University of California
Santa Barbara

Electronic instability in the kagome materials

A dissertation submitted in partial satisfaction
of the requirements for the degree

Doctor of Philosophy
in
Material Science

by

Farnaz Kaboudvand

Committee in charge:

Professor Ram Seshadri, Co-Chair
Professor Stephen D. Wilson, Co-Chair
Professor John W. Harter
Professor Vojtech Vlcek

September 2024

The Dissertation of Farnaz Kaboudvand is approved.

Professor Vojtech Vlcek

Professor John W. Harter

Professor Stephen D. Wilson, Co-Chair

Professor Ram Seshadri, Co-Chair

November 2023

Electronic instability in the kagome materials

by

Farnaz Kaboudvand

This thesis is dedicated to my amazing family and in loving memory of my dear Mom. Your constant love and support have been my anchor through it all. Mom and Dad, this is a small token of my deep gratitude for all that you've done for me.

Acknowledgements

I am sincerely grateful to everyone who has been a part of my incredible journey, providing constant support and encouragement. While it's difficult to express gratitude to every teacher, mentor, colleague, friend, and family member involved in this work, I would like to acknowledge the invaluable contributions of a select few who have made this dissertation possible.

First, my heartfelt appreciation goes to my incredible advisors, Ram Seshadri and Stephen Wilson, for their invaluable guidance, wisdom, and patience throughout the research process. Your support means a lot to me. They have been incredibly helpful in teaching me how to review and present my work, facilitating collaborations, and supporting my presentations at conferences.

I also extend my thanks to other significant scientific mentors involved in the research presented in this dissertation. Firstly, my committee members, John Harter and Vojtech Vlcek. I would also like to thank Michelle Johannes for generously sharing her time and mentorship.

A special thanks to Sam Teicher, whose feedback and guidance helped me find my path in quantum materials study. Additionally, I express my gratitude to Sanjeev Kolli, my first true mentor in the world of the DFT calculations. Also to my group-mates from Ram and Stephen's group for their support. I also express my gratitude to my collaborators and co-authors for their contributions to my research.

I would like to express my gratitude to all the staff at the Quantum Foundry and Materials Department for their support. I am especially grateful to Jocelyn Guzman, Kelsey Leonard Moore, Julie Standish, Fuzzy Rogers, Tal Margalith, Budd Jamieson, AJ Johnson, Sylvia Vogel, Dorothy Pak, and Amanda Strom for their kindness and consideration.

I express my sincere appreciation and love to my parents and Farzad, whose unwavering love, encouragement, and support have been the cornerstone of my academic pursuit. Mom, your absence is deeply felt every day, and your love continues to be my guiding force. I miss

you every day.

To my better half, your belief in my abilities and constant encouragement have been my guiding light through the challenges of this journey. Having you in my life and by my-side is truly wonderful, Farnoodam.

To my treasured old friends across borders, you have kept my spirits up despite the distances between us. To my friends in the US, who are like family to me here, thank you for always being there. To all my friends who have provided endless moral support, laughter, and companionship during the highs and lows of this academic adventure, your friendship has made this journey not just bearable, but truly joyful.

Curriculum Vitæ

Farnaz Kaboudvand

Education

2021-2023	Ph.D. in Materials Science at UC Santa Barbara, CA,
2019-2020	M.A. in Materials Science at UC Santa Barbara, CA, Santa Barbara.
	B.Sc. in Materials Science, IKIU, Iran.

Publications

1. B.R. Ortiz, G. Pokharel, M. Gundayao, H. Li, **F. Kaboudvand**, L. Kautzsch, S. Sarker et al. "YbV_3Sb_4 and EuV_3Sb_4, Vanadium-Based Kagome Metals with Yb^{2+} and Eu^{2+} Zig-Zag Chains", *Phys. Rev. Mater.* **7** (2023) 064201.
2. Y. M. Oey, **F. Kaboudvand**, B. R. Ortiz, R. Seshadri, and S. D. Wilson, "Tuning Charge-Density Wave Order and Superconductivity in the Kagome Metals $KV_3Sb_{5-x}Sn_x$ and $RbV_3Sb_{5-x}Sn_x$", *Phys. Rev. Mater.* **6** (2022) 074802.
3. **F. Kaboudvand**, S. M. Teicher, S. D. Wilson, R. Seshadri, and M. D. Johannes, "Fermi Surface Nesting and the Lindhard Response Function in the Kagome Superconductor CsV_3Sb_5", *Appl. Phys. Lett.* **120** (2022) 111901.
4. Y.M. Oey, B.R. Ortiz, **F. Kaboudvand**, S.D. Wilson, and R. Seshadri, "Fermi Level Tuning and Double-Dome Superconductivity in the Kagome Metals $CsV_3Sb_{5-x}Sn_x$", *Phys. Rev. Mater.* **6** (2022) L041801.
5. C. Hansen, J. Zak, A. Martinolich, J. Ko, N. Bashian, **F. Kaboudvand**, A. Van der Ven, B. Melot, W.J. Nelson and K. See, Multielectron, "Cation and Anion Redox in Lithium-Rich Iron Sulfide Cathodes", *J. Am. Chem. Soc.* **142** (2020) 6737–6749.
6. **F. Kaboudvand**, J. Vinckeviciute, S. Kolli, M.D. Radin, and A. Van der Ven. "Phase Stability and Electronic Structure of Tin Sulfide Compounds for Li-ion Batteries", *Phys. Chem. C* **123** (2019) 29086–29095.

Abstract

Electronic instability in the kagome materials

by

Farnaz Kaboudvand

The discovery of AV_3Sb_5 (A = K, Rb, Cs) compounds with a kagome net structure has unveiled their intriguing properties including superconductivity and unique topological characteristics in their electronic structure. These materials also exhibit charge density wave (CDW) ordering, which manifests as a distortion known as a breathing mode in the kagome layers. It has been proposed that this CDW ordering arises from nesting effects between saddle points on the Fermi surface.

To contribute to the evolving understanding of this fascinating class of materials, this thesis presents a comprehensive exploration of diverse kagome materials. The focus lies on conducting calculations that delve into the Fermi surface nesting and Lindhard susceptibility of CsV_3Sb_5, a prominent member of the AV_3Sb_5 family. Furthermore, the thesis thoroughly investigates the coupling between CDW and superconducting (SC) states through experimental and computational approaches, particularly by introducing hole doping into the systems. The resulting phase diagrams for AV_3Sb_5 unveil the profound impact of slight carrier doping on the SC and CDW orders in these materials. In addition, this thesis presents a comprehensive study of other kagome-based materials, such as the members of the AM_3X_4 family, including a focused analysis of YbV_3Sb_4 and EuV_3Sb_4. The research also delves into the properties of the RV_6Sn_6 compounds, characterized by a vanadium kagome-based structure, and investigates the intriguing characteristics of the RM_3Pn_3 family featuring a triangular lattice, which shares similar signatures of instabilities.

Throughout the thesis, a spotlight is cast on various aspects, including Fermi surface

nesting-driven instabilities, CDW phenomena, and magnetic behaviors within these materials. Meticulous experimental investigations and advanced theoretical analyses offer valuable insights into the complex interplay between electronic structures, CDW ordering, and superconductivity. The findings challenge previous assumptions and classifications, emphasizing the critical role of electron-phonon interactions and complex electronic correlations in shaping the observed behaviors of these materials. Overall, this dissertation contributes to a deeper understanding of the kagome materials and underscores the potential of these materials for realizing exotic electronic states and offers new avenues for exploring their unique physical phenomena.

Contents

Chapter 1

Introduction

The central focus of this dissertation is to equip researchers with indispensable tools and chemical insights necessary for the prediction and synthesis of quantum materials using sophisticated ab-initio calculations. Despite the notable advancements in first-principles methods over the past decades, which have considerably popularized density functional theory calculations in the realm of materials exploration, the practical implementation of these computational developments in experimental contexts has been somewhat limited. While recent investigations have made significant strides in unraveling the properties of quantum materials through systematic analyses, the first principle study could help to better understand the physics behind the instabilities in these materials. Some relatively recent studies[1, 2], have contributed significantly to the comprehensive understanding of quantum materials without always incorporating crucial chemical insights. It is crucial to recognize that simplified bonding models, widely acknowledged by solid-state chemists and physicists, continue to provide invaluable insights in experimental research.

This dissertation serves as a bridge between the intricate mathematical concepts governing quantum properties and their practical implications for experimental investigations. By studying and perturbing the electronic structures of different kagome materials, this work aims to help

find and improve quantum materials with specific properties. Through this contribution, the field of materials science can be advanced, leading to the discovery of novel materials with unique applications. With this objective in mind, the dissertation presents a series of careful computational studies focusing on a comprehensive exploration of the intriguing properties and diverse behaviors exhibited by kagome-based materials, including the notable AV_3Sb_5 (A = K, Rb, Cs) compounds, celebrated for their unique topological characteristics and superconductivity. The captivating discovery of a breathing mode attributed to charge density wave (CDW) ordering has sparked interest in understanding the underlying Fermi surface nesting effects that drive these phenomena [3, 4, 5, 6].

To investigate the origins of charge density waves and the Fermi surface in CsV_3Sb_5, we conducted Lindhard response calculations, detailed in Chapter 2. Expanding our examination of the Fermi surface, we tuned the band structure of CsV_3Sb_5 via Sn doping, as outlined in Chapter 3. Additionally, to provide a comprehensive understanding and comparison of the properties within the broader AV_3Sb_5 family, we explored the tuning of charge density wave ordering and superconductivity with Sn doping, which is discussed in Chapter 4.

Beyond the AV_3Sb_5 family, the dissertation delves into the investigation of other families exhibiting the kagome structure. In Chapter 5, we present a detailed analysis of YbV_3Sb_4 and EuV_3Sb_4, two newly discovered vanadium-based kagome metals. Additionally, Chapter 6 explores the properties of ScV_6Sn_6 from the AB_6X_6 family, which has garnered significant attention due to its electronic instabilities. Furthermore, we provide an insightful comparison of $CsTi_3Bi_5$ and CsV_3Sb_5.

In Chapter 7, we present our findings on $LaCd_3P_3$, a member of the RM_3Pn_3 family, also known as the 133 family. Due to its unique two-dimensional triangular lattices, $LaCd_3P_3$ represents a promising candidate for the study of electronic instabilities. We hope that these comprehensive studies shed light on the intricate physics behind the instabilities observed in these materials, paving the way for a deeper understanding of their underlying mechanisms.

1.1 Motivation

The prospect of achieving room temperature superconductivity stands as one of the most compelling and sought-after goals in the realm of scientific research. The concept of materials that can conduct electricity with zero resistance at temperatures easily attainable and sustainable in everyday environments is nothing short of a dream for scientists and engineers alike. Room temperature superconductors would fundamentally transform power transmission grids, allowing for nearly lossless electricity transfer over vast distances, thus reducing energy wastage and enhancing overall energy efficiency. This breakthrough could significantly alleviate global energy demands and bolster the transition to more sustainable energy sources. Moreover, the development of superconducting electronics operating at room temperature would open the door to an entirely new generation of ultra-fast and energy-efficient computing devices, revolutionizing information technology and data processing capabilities. The pathways to achieving room-temperature superconductivity remain unclear, underscoring the significance of exploring the fundamental physics of superconductors. A particular focus on electronic behavior, accessible through comprehensive ab-initio methods like Density Functional Theory (DFT), holds key insights into unraveling this phenomenon.

Following that, the discovery of kagome metals AV_3Sb_5 (A = K, Rb, Cs)[3] has sparked significant interest. These materials serving as a new family of superconductors that additionally exhibit unique electronic structure topology. While their practical application in devices is currently limited by the requirement for extremely low temperatures for superconductivity to occur, the exploration of these kagome metals holds promise for uncovering new physics phenomena. Initial calculations and collaborative experimental efforts have suggested that these materials could provide insights into the mechanisms governing superconductivity and its interplay with proposed topological surface states. As presented in Figure 1.1(a), we have magnetization frustration in equilateral triangles. If we corner share the triangles, we will ended

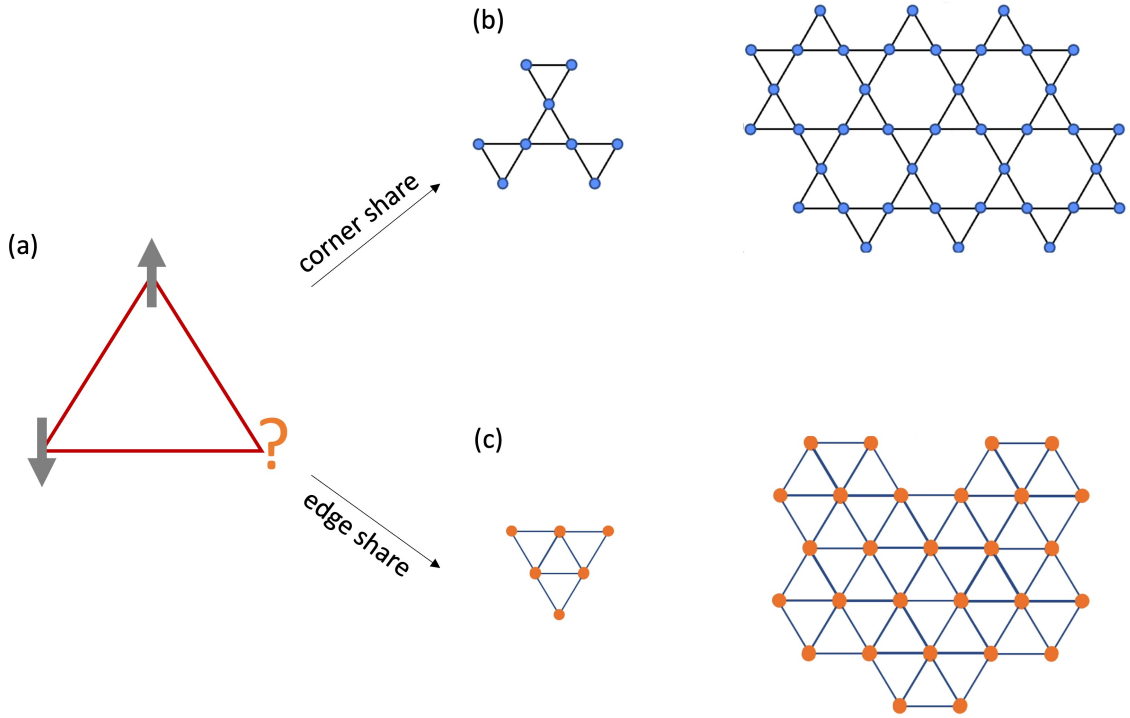

Figure 1.1: (a) Frustration in equilateral triangles lattice. (b) Corner share triangles leads to kagome network, and (c) edge sharing triangles will make a triangular structure.

up with kagome network.(Figure 1.1) The specific arrangement of this lattice means that the electronic structure naturally features a flat band, inflection points corresponding to singularities in the density of states called van Hove singularities and Dirac cones[7, 8, 9, 10, 11]. The flat band [1] arises due to the cancellation of quantum interference from localized states. Alongside the presence of van Hove singularities [2], this facilitates the system to persist within the realm of strong interactions. Simultaneously, the existence of Dirac cones [3] fosters non-trivial topological properties. While kagome insulators have traditionally been sought as potential hosts of quantum spin liquid states and laboratories for highly frustrated magnetism[12, 13, 14, 15], kagome metals have also captured significant attention due to their unique electronic structures. Depending on the electron filling in their lattices, these materials can exhibit a range of instabilities, including superconductivity, spin liquid states, and charge density waves[16, 17]. Consequently, the kagome network serves as an excellent framework for investigating the intricate interplay between frustrated geometry, correlations, and topology.

To deepen our understanding of kagome systems and elucidate their electronic structures, this study employs first principles techniques. During my Ph.D., I focused on applying first-principles techniques specifically under the framework of density functional theory (DFT) calculations, to investigate the Fermi surface and the underlying origins of charge density waves in kagome systems. Additionally, we examine the evolution of the Fermi level and band structure as electrons or holes are introduced through elemental substitution in each system. By correlating our DFT-simulated data with experimental observations, we aim to elucidate the physical mechanisms responsible for the observed effects in kagome materials. By contributing

[1] Flat band refers to a band structure in which the energy dispersion relation is relatively flat. This typically indicates that the energy of the electronic states is nearly independent of the momentum. Such flat bands can lead to the emergence of exotic electronic and magnetic properties in materials.

[2] which are points of maximum or minimum in the density of states of a material. These singularities can significantly influence the electronic and optical properties of materials, leading to various interesting phenomena, such as the enhancement of certain physical properties at these specific energy levels.

[3] Dirac cone refers to the shape of the energy dispersion relation near the Fermi level in certain materials. It resembles a cone-like structure, indicating linear dispersion of energy as a function of momentum. Dirac cones are a signature feature of materials with linear band crossings, often associated with the presence of massless fermions.

to the expanding knowledge base on electronic instability in kagome materials, this report strives to shed light on their fascinating properties and their potential applications in emerging quantum technologies.

1.2 Kagome materials

Kagome metals represent a captivating frontier in the pursuit of stabilizing unique correlated and topological electronic states. The electron filling within the kagome network plays a crucial role in determining the diverse range of instabilities observed in these materials. These instabilities encompass phenomena such as spin liquid states [18], charge density waves (CDW) [17] , and superconductivity (SC) [9, 19]. Moreover, the kagome structural motif offers the possibility of hosting topologically nontrivial electronic structures, wherein the coexistence of Dirac cones and flat bands can give rise to strong correlation effects, potentially leading to the emergence of correlated topological states. Recently, a novel family of non-magnetic kagome metals has been discovered, characterized by the AV_3Sb_5 (A = K, Rb, Cs) structure with a *P6/mmm* space group [3, 4, 5, 6, 20] which we called them as short "135 family". These compounds consist of V cations coordinated by octahedral Sb, forming a kagome network, while layers of A-site ions separate the kagome planes, resulting in a two-dimensional metallic appearance. Notably, CsV_3Sb_5, a member of the AV_3Sb_5 family, exhibits superconductivity with a critical temperature (T_c) of 2.5 K. As presented in Figure 2.1, the crystal structure and temperature-dependent resistivity of CsV_3Sb_5 have been investigated, revealing a phase transition at T_{CDW} = 94 K, accompanied by anomalies in magnetic susceptibility, electrical resistivity, and heat capacity [4]. Previous studies have attributed this phase transition to charge density waves and a Peierls-like nesting-driven instability [20].

The search for electronic instabilities in two-dimensional kagome networks has led to significant interest in the formation of a superconducting ground state. However, layered

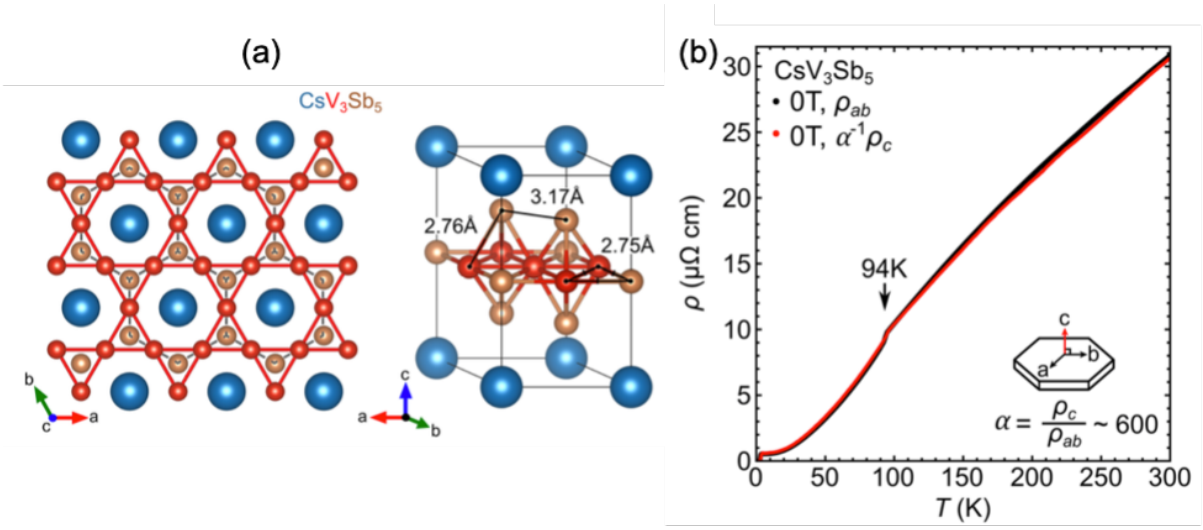

Figure 1.2: Kagome structure of CsV_3Sb_5 (used with permission from the authors)[4]. (a) Crystal structure of layered CsV_3Sb_5, (b) Resistivity as a function of temperature with the CDW transition temperature indicated. The out-of-plane resistivity is nearly 600 times larger than in a plane, emphasizing the two-dimensional nature of the Fermi surface.

kagome metals that exhibit superconductivity are rare. The intriguing interplay between the nontrivial topology accessible through their electronic band structures and the emergence of an intrinsic superconducting state makes the study of kagome materials particularly enticing for realizing exotic ground states and quasiparticles. Theoretical predictions suggest that unconventional superconductivity can arise in heavily doped kagome networks through nesting-driven interactions [8]. This mechanism, initially proposed for doped graphene due to its hexagonal symmetry akin to the kagome network, relies on scattering between saddle points of a band located at the *M* points of the two-dimensional Brillouin zone. In the chapter 2 with applying the Lindhard and DFT calculations we will explore the origin of the CDW and it's relation to *M* points in these compounds[21].

1.3 Charge density wave

In a metal, the electron density is highly uniform, and the equilibrium positions of the ions usually form a perfectly periodic lattice. At low temperatures though, the electronic structures of metals become unstable, and in some metals, the Fermi surface instability leads to the redistribution of the charge density, forming a periodic spatial modulation. The modulation of the electron density is called a charge density wave (CDW) and the transition temperature is known as T_{CDW} [22, 23]. The existence of charge density waves was first predicted in 1930 by Rudolf Peierls [24]. In summary, Peierls' theory predicts that a Fermi surface of a one-dimensional (1D) metal chain is unstable against any external perturbations at very low temperature, and the formation of a static lattice distortion is one of the possible scenarios. In fact, he showed that an electronic disturbance with the wave vector $q = 2k_F$ can change the atomic periodicity of the chain to 2a, where k_F and a are the Fermi wave number and the lattice constant respectively, and open a gap at the zone boundary ($k = \pi/2a$) of the new unit cell containing two atoms.

An illustration of the Peierls picture is presented in Figure 1.3. An atomic model of such a 1D chain with one electron per atomic site above T_{CDW}, and the corresponding free electron band structure illustrated in Figure 1.3(a). As it can be seen in Figure 1.3(b), two neighbor ions have moved toward each other, forming dimers of ions below T_{CDW}. The corresponding electronic band structure in the new zone is shown. We can clearly see that the transition spontaneously breaks the translational symmetry of the crystal and modifies the electronic structure. Therefore, in the Peierls model there is usually a metal-to-insulator transition at T_{CDW}, which is known as Peierls transition[22, 23, 24].

For years, the Peierls picture was the most common method to interpret CDWs in metals connecting the presence of CDWs in metals to the observation of the Fermi surface nesting (FSN). A very important contribution of Mazin and Johannes[25] casts doubt on whether, in

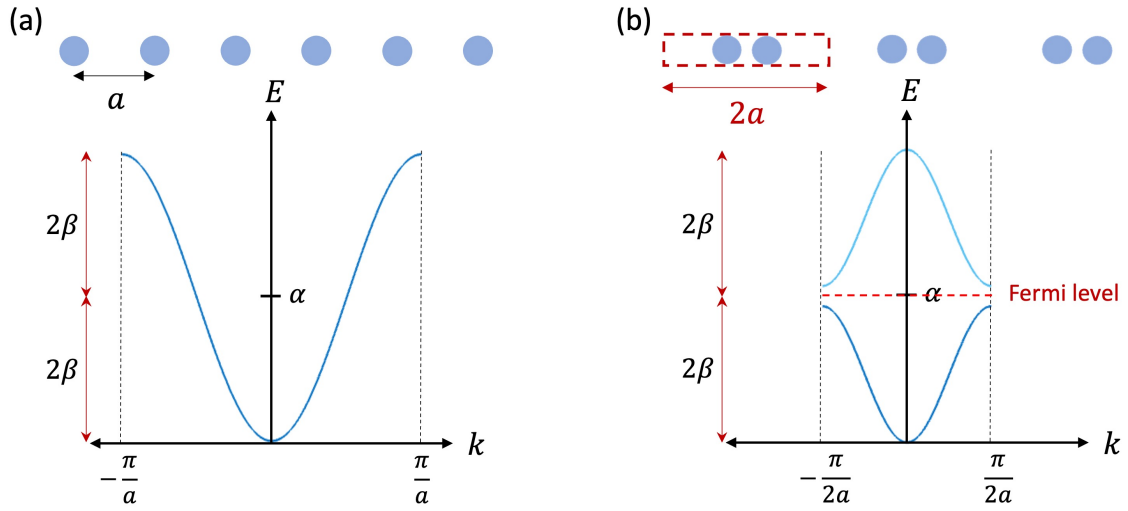

Figure 1.3: Demonstration of the Peierls picture. (a) Atomic model of a 1D chain with lattice constant a, and the free electron band of the 1D chain above T_c. (b) Atomic model of the 1D chain below T_c, with the lattice constant changed to $2a$. The free electron band of the 1D chain below T_c with a gap opening at k_F is also presented.

anything other than one-dimension, FSN could be responsible for the formation of CDWs.

Although the Peierls description of nesting-driven distortions often succeeds in 1D materials [22, 23, 26], for higher-dimensional materials with 2D or 3D connectivity, this model must be extended. One way to understand whether the electron response can drive a Peierls phase transition is to calculate the susceptibility, $\chi(q,\omega)$, for a given electronic configuration and to use the zero-energy value of the Lindhard response function, $\chi_0(q,\omega=0)$ [22, 23, 25, 26]. In the constant matrix element approximation, the real part, $\chi^{'}(q)$, and the imaginary part, $\chi^{''}(q)$, can be written as:

$$\chi^{'}(q) = \sum_k (f(\varepsilon_k) - f(\varepsilon_{k+q}))/(\varepsilon_k - \varepsilon_{k+q}) \tag{1.1}$$

$$\lim_{\omega\to 0} \frac{\chi^{''}(q,\omega)}{\omega} = \sum_k \delta(\varepsilon_k - \varepsilon_F)\delta(\varepsilon_{k+q} - \varepsilon_F) \tag{1.2}$$

where ε is the electron's energy and f denotes the electron's Fermi distribution function. The imaginary part, $\chi^{''}(q,\omega \to 0)$, has been used in first-principles studies as a comparative test of FSN. As mentioned above, there was a common misconception that FSN is almost always responsible for a CDW. The idea was that if Fermi surface contours match when shifted along the observed CDW wave vector, then the CDW is nesting derived. However, by investigating prototypical CDW materials like $NbSe_2$, $TaSe_2$, and $CeTe_3$, Johannes and Mazin argued that only a tiny fraction, if any, of the observed charge ordering phase transitions are true analogs of the Peierls instability and FSN derived [25, 27]. Based on the literatures, there are several requirements that a system should satisfy to be considered a Peierls system:

- There must be substantial nesting of the Fermi Surface, which can be reflected by calculating the imaginary part, $\chi_0''(q)$.

- The nesting-derived peak must carry over into the real part of the susceptibility, $\chi_0'(q)$, at the same wavevector.

- The peak in $\chi_0'(q)$ must translate into a divergence in the full electronic susceptibility to cause the electronic subsystem to be unstable.

- All phonons must soften at the CDW's wavevector.

Johannes et al. cleared the divergence in the imaginary part of susceptibility, reflecting the Fermi surface topology, and the real part, induced electronic CDW instability [25, 27].

Johannes et al. used density functional calculation and Lindhard function in a case study of $NbSe_2$ as a classic CDW materials to provide a clear example of the lack of influence of FSN on CDWs. $NbSe_2$ is a quasi-2D material with hexagonal layered structure that undergoes a CDW transition at $T_{CDW} = 33.5$ K, and superconducting transition at $T_c = 7.2$ K [26, 27, 28, 29, 30]. Figure 1.4 displays the crystal structure of $NbSe_2$ visualized with Vesta [31] and its measured resistivity versus temperature. The first calculated electronic structure for NbSe2 by Mattheiss [29] were generated using a non-self-consistent potential which is in reasonable agreement with later self-consistent calculations[28]. This earlier work led to suggestions that the charge

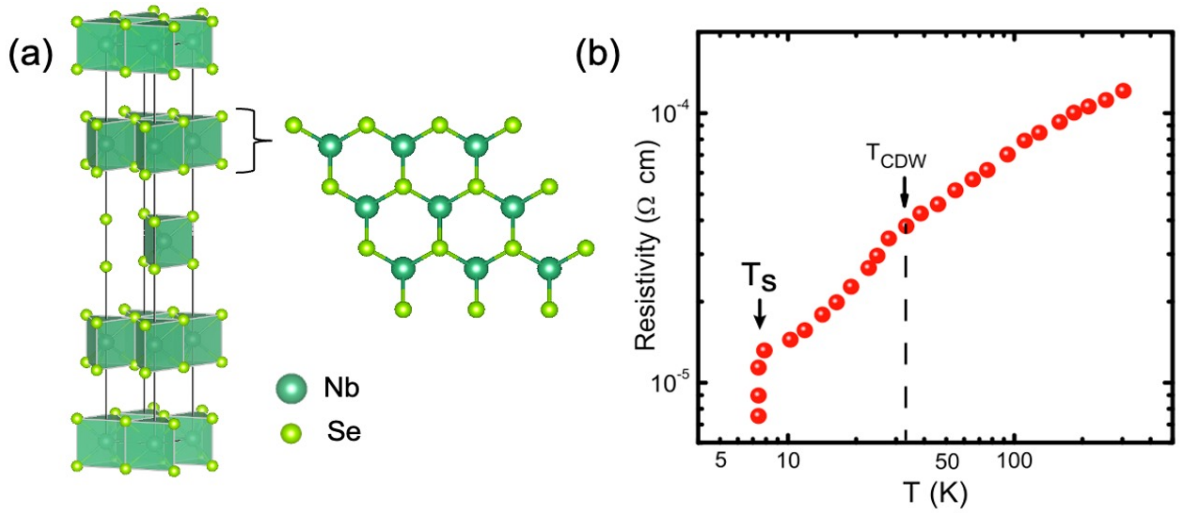

Figure 1.4: The structure of $NbSe_2$. (a) Unit cell of layered $NbSe_2$ (left) and top view of single layer (right). (b) Resistivity as function of temperature. Superconducting and CDW transition temperatures marked[26].

density wave (CDW) transition in this material was driven by FSN[29]. However, Johannes et al.[27] later provided a quantitative analysis of the non-interacting susceptibility, $\chi''(q, \omega = 0)$, revealing that the momentum space structure is considerably weak, and that FSN does not play a significant role in driving CDW transitions. Comparison between the crystal structures of CsV_3Sb_5 and $NbSe_2$, see Figure 1.2 and Figure 1.4, reveals notable similarities, reflecting analogous features in their resistivity versus temperature plots. Motivated by these similarities, we conducted Lindhard calculations on the CsV_3Sb_5, the results of which are discussed in detail in Chapter 2.

1.4 Computational techniques

Certainly, the past 70 years have witnessed remarkable progress in our understanding of the electronic structures of materials, largely owing to the development of computationally efficient and increasingly accurate simulation techniques. Density functional theory (DFT) has

been a cornerstone of this progress, providing a powerful framework for studying the electronic properties of atoms, molecules, and solids. This approach allows researchers to calculate the electronic structure of a system by solving the many-body Schrödinger equation, which describes the behavior of quantum particles. The evolution of quantum mechanical theory has been instrumental in revolutionizing our understanding of the fundamental nature of matter, leading to breakthroughs in fields such as condensed matter physics, chemistry, and materials science. Through the application of DFT, researchers can now explore the behavior of electrons within materials, gaining insights into their energies, wave functions, and interactions, thereby unraveling the intricate properties and behaviors of a wide range of substances, from simple atomic systems to complex solid-state materials. Equation 1.3 shows the Schrodinger equation.

$$\hat{H}\psi(r) = E\psi(r) \tag{1.3}$$

provided here in the time-independent form where $\hat{H}$ is the Hamiltonian, E is the system energy, and ψ is the wavefunction, which can depend on position, r. While ψ itself is not a physical observable, Max Born demonstrated in his work on quantum mechanics that the modulus squared of this quantity, $|\psi|^2$, can be interpreted as a probability density [32]. For example, the modulus square of a single electron wavefunction represents the probability of finding the electron in a given state within the system. Born's interpretation of the wavefunction laid the groundwork for the probabilistic interpretation of quantum mechanics, fundamentally shaping our understanding of the behavior of subatomic particles and their interactions within physical systems.

While the equation 1.3 serves as the foundation of quantum mechanics, it does not readily offer guidance on the practical means of solving for the wavefunction within an actual material. Extending the discussion to a system of electrons within a material, the Schrödinger equation can be further expressed as:

$$\left[-\frac{\hbar^2}{2m}\nabla^2 + V_{\text{ext}}(\mathbf{r}) + V_{\text{int}}(\mathbf{r})\right]\psi(\mathbf{r}) = E\,\psi(\mathbf{r}) \tag{1.4}$$

where $\hbar$ is the reduced Planck constant, m represents the effective mass of the electron, ∇^2 denotes the Laplacian operator, $V_{\text{ext}}(\mathbf{r})$ signifies the energy associated with the interaction of electrons with an external potential, $V_{\text{int}}(\mathbf{r})$ represents the energy associated with the interaction between electrons, and $\psi(\mathbf{r})$ is the wavefunction depending on the position vector $\mathbf{r}$. The term E represents the energy of the system. This equation is fundamental in describing the behavior of electrons in various materials, considering the influence of both external potentials and interactions between electrons.

In the majority of materials, the movement of atoms occurs at a significantly slower rate compared to the speed of the electrons that envelop them, establishing bonds in between. Hence, quantum mechanical simulations of materials generally adopt the Born-Oppenheimer assumption [33], which asserts that atomic nuclei remain static with fixed positions. These simulations primarily concentrate on modeling the behavior of electrons and their reactions to the atomic potentials. Equation 1.4 incorporates the Born-Oppenheimer approximation by integrating the ionic potentials associated with atomic nuclei, as part of the total potentials, while the explicit treatment of the nuclear wavefunctions is omitted. However, it is important to note that due to computational constraints, it is challenging to fully account for electron interactions in these simulations. Even the modeling of individual atoms with three or more electrons continues to be an active area of research due to the intricacy involved in directly computing many-body interactions.

Hohenberg and Kohn established two significant theorems that served as the foundation for contemporary density functional theory (DFT) approaches to solving the Schrödinger equation [34, 35, 36]. Hohenberg and Kohn proved fundamental properties of the functional $E[n(r)]$, which takes an electron density $n(r)$ as input to compute the corresponding energy E. The H-K

theorems can be summarized as follows:

1. For any system of interacting particles in an external potential $V_{\text{ext}}(r)$, the potential is uniquely determined by the ground state electron density, $n_0(r)$.

2. There exists a universal functional for the energy, $E[n(r)]$, that is valid for any choice of external potential. For any given $V_{\text{ext}}(r)$, the global minimum of this functional is the ground state energy, and the electron density that minimizes this functional, $n_0(r)$, represents the ground state electron density.

As per the first theorem, it is known that the Hamiltonian of a system is uniquely determined by $n_0(r)$. Consequently, all properties of a material, including ground and excited states, are determined based on the ground state electron density. The second theorem indicates that understanding the functional $E[n]$ and external potential $V_{\text{ext}}(r)$ is sufficient to determine the ground state of a system, though not its excited states. In the context of materials simulation, the external potential is primarily contributed by the periodic potential originating from the atomic lattice of nuclei. Selecting the appropriate functional allows precise determination of the ground state properties, given a material with a known crystalline structure and associated periodic potential. Nevertheless, despite the H-K theorems suggesting the existence of an exact energy functional, the true functional remains unknown.

While Hohenberg and Kohn provided a theoretical framework for density functional methods, the H-K theorems themselves do not provide immediate insight into how one can simplify the many-body problem of inter-electron interactions into a computationally tractable form. Kohn and Sham introduced the ansatz that a material can be modeled with completely independent electrons and that the effect of electron interaction and correlation can be accounted for by an exchange-correlation functional, $E_{\text{xc}}[n(r)]$ [35]. The Kohn-Sham equation for the ground state energy functional can be written as:

$$E_{\mathrm{KS}} = T_s[n] + \int dr V_{\mathrm{ext}}(r) n(r) + E_H[n] + E_{\mathrm{II}} + E_{\mathrm{xc}}[n] \tag{1.5}$$

where $T_s[n]$ is the kinetic energy, $V_{\mathrm{ext}}(r)$ represents the external potential, experienced by the electrons due to the atomic nuclei as well as any applied fields, $n(r)$ is the electron density, $E_H[n]$ is the Hartree energy, associated with coulomb interactions between the electron and surrounding. E_{II} denotes the ion-ion interaction energy, and $E_{\mathrm{xc}}[n]$ is the exchange-correlation energy functional. Given the appropriate choice of the exchange-correlation functional, the determination of a system's ground state involves minimizing the Kohn-Sham energy. While the precise exchange-correlation functional remains elusive, the Kohn-Sham assumption is effective in practical scenarios due to the screening of electron correlations in many materials. In compounds with a substantial electron density, particularly metals, the electron system is well described by the assumption that each electron predominantly interacts with the collective potential of the remaining electrons rather than with each electron individually. Ongoing extensive research is dedicated to identifying increasingly accurate options for $E_{\mathrm{xc}}[n]$.

Another significant simplifying assumption in many contemporary DFT codes is the localization of core electrons, which are considered to have minimal impact on chemical bonding and are, therefore, treated as part of the external potential, $V_{\mathrm{ext}}(r)$. Consequently, simulations typically focus solely on the wavefunctions of valence electrons, while the influences of core electrons are approximated using pseudopotentials [37] or PAW potentials [38] localized at the atomic sites.

Given the previous discussion, we can outline both technical and fundamental challenges associated with the Kohn-Sham DFT calculations employed in this dissertation. Two practical issues are limitations on the system size and accuracy of approximate choices of $E_{\mathrm{xc}}[n]$. Despite remarkable progress in computing hardware and algorithmic efficiency, systems with hundreds or thousands of atoms are not currently computationally tractable for most DFT users. DFT is

generally most accurate in describing crystalline solids, which are well approximated by a small (periodic) unit cell with a small number of atoms.

Our incomplete knowledge of $E_{\mathrm{xc}}[n]$ can make it challenging to accurately simulate materials with strong electron correlations based on Kohn-Sham DFT. Standard functional such as the local density approximation (LDA) [39,40] and generalized gradient approximation (GGA) [41] methods employed here often fail spectacularly when simulating strongly-correlated systems. This is a particular challenge for work on topological superconductors since the superconducting phase itself, which involves strong interactions such as Cooper-pairing of electrons, cannot be simulated with standard DFT methods. In practice, however, DFT can provide useful information about the electronic properties in the metallic phase of a material that has a low-temperature superconducting transition. Extensive DFT calculations are employed in this dissertation to understand the metallic phases of superconducting metals.

A fundamental issue is the treatment of thermal properties and excited states. Even with knowledge of the exact functional, $E_{\mathrm{xc}}[n]$, the H-K theorems only guarantee an exact solution for the ground state properties of a material at 0 K. While progress has been made in modeling thermal transport via phonon calculations and adjusting for temperature effects via thermodynamic sampling ans Monte Carlo simulations, simulating excited states is a very present challenge.

Both fundamental and technical issues contribute to inaccuracy in the prediction of electronic band gaps using standard DFT methods, which is a particular challenge for the field of topological materials since an accurate prediction of band inversion is necessary to correctly classify the topology in a material. The experimentally measured band gap of a material is the energy required to excite an electron from an initial state in the highest occupied state of the valence band to the lowest unoccupied state in the conduction band. Consequently, the DFT band gap is typically calculated by determining the separation between the highest energy eigenvalue in the valence band and the lowest energy eigenvalue of the conduction band based on the calculated (Kohn-Sham approximated) ground state configuration. However, it is known

that even an exact Kohn-Sham density functional theory solution will not provide an exact band gap using this method. Furthermore, in addition to the fundamental limitations associated with the treatment of excited states in general, the Kohn-Sham DFT band gap is susceptible to errors arising from derivative discontinuity, complicating the accurate determination of the band gap for materials, especially those crucial for the investigation of topological phenomena. This subject with more details has been discussed in Dr. Samuel Teicher's thesis[42].

The objective of this dissertation is to develop tools and chemical intuition for the prediction and synthesis of kagome materials using ab-initio calculations to understanding their electronically structures. While significant progress has been made in first-principles methods over the past few decades, making density functional theory (DFT) calculations widely accessible and commonplace in materials discovery, these advancements have not always translated into laboratory-relevant knowledge. Recent influential studies have made notable contributions to the field of topological materials by systematically calculating and categorizing topological invariants for large databases of materials, relying on mathematical rigor without incorporating chemical insights [2, 43, 44, 45]. However, understanding the electronic structure can have an immediate impact on experimentalists.

This dissertation aims to fill this gap by integrating ab-initio calculations with chemical intuition to develop a comprehensive framework for predicting and synthesizing kagome materials. In this research, we will explore advanced techniques to understand the electronic structure and the connections between the material property that we observe experimentally, and their electron density (like dipole moment and charge density) and electronic energy (potential energy surface, bond energies). By systematically analyzing different systems, we aim to categorize them based on their distinct electronic and structural features. Furthermore, we will investigate the effects of various parameters, such as doping electron or hole into the structure, on the emergence and manipulation of topological properties.

Chapter 2

Fermi surface nesting and the Lindhard response function of CsV_3Sb_5

[1] The discovery of AV_3Sb_5 (A = K, Rb, Cs) compounds with a kagome net structure has unveiled their intriguing properties, including superconductivity and unique topological characteristics in their electronic structure. These materials also exhibit charge density wave (CDW) ordering, which manifests as a distortion known as a breathing mode in the kagome layers. It has been proposed that this CDW ordering arises from nesting effects between saddle points on the Fermi surface. To contribute to the evolving understanding of this fascinating class of materials, this study presents calculations focusing on the Fermi surface nesting and Lindhard susceptibility of CsV_3Sb_5. Understanding the nesting effects on the Fermi surface and their relationship to the breathing mode distortions is crucial for unraveling the underlying mechanisms driving the CDW ordering in AV_3Sb_5 compounds. By examining the Fermi surface nesting (FSN) and its correlation with the observed breathing mode distortions, insights can be gained into the nature of the CDW transition and its connection to the electronic structure.

[1]The contents of this chapter previously appeared in Ref. [21]: **F. Kaboudvand**, S. M. Teicher, S. D. Wilson, R. Seshadri, and M. D. Johannes, "Fermi Surface Nesting and the Lindhard Response Function in the Kagome Superconductor CsV_3Sb_5", *Appl. Phys. Lett.* **120** (2022) 111901. Reprinted with permission.

2.1 Introduction

Compounds with kagome nets have attracted recent attention due to the interesting ground states they can display. As a consequence of their geometry and depending on the degree of electron filling, kagome materials are predicted to host a variety of instabilities associated with spin liquid states, superconductivity, charge density waves (CDW), and more. [17, 19] The recently discovered non-magnetic kagome metals AV_3Sb_5 (A = K, Rb, Cs) exhibit charge density wave and superconducting order and are predicted to host $\mathbb{Z}_2$ topological surface states [3, 4, 5].

The unique transitions and functionalities observed in kagome metals have been attributed to distinct features in their electronic band structures, particularly the saddle point located at the M point, which plays a crucial role in topological band inversion. Phenomenological models have long predicted the existence of two-dimensional charge density waves (CDW) in kagome metals with 3-fold rotational symmetry, also referred to as $3Q$ phases, arising from perfect Fermi surface nesting (FSN) between the M points [9, 46, 47]. Experimental investigations have confirmed the presence of this $3Q$ CDW order in all members of the AV_3Sb_5 family [48, 49, 50, 51, 52, 53, 54]. Simulations have further supported these findings, demonstrating the instability of the room temperature structure to 2D breathing mode distortions at $q = [1/2, 1/2, 0]$ and $q = [1/2, 1/2, 1/2]$, which are associated with phonon modes at the M and L points [6].

In addition to the observed $3Q$ charge density wave (CDW) order, additional CDW distortions have been identified in the AV_3Sb_5 compounds. Surface probes such as scanning tunneling microscopy have revealed a unidirectional $4a_0$ stripe ordering, while bulk X-ray diffraction experiments suggest either 2-fold or 4-fold distortions along the c-axis, indicating the possibility of either L-type ($q = [1/2, 1/2, 1/2]$) or U-type ($q = [1/2, 1/2, 1/4]$) total q-vectors for the bulk charge density wave [48, 50, 51]. The origin of these c-axis distortions could be attributed to various factors, such as the stacking of kagome planes or an in-out variation of the breathing

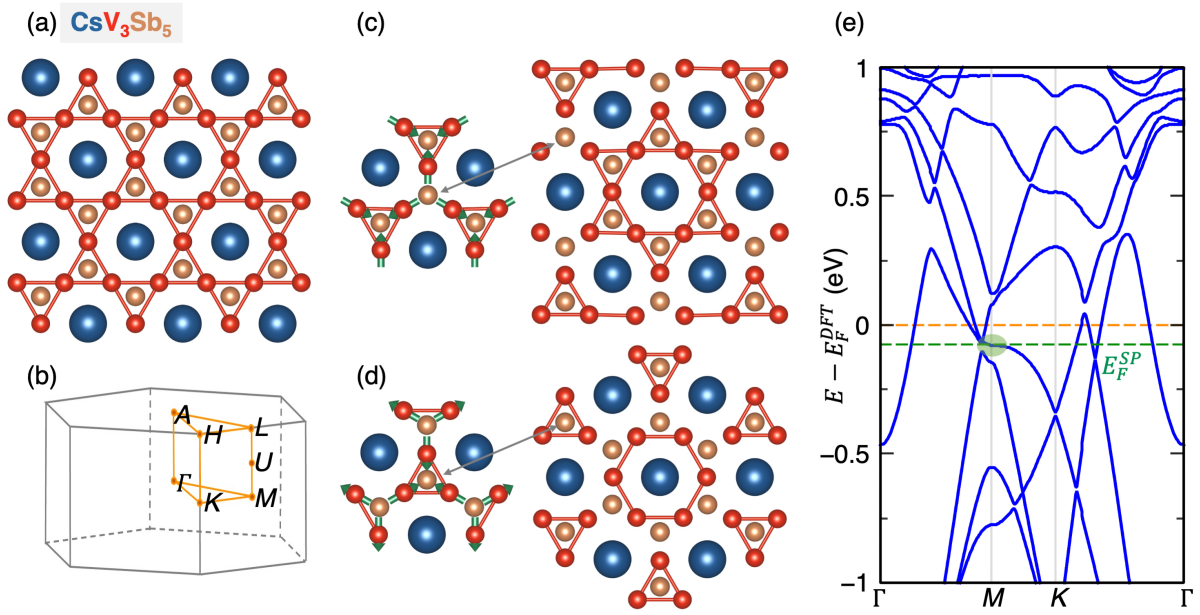

Figure 2.1: Crystal and electronic structure of CsV_3Sb_5. (a) Room temperature structure with un-distorted kagome nets. (b) reciprocal space Brillouin zone with high symmetry points labeled. (c) and (d) present two in-plane breathing mode candidates, the Star of David (SoD) and the inverse Star of David (ISD) distortions. These M-type distortions have $q = [1/2, 1/2, 0]$. (e) Presents the electronic band structure of CsV_3Sb_5, displaying the Fermi level from DFT calculations, and the previously-observed experimental Fermi level.

mode [20, 50]. While Fermi surface nesting has been proposed as a possible explanation for the in-plane $3Q$ ordering based on previous theoretical work, it remains uncertain whether these additional distortions can be attributed to nesting instabilities.

The crystal and electronic structures of CsV_3Sb_5 are illustrated in Figure 2.1. Figure 2.1(a) presents the room temperature structure of CsV_3Sb_5 with an undistorted kagome lattice. The reciprocal space Brillouin zone, highlighting the high symmetry points, is shown in Figure 2.1(b). The structure exhibits two potential in-plane breathing mode distortions, namely the Star of David (SoD) and inverse Star of David (ISD) (also known as Tri-Hexagonal) distortions, as depicted in Figures 2.1(c) and 2.1(d), respectively. Both SoD and ISD distortions correspond to M-type distortions with $q = [1/2, 1/2, 0]$. The electronic band structure of CsV_3Sb_5 is displayed in Figure 2.1(e), with the green region highlighting the M saddle point region. While multiple

saddle point features are expected in kagome metals and are present in the band structure of CsV_3Sb_5 [55], the CDW instability in this compound is commonly attributed to the large flat saddle-point band at E_F^{SP}. There is a slight discrepancy between calculations, but most *ab initio* simulations place the Fermi level slightly above the saddle point at E_F^{DFT}. However, experimental studies utilizing angle-resolved photoemission spectroscopy have suggested that the true Fermi level may reside slightly lower, near or just above the saddle point around E_F^{SP} [4, 53, 55].

The existence of various CDW distortions in the AV_3Sb_5 family, including the $3Q$ order and additional in-plane and out-of-plane distortions, highlights the rich complexity of these materials and the interplay between their crystal structures and electronic properties. Further investigations combining experimental and theoretical approaches are essential to unravel the underlying mechanisms driving these CDW transitions and to gain a deeper understanding of the role of Fermi surface nesting and saddle point features in the emergence of these.

The Peierls model, which describes nesting-driven distortions, has been successful in understanding 1D materials. However, when it comes to higher dimensional materials with 2D or 3D connectivity, this model needs to be extended. To assess whether electron response can drive a Peierls phase transition, the susceptibility $\chi(q,\omega)$ is calculated for a given electronic configuration, with a particular focus on the zero-frequency value of the Lindhard response function, $\chi_0(q,\omega=0)$ [23].

Previous studies by Johannes and Mazin [25, 27] have shown that Fermi surface nesting, which can be identified by the divergence in the imaginary part of the Lindhard susceptibility $\chi''(q)$, fails to predict charge density wave (CDW) formations in various 2D materials. The strongest peaks in $\chi''(q)$ often do not correspond to the actual CDW q-vector observed in experiments, and many materials do not undergo CDW transitions despite exhibiting strong Fermi surface nesting peaks. Instead, true electronic instability is represented by peaks in the real part of the susceptibility, $\chi'(q)$. Johannes and Mazin argue that a Fermi surface nesting-

driven CDW distortion can only be attributed to a simple Peierls-like origin if a strong Fermi surface nesting peak in $\chi''(q)$ is also present at the same location in $\chi'(q)$ [25]. This approach was successfully applied to clarify the distortion mechanism in $NbSe_2$, a quasi-2D hexagonal metal with CDW and superconducting transitions, demonstrating similarities to the quasi-2D hexagonal CsV_3Sb_5 compound [4].

Considering the current extensive qualitative discussions surrounding Fermi surface nesting in the AV_3Sb_5 system [20,50,54,55,56,57,58], we aim to provide explicit Fermi surface nesting and Lindhard response calculations for CsV_3Sb_5 in order to determine whether the CDW can be attributed to a clear Peierls-like nesting mechanism.

2.2 Methods

We used the Wien2k full potential code [59] with the Perdew-Burke-Ernzerhof (PBE) [41] approximation to the exchange correlation functional. The spin-orbit interaction was accounted for using the second variational principle, as implemented in the code. We used the structure relaxed with the VASP code[60, 61] where a van-der-Waals correction was added to better approximate the distance between the 2D planes (We employed the PBE functional[41] with D3 correction[62]). The projector augmented wave (PAW) method [60, 61] was employed and relaxations of the ionic positions were conducted using an energy cutoff of 520 eV.; all parameters were identical to Ref. [4]. a and c unit cell parameters were 5.45 Å and 9.35 Å, respectively). We used a dense k-mesh of $20\times20\times9$ for the self-consistent calculation and then a denser mesh of $50\times50\times12$ for calculation of the Fermi surface and the real and imaginary parts of the Lindhard function, taken in both cases in the limit that the frequency goes to zero [25, 27].

2.3 Results and discussion

Our findings are summarized in Figure 2.2. Figure 2.2 (a) displays the calculated $\chi''(q)$ for $E_F = E_F^{DFT}$, where the largest peaks correspond to perfect self-nesting at $q = [0,0]$, $q = [1,0]$, and so on, providing limited information. Additional peaks form a complex pattern of ridges. At the M points with q vectors $[1/2, 0.0]$, $[1/2, 1/2]$, $[0.0, 1/2]$, a peak in the nesting function can be observed, indicated by a red arrow. However, this peak is not isolated; rather, it is part of a larger triangular ridge pattern running along the $\Gamma - M$ lines. These triangular nesting ridges exhibit a finer-grained striped texture, with up to three parallel nesting lines. A nearly circular nesting pattern surrounds the largest trivial peaks. These nesting features are similar for both the $k_z = 0$ and $k_z = 1/2$ planes. In Figure 2.2 (b), the $\Gamma - M$ nesting ridges are shown to manifest in the real part, $\chi'(q)$. The circular ridges also exhibit increased intensity in $\chi'(q)$. Interestingly, the highest intensity peaks in $\chi'(q)$ are associated with the circular ridges and do not occur at M-like q vectors. Furthermore, we conducted Lindhard susceptibility calculations with the saddle point shifted to the Fermi level. The imaginary part and the real part of these calculations for different k_z values are presented in Figure 2.2 (c) and (d), respectively. While the relative peak heights may vary when adjusting the Fermi level, there are no major qualitative differences observed between the Lindhard calculations. These results provide insights into the nesting characteristics and Lindhard response of CsV_3Sb_5, shedding light on the potential nesting-driven mechanisms behind the observed charge density wave formation in the material.

The observed combination of circular and triangular ridges in the Lindhard function aligns with the pattern previously detected in experimental quasi-particle interference measurements [48], and its origin can be elucidated by examining the Fermi surface geometry. Figure 2.3 illustrates the calculated Fermi surfaces for both (a) E_F^{DFT} and (b) E_F^{SP}. In both cases, the qualitative features of the Fermi surface topography are similar, characterized by a central circular Fermi surface pocket surrounded by hexagonal and triangular pockets.

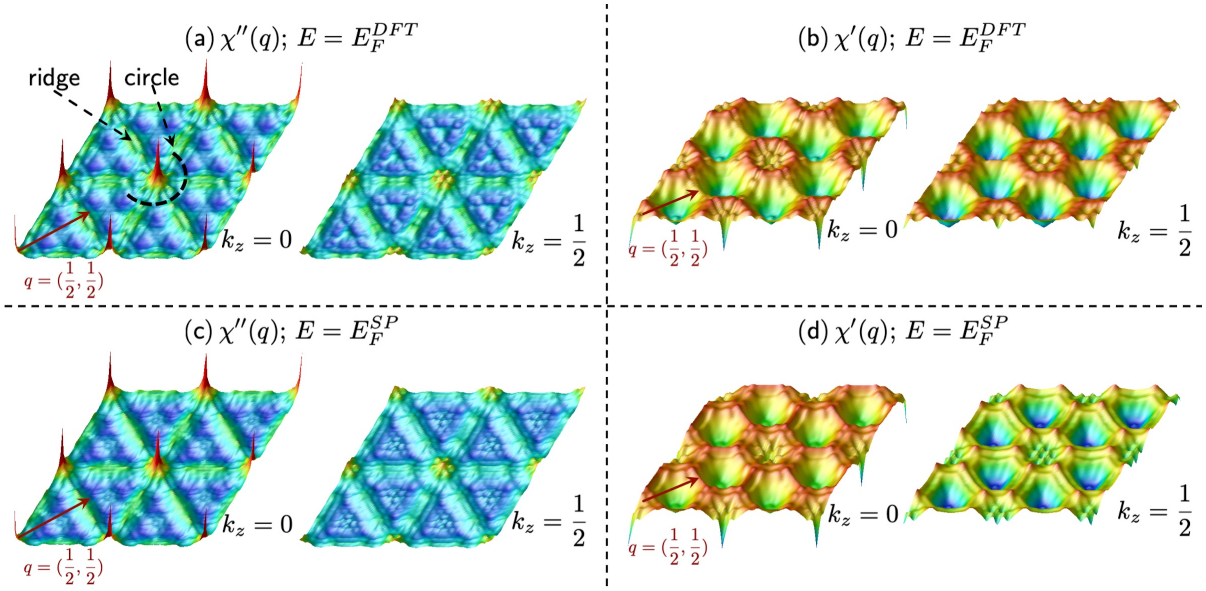

Figure 2.2: Fermi surface nesting and Lindhard response function in CsV_3Sb_5. The imaginary and the real part of the Lindhard susceptibility function at different k_z for the DFT Fermi level electronic structure is presented in (a) and (b), respectively. The imaginary and the real part at the saddle point (SP) energy level are presented in (c) and (d).

The central pocket, predominantly originating from antimony p states, exhibits nesting tendencies with the larger hexagonal pocket, resulting in the formation of the central circular patterns observed in the Lindhard function. On the other hand, the remaining triangular and hexagonal pockets, primarily influenced by vanadium d contributions, display strong two-dimensional nesting behavior along the $\Gamma - M$ direction, as indicated by the green lines. The nesting at the M point is highlighted by a red arrow. Conversely, when considering saddle-point nesting, as depicted in Figure 2.3(b), the overlap between the involved Fermi surface regions is minimal, leading to a negligible impact on the overall Lindhard function.

These findings highlight the connection between the Fermi surface geometry and the observed features in the Lindhard function, providing insights into the underlying mechanisms governing the charge density wave formation in CsV_3Sb_5.

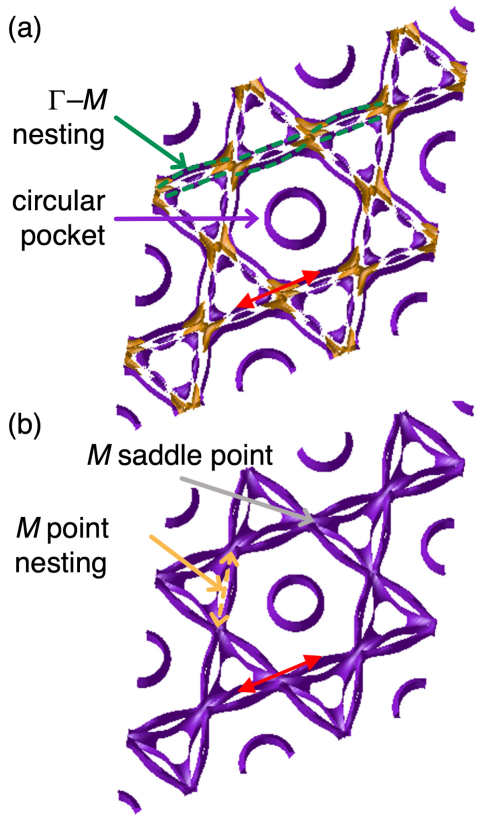

Figure 2.3: Fermi surfaces and origins of nesting. Fermi surfaces are presented at (a) E_F^{DFT} (b) E_F^{SP}. The circular FSN ridges derive from nesting between central circular and hexagonal pockets. The $\Gamma - M$ FSN ridges derive from strong nesting and linear overlap of the triangular and hexagonal regions, highlighted in green. The main M-type FSN vector is highlighted in red for both Fermi level choices, while the weak saddle point nesting at the M-point is indicated in orange in (b). The Figure illustrates that they are multiple type of M-like nesting that we could have in this Fermi surface, and the dominant M-type nesting is not the one between the M saddle points (M point nesting which showed by the orange dashed arrow is not the dominant nesting). The saddle point shows up in Fermiology as extremely 2-D rectangles oriented such the nesting is weak (if even existed).

2.4 Conclusion and summary

The obtained results allow us to draw several conclusions regarding Fermi surface nesting-driven instabilities in CsV_3Sb_5 and other members of the AV_3Sb_5 kagome family, which exhibit similar electronic structures. Firstly, the peaks observed at the M point in the nesting function and the real part of the susceptibility are not singularly strong; rather, they are part of ridges extending along the $\Gamma - M$ direction. This implies that they do not solely drive the electronic instability, although they may contribute to it to some extent. When considering the real part of the Lindhard function, the intensity of the $\Gamma - M$ ridges is comparable to or even weaker than the intensity of the central circular ridge, which arises from the nesting between the central pocket of the Fermi surface (predominantly derived from Sb p orbitals) and the slightly larger hexagonal pocket.

Secondly, Fermi surface nesting appears to be insensitive to the k_z value. Despite slight variations in peak magnitudes, the $\chi''(q)$ and $\chi'(q)$ maps exhibit qualitative similarity at $k_z = 0$ and $k_z = 1/2$ for all calculations. This observation holds not only for high symmetry planes but also for other k_z values, such as $k_z = 1/4$. Consequently, it becomes challenging to argue that either the observed 2-fold or 4-fold c-axial distortions, observed experimentally, can be uniquely favored by the electronic structure instability.

Finally, since the Lindhard function remains relatively unchanged with variations in the Fermi level and k_z value (with the M saddle point located at $k_z = 0$), the kagome saddle point seems to have minimal relevance to the overall nesting behavior. In fact, the Lindhard intensity does not exhibit a preference for the intrinsic V kagome instability associated with the outer pockets of the Fermi surface over the instability involving the central circular Sb pocket.

Zhu *et al.* [26] proposed a classification scheme for charge density waves (CDWs) based on three different formation mechanisms. According to their framework, type-I CDWs follow the Peierls picture, where the transition is driven by Fermi surface nesting. In contrast, type-II

CDWs are associated with q-dependent electron-phonon coupling, while type-III encompasses correlated systems with charge modulations, such as cuprates, where neither Fermi surface nesting nor electron-phonon coupling alone can explain the transition. Overall, our findings support the notion that the charge density waves observed in CsV_3Sb_5 do not arise from a singular instability in the electronic structure and cannot be classified as type-I Peierls-like distortions.

Electron-phonon coupling has been identified as the primary driving force behind the structural instability in $NbSe_2$ [27, 63], and it is likely responsible for the observed ordering in the AV_3Sb_5 family as well. While recent experiments indicate that the phonon transitions in CsV_3Sb_5 [64, 65] may exhibit greater complexity than the previously observed phonon softening in $NbSe_2$, the effects of electron-phonon coupling may still explain the strong influence of chemical doping on the charge density wave in this compound [66, 67].

Calculations performed on CsV_3Sb_5 indicate that the breathing mode distortions in the material do not exhibit a simple link with Fermi surface nesting. The FSN appears to be independent of changes along the k_z direction, which is perpendicular to the kagome layers. Additionally, small shifts in the Fermi level have only a mild impact on the FSN. These findings suggest that the nesting effects on the Fermi surface may not be strongly influenced by specific features in the saddle points, contrary to initial expectations. The lack of a Peierls-like transition signature further supports the notion that the breathing mode distortions in CsV_3Sb_5 do not arise solely from Fermi surface nesting effects. This implies that other factors, such as electron-phonon interactions or complex electronic correlations, may play a role in driving the observed CDW ordering. By examining the Fermi surface nesting and Lindhard susceptibility in CsV_3Sb_5, this study [21] provides insights into the relationship between electronic structure, CDW ordering, and superconductivity in kagome net compounds. The results suggest that the FSN is not solely determined by specific features in the saddle points, challenging previous assumptions. The findings contribute to the ongoing understanding of the intricate behavior of

AV_3Sb_5 materials and their potential for realizing exotic electronic states.

2.5 Acknowledgments

This work was supported by the National Science Foundation (NSF) through Enabling Quantum Leap: Convergent Accelerated Discovery Foundries for Quantum Materials Science, Engineering and Information (Q-AMASE-i): Quantum Foundry at UC Santa Barbara (DMR-1906325). We acknowledge use of the shared computing facilities of the Center for Scientific Computing at UC Santa Barbara, supported by NSF CNS-1725797, and the NSF MRSEC at UC Santa Barbara, NSF DMR-1720256. FK acknowledges the Roy T. Eddleman Center for Quantum Innovation (ECQI) for their support. SMLT. has been supported by the National Science Foundation Graduate Research Fellowship Program under Grant No. DGE-1650114. MDJ acknowledges support by the Office of Naval Research through the U.S. Naval Research Laboratory.

Chapter 3

Tune band structure of CsV_3Sb_5 via Sn doping

[1]The recently reported AV_3Sb_5 (A = K, Rb, Cs) family of kagome metals are candidates for unconventional superconductivity and chiral charge density wave (CDW) order. Both of these phenomena potentially arise from nested saddle points in their band structures close to the Fermi energy. In this study, we use chemical substitution to introduce holes into CsV_3Sb_5 and unveil an unconventional coupling of the CDW and superconducting states. Specifically, we generate a phase diagram for $CsV_3Sb_{5-x}Sn_x$ that illustrates the impact of hole-doping the system and lifting the nearest van Hove singularities (vHs) toward and above E_F. Superconductivity exhibits a non-monotonic evolution with the introduction of holes, resulting in two "domes" peaked at 3.6 K and 4.1 K, along with the rapid suppression of three-dimensional CDW order. The evolution of the CDW and superconducting order is compared with the evolution of the electronic band structure of $CsV_3Sb_{5-x}Sn_x$, where the complete suppression of superconductivity seemingly coincides with the emergence of an electron-like band composed of Sb p_z orbitals pushed above

[1]The contents of this chapter previously appeared in Ref. [66]: Y.M. Oey, B.R. Ortiz, **F. Kaboudvand**, S.D. Wilson, and R. Seshadri, "Fermi Level Tuning and Double-Dome Superconductivity in the Kagome Metals $CsV_3Sb_{5-x}Sn_x$", *Phys. Rev. Mater.* **6** (2022) L041801. Reprinted with permission.

E_F.

3.1 Introduction

Kagome metals, such as the AV_3Sb_5 family, exhibit intriguing electronic structures featuring Dirac points, flat bands, and saddle points, which often lead to electronic instabilities associated with divergences in the density of states at the Fermi level [9, 9, 17, 19, 68, 69, 70]. A wide array of instabilities has been predicted, including bond density wave order, charge fractionalization, charge density waves (CDW), and superconductivity (SC) [9, 9, 17, 19, 68, 69, 70]. Surprisingly, these instabilities can be fine-tuned through minor adjustments in the band filling [8, 9, 71, 72, 73]. For instance, when you have band fillings around $5/4$ electrons per band [8, 9, 71, 72, 73], it tends to load up those nested van Hove singularities (vHs), which kickstarts the CDW order. In some cases, it even sparks some pretty unconventional superconductivity.

The recently discovered group of AV_3Sb_5 kagome metals (A= K, Rb, Cs) [3] may embody this physical mechanism. Each of these materials showcases experimental evidence linked to CDW order [4, 49, 74, 75, 76, 77]. Interestingly, these signatures are succeeded by the coexistence of superconductivity at low temperatures [4, 75, 78]. When subjected to hydrostatic pressure, the relationship between CDW instability and superconductivity in AV_3Sb_5 takes on an unconventional character [79, 80], yet the exact impact of the pressure-modified band structure on their interplay remains a subject of ongoing exploration. In particular, unraveling the respective roles of the vHs, primarily composed of V d-orbital states near the M-points, and the electron-like band originating from Sb-states at the Γ-point within the CDW and SC mechanisms is pivotal to developing a microscopic understanding of their coupling.

Introducing additional carriers through doping presents an attractive method for adjusting these characteristics concerning the Fermi level while also investigating the connection between CDW and SC states. By shifting the positions of the vHs and the Γ pocket in relation to E_F and

examining the evolution and interplay of the CDW and SC phase transitions, valuable insights into the origins of each state can be gleaned. A recent investigation involving oxidized thin flakes of CsV_3Sb_5, for example, demonstrates that hole-doping at the Cs site can boost T_C while concurrently suppressing CDW order [81]. Furthermore, DFT calculations reveal that hole-doping propels the vHs in the opposite direction relative to E_F compared to the effect of external hydrostatic pressure [82]. Considering the peculiar coupling between SC and CDW states observed under variable pressure [80], conducting a systematic exploration of hole-doping effects promises to offer a vital experimental perspective on comprehending this unconventional coupling.

In this chapter, we explore the impact of hole-doping on the CDW and SC states in $CsV_3Sb_{5-x}Sn_x$ across the range of $0 \leq x \leq 1.5$. The process of hole-doping is achieved through the substitution of Sn atoms onto the Sb sites. Notably, Sn and Sb have strikingly similar sizes, which results in minimal coincidental steric effects on the band structure. As we introduce holes into the system, the CDW state undergoes rapid suppression, with the three-dimensional CDW order vanishing at approximately $x = 0.06$. Concurrently, there is an augmentation in the superconducting phase, reaching its peak at $T_C = 3.6$,K when $x = 0.03$ within the CDW state. However, as the CDW order is fully suppressed, the superconducting transition temperature subsequently decreases. Continuing the hole-doping process beyond the point of CDW order suppression unveils a second peak in T_C at $x = 0.35$, with a maximum value of 4.1,K. This is followed by a gradual weakening and eventual disappearance of bulk superconductivity beyond $x = 0.5$.

The combination of density functional theory (DFT) calculations and nuclear quadrupolar resonance measurements sheds light on the strong preference for Sn to occupy Sb sites within the kagome plane [82]. DFT models predict that Sn substitution on this site raises the energy of the Sb p_z electron-like band at Γ above E_F, coinciding with the vanishing of bulk superconductivity. Importantly, small changes are predicted in the energies of the vHs for doping levels sufficient

to suppress CDW order, suggesting the importance of Sb-states in stabilizing both phases [82].

3.2 Methods

For our electronic state calculations, we conducted first-principles analyses utilizing density functional theory (DFT) within the Vienna ab-initio Simulation Package (VASP), as previously outlined in references [83, 84]. To facilitate these calculations, we employed the projector augmented wave (PAW) method [38, 85] and conducted ionic relaxation procedures with an energy cutoff of 520 eV. Our investigation encompassed the automatic generation of reciprocal space k-point meshes at a density of 55 Å^{-1} along each reciprocal lattice vector.

The central focus of our analysis revolved around the computation of the band structure along primary paths, which were determined based on high symmetry points, as per the definitions by Setyawan and Curtarolo[86]. To gain a comprehensive understanding of the electronic properties, we visualized the density of states (DOS) and band structures using the sumo package[87].

It's important to note that the CsV_3Sb_5 structure comprises five distinct sites for Sb atoms, including two sites with unique and symmetrically distinct characteristics: site 1 within the kagome plane (WKP) and site 2 outside of the kagome plane (OKP). Those sites presented in Figures 3.1. In the scope of our study, we conducted calculations for both scenarios, considering the placement of Sn atoms within the WKP and at one of the OKP sites.

We synthesized powder samples of $CsV_3Sb_{5-x}Sn_x$ for a range of $0 \leq x \leq 1$ in batches of 6–7 grams. This synthesis involved a combination of ball milling and high-temperature sintering . To analyze the structural characteristics, we employed synchrotron powder x-ray data acquired at Argonne National Laboratory (APS, 11-BM) and conducted laboratory x-ray powder diffractometry using a Panalytical Empyrean instrument. In addition, a Hitachi TM4000Plus scanning electron microscope (SEM) equipped with energy-dispersive x-ray spectroscopy (EDS) capabilities was employed.

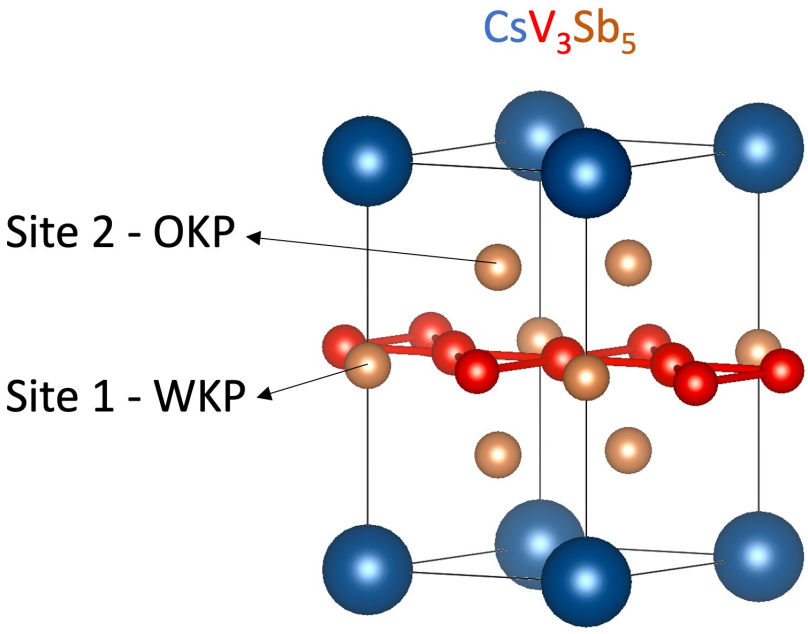

Figure 3.1: Crystal structure of CsV_3Sb_5. Although there are five sites for Sb, there are only two unique, and symmetrically distinct sites, site 1 within the kagome plane (WKP) and site 2 the outside of the kagome plane (OKP) which labeled in the picture.

We gathered magnetization data using a Quantum Design Magnetic Property Measurement System (MPMS) and acquired electrical resistivity data with a Quantum Design Physical Property Measurement System (PPMS). We conducted room temperature ^{121}Sb zero-field Nuclear Quadrupole Resonance (NQR) measurements using a custom NMR spectrometer. For additional details, including relevant references, please refer to the Supplemental Material accompanying our paper in this topic[66], which also contains references to [38, 85, 86, 87, 88, 89, 90, 91, 92].

3.3 Results and discussion

At room temperature, all $CsV_3Sb_{5-x}Sn_x$ compositions within the range $0 \leq x \leq 1$ adopt the hexagonal $P6/mmm$ structure, similar to the pristine CsV_3Sb_5, characterized by an ideal kagome network of V atoms, as depicted in Figure 4.1(a). Polycrystalline samples in this composition

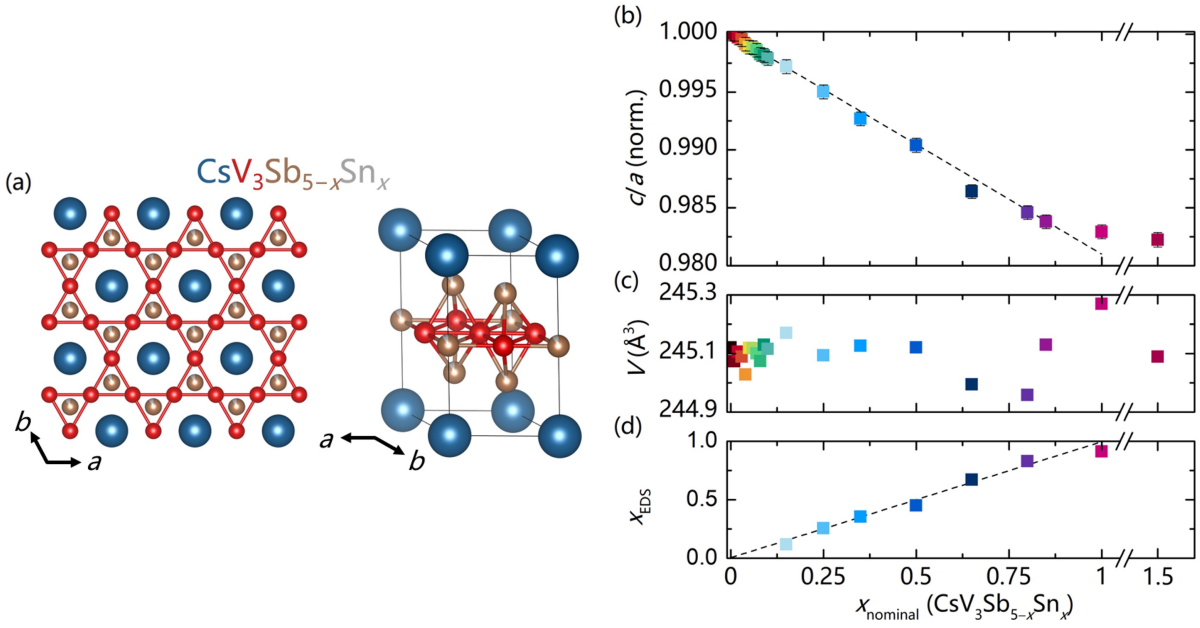

Figure 3.2: (a) The crystal structure of $CsV_3Sb_{5-x}Sn_x$ preserves the parent CsV_3Sb_5 (*P6/mmm*) configuration. Sn atoms are capable of substituting on either the Sb1 or Sb2 sublattices, with our investigations at low doping revealing a predilection for Sn to occupy the Sb site within the V kagome plane. (b-c) The integration of Sn into $CsV_3Sb_{5-x}Sn_x$ provokes a gradual decrease in the c/a ratio, culminating in the cessation of solid solubility at $x = 1$. (d) For samples with concentrations surpassing the EDS sensitivity threshold, the nominal Sn content closely aligns with the measured Sn content. Error bars are displayed, unless their dimensions are smaller than the associated data point size. The distinctive colors employed in these figures consistently correspond to sample compositions.

range remain single-phase, although a secondary phase emerges at $x = 1.5$, signifying the termination of the solid solution. To determine the impact of Sn content on the unit cell, Pawley fits were employed on powder diffraction data. Figures 4.1(b-c) illustrate the normalized c/a ratio and the cell volume as functions of Sn content. As Sn content increases, a experiences an increment, while c undergoes a reduction in near-perfect compensation, ultimately leading to a cell volume that remains virtually unaltered with respect to Sn content. Minimal volume fluctuations, less than 0.16%, can be attributed to uncertainties in chemical composition and structural refinement.

The linear trend observed in the c/a ratio is reminiscent of Vegard's Law, suggesting that Sn

integrates into the parent structure as a solid solution up to approximately $x = 1$, beyond which the c/a ratio plateaus. Figure 4.1(d) demonstrates that the measured Sn content (determined *via* EDS) closely aligns with the nominal Sn content. While Rietveld refinements of X-ray data confirm the single-phase nature of the powders, limited scattering contrast between Sb and Sn hinders the ability to precisely determine whether Sn is evenly distributed across both the Sb1 and Sb2 sites or if there is a preference for occupation of a specific sublattice. DFT calculations indicate a preference of approximately 10 meV/atom for Sn to selectively substitute the Sb1 site (within the kagome plane), a preference further corroborated by nuclear quadrupole resonance (NQR) measurements, as discussed later.

Undoped CsV_3Sb_5 single crystals exhibit a superconducting transition at $T_C = 2.5$ K [4, 81] and a charge density wave transition at $T^* = 94$ K [74, 76]. This charge density wave transition induces a structural distortion, resulting in a $2 \times 2 \times 4$ enlarged unit cell. Within this unit cell, layers of kagome nets undergo distortion, forming Star-of-David and Tri-hexagonal structures [50, 74, 93]. It's worth noting that polycrystalline samples exhibit equivalent transition temperatures; however, the transitions are broader in comparison to single crystals [4]. This broadening is primarily attributed to the heightened sensitivity of powders to specific synthesis conditions and the influence of strain effects.

In the case of pure CsV_3Sb_5 powder synthesized in this study, an onset T_C of 2.70 K and a midpoint T_C of 2.07 K are observed. As Sn is introduced into the matrix, Figure 3.3(a) elucidates the progression of superconductivity in two distinct doping ranges ($x = 0$ to 0.03 and $x = 0.1$ to 0.35). Notably, all superconducting samples exhibit $4\pi\chi_v \approx -1$ in magnetization, with values slightly exceeding unity being attributed to packing density errors. Data are normalized to -1 for the sake of ease in comparison.

The influence of Sn on T_C becomes immediately evident. With an increase in Sn content to $x = 0.03$, T_C experiences a notable upturn, reaching a local maximum of 3.6 K. Subsequently, T_C exhibits a decline with continued hole-doping, followed by the emergence of a second

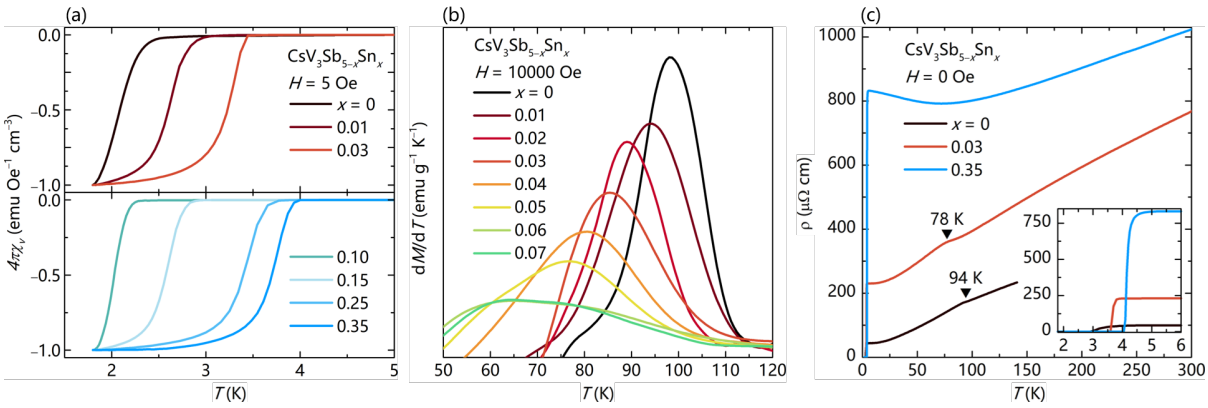

Figure 3.3: (a) The superconducting T_C measured under a field of $H = 5$ Oe shows a systematic shift to higher temperature in the compositions leading to the two T_C maximums. The superconducting fraction is normalized to account for errors in mass and packing fraction so all data have a minimum of -1, the theoretical minimum. (b) dM/dT for compositions $x \leq 0.06$ show a decrease in CDW T^*, and this transition disappears for greater Sn compositions. (c) Resistivity data also show this enhancement in T_C, and the low-T, normal state resistivity for $x = 0.35$ is about 4 times higher than $x = 0.03$.

superconducting dome with a peak T_C of 4.1 K at $x = 0.35$. Beyond $x > 0.5$, superconductivity occupies only a partial volume fraction, and it is entirely absent at $x = 0.85$. Further detailed susceptibility measurements are provided in the supplemental information of our paper [66].

The way CDW order evolves as we introduce holes via Sn doping becomes clear when we look at changes in magnetization. We use a metric called the inflection point in magnetization, represented by the peak in the derivative dM/dT, to track when the three-dimensional CDW order kicks in.

When we add light holes through Sn substitution, something interesting happens. The CDW transition gets broader and shifts to lower temperatures. In its original, undoped state, the CDW transition occurs at 98.01 K, but as we introduce Sn, this peak in dM/dT drops to below 80 K by the time we reach a Sn concentration of $x = 0.04$. This suggests that the CDW transition is significantly altered and suppressed as we dope with Sn.

Beyond a Sn concentration of $x > 0.05$, things get a bit fuzzy. The magnetization doesn't show distinct CDW transition signatures, hinting that the CDW anomaly becomes quite broad

and might continue to be suppressed with even higher Sn doping.

What's interesting is that at the first maximum of the initial superconducting dome ($x = 0.03$), the superconducting and CDW states coexist. However, at the second peak in superconducting critical temperature (T_C) for higher Sn content ($x = 0.35$), this coexistence disappears, happening well after the CDW order has been suppressed. This complex relationship between CDW and superconducting transitions raises intriguing questions that call for further investigation, possibly involving single crystals.

In a nutshell, these results highlight the intricate behavior of CDW order when we introduce Sn via hole-doping in CsV_3Sb_5. This opens up possibilities for exploring new phase boundaries and phase transitions that deserve closer scrutiny and understanding.

Figure 3.3(c) presents electrical resistivity measurements performed on samples at both peak T_C values ($x = 0.03$ and $x = 0.35$). These measurements nicely align with the critical temperatures (T_C) that we identified using magnetization data. Additionally, for the sample at $x = 0.03$, we can clearly spot the onset of the charge density wave (CDW) transition.

The introduction of Sn into the mix results in some remarkable changes in electrical resistivity. Just before the onset of superconductivity, we see a significant jump in resistance. For instance, in the undoped state ($x = 0$), the resistance is a modest 50 $\mu\Omega$-cm. However, as we add Sn and reach $x = 0.03$, we observe a noteworthy increase to 250 $\mu\Omega$-cm, which marks the first peak in superconducting critical temperature (T_C). When we reach $x = 0.35$, the resistance spikes even higher at 800 $\mu\Omega$-cm, corresponding to the second peak in T_C. This substantial shift in resistance, especially around the CDW transition temperature, underlines the significant impact of Sn doping on the material's electronic properties.

In summary, as illustrated in Figure 4.4, a phase diagram provides a visual representation of how Sn-substitution affects both superconductivity (SC) and charge density wave (CDW) orders. Notably, we observe a two-dome structure in the T_C values, indicating that Sn doping has a profound influence on the superconducting transitions in this system.

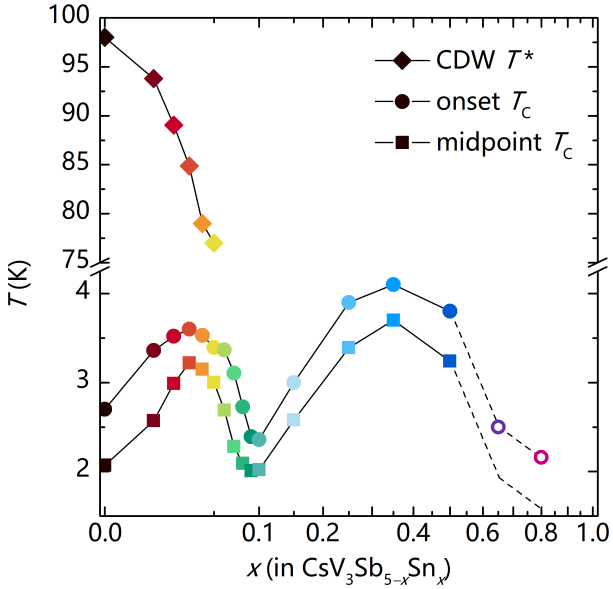

Figure 3.4: Hole-doping phase diagram for $CsV_3Sb_{5-x}Sn_x$. The double-dome structure is clearly evident, as is the depression of the CDW ordering temperature. T_C shows two maxima at $x = 0.03$ and at $x = 0.35$ and the CDW state disappears by $x = 0.06$. We note that the first T_C maximum occurs while the CDW is still present, and the CDW vanishes once T_C is already declining again $x > 0.03$. For $x \geq 0.65$, the volume fraction of superconductivity decreases and the onset T_Cs are represented with open circles.

Now, let's delve into the effects of Sn substitution within the CsV_3Sb_5 lattice. This substitution process allows us to replace nearly 1/5 of the total Sb atoms with Sn, and the resulting changes in the electronic structure are quite fascinating. Figure 4.5(a) provides us with a snapshot of the electronic structure of pure CsV_3Sb_5, highlighting the range of achievable Fermi levels (E_F) with a loss of 1 electron per unit cell, as indicated by the gray shaded region. In a simple rigid band shift approximation, introducing Sn should, in theory, enable us to tune E_F across various van Hove singularities (vHs) and Dirac points near the M- and K-points, respectively. However, it's essential to consider the orbital effects and the complexities introduced by Sn substitution.

Figure 4.5(c) illustrates a hypothetical scenario where Sn is substituted on the Sb2 sublattice (out of the kagome plane). In this case, apart from the expected Fermi level shift (notice how the vHs crossing near the M-point is now situated approximately 0.2 eV *above* E_F), there's a

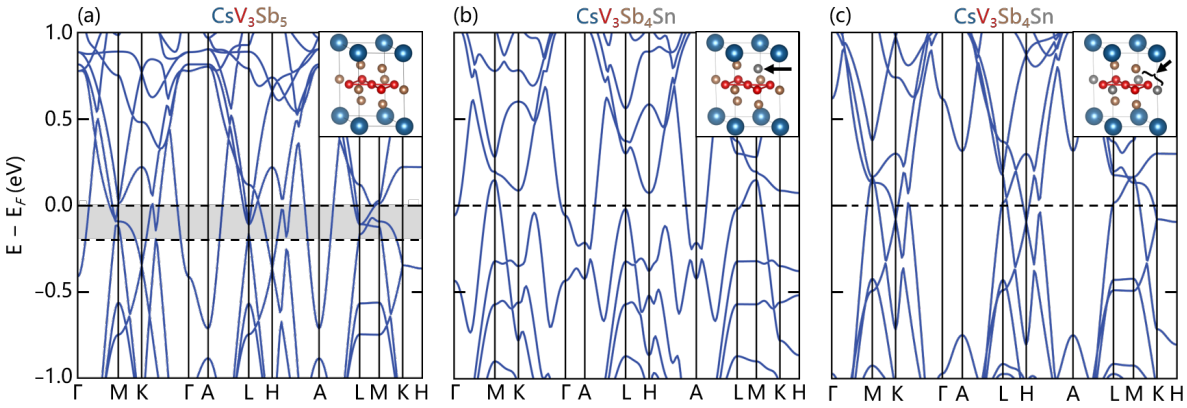

Figure 3.5: (a) DFT calculations illustrate the range of allowable Fermi levels for CsV_3Sb_5 under the rigid band approximation when substituting one Sn atom per formula unit. (b) We delve into the band structure of CsV_3Sb_4Sn, focusing on scenarios where one Sn atom is swapped within the kagome plane (WKP). Most of the electronic structure remains unchanged, except for the Γ pocket, where the Sb band, previousl occupied, is replaced by an unoccupied Sn band positioned above E_F. (c) This time, our calculations explore the band structure of CsV_3Sb_4Sn when one Sn atom takes the place of an Sb atom located outside of the kagome plane (OKP). Notably, we observe a substantial reconstruction of many bands, especially in regions around K, H, and K-Γ.

significant reconstruction observed around the K, L, and H points. Interestingly, the electron-like band at Γ remains intact in this scenario. However, if Sn occupies the Sb1 sublattice within the kagome plane, the overall electronic structure relative to CsV_3Sb_5 is relatively preserved, mimicking a rigid band shift model. But there's a crucial exception— the Sb-derived Γ-pocket disappears and is replaced by an electron-like Sn-band situated far above E_F.

Figure 3.6 presents more detailed insights into the orbital contributions to these electronic band structures. The colorized bands generated by DFT calculations provide a visual representation of the orbital contributions originating from the constituent elements: V, Sb, and Sn. In the case of CsV_3Sb_5, the Γ pocket primarily arises from the involvement of the Sb p_z orbitals. These orbitals play a crucial role in shaping the electronic structure of this material as presented in Figure 3.6(a). Conversely, when we consider the fully substituted structure with Sn atoms embedded within the kagome plane, the electronic landscape is significantly influenced by the

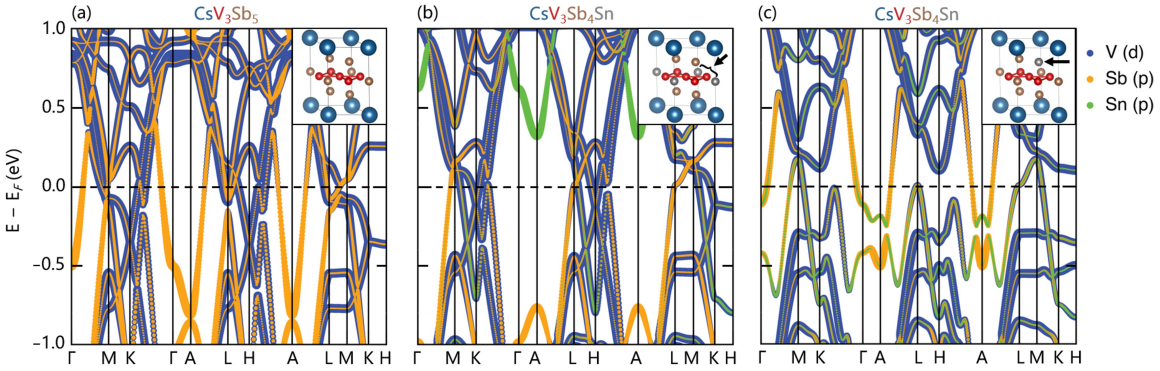

Figure 3.6: Colorized bands structure from DFT calculations show the orbital contributions from V, Sb, and Sn. (a) The Γ pocket in CsV_3Sb_5 primarily originates from the Sb p_z orbitals. (b) and (c) present the band structure of CsV_3Sb_4Sn when we substitute Sb with Sn, whit-in and out of the kagome plane. In contrast of the CsV_3Sb_5, the fully substituted structure with Sn atoms integrated into the kagome plane is predominantly shaped by the Sn p_z orbitals.

Sn p_z orbitals, compare 3.6(b) and (c) which is band structure for CsV_3Sb_4Sn with CsV_3Sb_5 that presented in 3.6 (a).

To elucidate the influence of Sn-doping on the band structure, nuclear quadrupolar resonance (NQR) measurements were conducted, confirming a marked preference for Sn occupation on the Sb1 sites within the kagome plane. This finding is in accordance with density functional theory (DFT) calculations, which reveal a modest energy favorability for Sn residing on the Sb1 site. With the doping site identified, supercell calculations for fractional in-plane Sb substitution were carried out. These calculations indicate that as the Sn content increases, the electron-like band at Γ is shifted above the Fermi level (E_F), particularly near $x \approx 0.5$, coinciding with the attenuation of bulk superconductivity. The calculations presented in 3.7 This observation suggests a partial dependence of superconductivity in CsV_3Sb_5 on the Sb p_z-derived orbitals, aligning with prior findings from pressure studies [94].

At lower Sn-doping levels, the emergence of an intermediate peak in T_C reflects the intricate interplay between the Sb-states at Γ and the V d-states responsible for driving the charge density wave (CDW) order. Supercell calculations reveal a relatively modest shift in the van

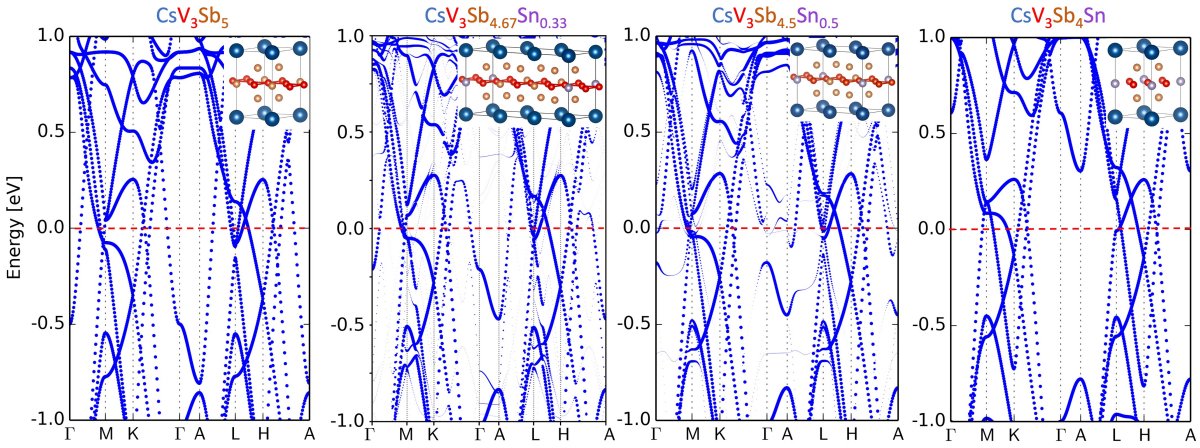

Figure 3.7: Supercell DFT calculations for $x = 0.33$ and $x = 0.5$ illustrate the evolution of band structures as the Sn content increases. The Γ pocket ascends beyond the Fermi level (E_F) at $x = 0.5$, while the van Hove singularity at the M-point crosses E_F at $x = 1$.

Hove singularities (vHs) at the M-point, transitioning from approximately -0.072 eV below E_F for $x = 0$, to -0.047 eV for $x = 0.33$, and -0.042 eV for $x = 0.5$, before surging 0.083 eV above E_F at $x = 1$. The slight shift in the anticipated vHs energies toward E_F at a modest $x = 0.05$ substitution fails to elucidate the rapid suppression of the CDW state at this doping level, implying a complex interplay of energy scales governing the CDW state. This observation aligns with the rapid CDW suppression under hydrostatic pressure [79, 80]. However, the two superconducting (SC) domes encountered during hole-doping appear distinct from those induced by pressure. Superconductivity in crystals nominally doped between the SC domes maintains a well-defined transition, in contrast to the weak SC observed in pressure studies. Further investigation is needed to explore the distinctions between pressure (pushing vHs away from E_F) and hole-doping (drawing vHs closer to E_F), with the goal of comprehending the parallels between the hole-doping and pressure-driven phase diagrams.

3.4 Conclusion and summary

The introduction of hole-doping through the chemical substitution of Sn into the CsV_3Sb_5 compound leads to a remarkably intricate electronic phase diagram. This diagram reveals the emergence of two distinct superconducting (SC) regions, resembling two domes, each with its unique characteristics. The first dome of superconductivity is particularly intriguing because it coexists with the charge density wave (CDW) order, a phenomenon that has been predicted for superconductors situated slightly away from the van Hove singularities (vHs). The appearance of a peak in the critical temperature (T_C) before the CDW order is fully suppressed is a noteworthy observation, highlighting the complex interplay between the Sb p_z states, CDW, and superconductivity in these materials. We applied first-principle study to understand how the Sb p_z states intertwine with both CDW order SC in these materials. Our results demonstrate that small changes in the electronic structure achieved through carrier doping can have dramatic impacts on SC and CDW orders in CsV_3Sb_5 and provide a elegant chemical means to tune the competition between these states in the new AV_3Sb_5 class of kagome superconductors. The results of this study has been published [66] which opens up new avenues for exploring and understanding these unique materials and the exotic physical phenomena they exhibit.

3.5 Acknowledgments

This work was supported by the National Science Foundation (NSF) through Enabling Quantum Leap: Convergent Accelerated Discovery Foundries for Quantum Materials Science, Engineering and Information (Q-AMASE-i): Quantum Foundry at UC Santa Barbara (DMR-1906325). The research reported here made use of shared facilities of the NSF Materials Research Science and Engineering Center at UC Santa Barbara DMR-1720256, a member of the Materials Research Facilities Network (www.mrfn.org). Use of the Advanced Photon Source

at Argonne National Laboratory was supported by the U.S. Department of Energy, Office of Science, Office of Basic Energy Sciences, under Contract No. DE-AC02-06CH11357. YMO is supported by the National Science Foundation Graduate Research Fellowship Program under Grant No. DGE-1650114. BRO is supported by the California NanoSystems Institute through the Elings Fellowship program. FK acknowledges the Roy T. Eddleman Center for Quantum Innovation (ECQI) for their support. Work at Brown was supported in part by the the National Science Foundation grant No. DMR-1905532 and funds from Brown and University of Bologna.

Chapter 4

Tuning charge density wave order and superconductivity in the kagome metals $KV_3Sb_{5-x}Sn_x$ and $RbV_3Sb_{5-x}Sn_x$

[1]The family of AV_3Sb_5 (A = K, Rb, Cs) kagome metals exhibits charge density wave (CDW) order, proposed to be chiral, followed by a lower temperature superconducting state. Recent studies have proposed the importance of band structure saddle points proximal to the Fermi energy in governing these two transitions. Here, we show the effects of hole doping achieved via chemical substitution of Sn for Sb on the CDW and superconducting states in both KV_3Sb_5 and RbV_3Sb_5 and generate a phase diagram. Hole doping lifts the Fermi pocket and van Hove singularities toward E_F, causing the superconducting T_C in both systems to increase to about 4.5 K, while rapidly suppressing the CDW state.

[1]The contents of this chapter previously appeared in Ref. [95]: Y. M. Oey, **F. Kaboudvand**, B. R. Ortiz, R. Seshadri, and S. D. Wilson, "Tuning Charge-Density Wave Order and Superconductivity in the Kagome Metals $KV_3Sb_{5-x}Sn_x$ and $RbV_3Sb_{5-x}Sn_x$", *Phys. Rev. Mater.* **6** (2022) 074802. Reprinted with permission.

4.1 Introduction

The AV_3Sb_5 (A: K, Rb, Cs) class of kagome superconductors [3,4,49,75] are proposed to host both unconventional charge density wave (CDW) [46, 56, 96] and superconducting (SC) states [71, 97, 98], making them promising candidates for realizing these two intertwined states within a host, forming a pair density wave state [77, 99, 100, 101]. Investigations into this coupling have included computational studies exploring the effects of small alterations in the electronic band structures on the SC and CDW order parameters [82, 102], alongside experimental approaches involving the application of external hydrostatic pressure [79, 80, 103, 104] and hole doping on various sites [66, 67, 105].

The electron pocket comprising Sb p_z orbitals at the Γ point and saddle points arising from V d-orbitals at the M-points are believed to play pivotal roles within the SC and CDW states. Consequently, gaining insights into their behaviors under external perturbations such as pressure and chemical doping is critical. Recently, the effect of hole doping in CsV_3Sb_5 with Sn substituting Sb was reported, revealing a double superconducting dome under light hole-substitution [66]. As discussed in chapter 3, the termination of the second dome was attributed to the lifting of the Γ pocket above the Fermi energy (E_F) and the removal of the Sb p_z orbitals from the Fermi surface. However, the formation of the first dome remains somewhat anomalous. Within the first SC dome, the CDW order rapidly vanishes at doping levels corresponding to only a slight movement of the van Hove singularities (vHs) at the M point toward E_F.

Curiously, while applied external pressure shifts the M saddle points away from E_F, resulting in a similar phase diagram, it suggests a delicate balance of energy scales within the unperturbed parent structure [80, 82], with the removal of the CDW state predominating in governing the formation of the first SC dome.

In contrast to the aforementioned observations, pressure studies of KV_3Sb_5 and RbV_3Sb_5 have reported only a single superconducting dome, coinciding with the suppression of the CDW

order [79, 103]. However, studies examining carrier-induced perturbations in these variants remain unexplored. To further investigate the similarities between pressure-induced and carrier-induced perturbations and the interplay between CDW and SC orders, this study presents the effect of hole doping AV_3Sb_5 with solid solutions, where A = K, Rb.

In both systems, only one superconducting dome is observed, contrasting with $CsV_3Sb_{5-x}Sn_x$, although a similar rapid CDW suppression is noted. The solubility limit of Sn in KV_3Sb_5 is the lowest within the family, with phase separation observed at $x = 0.30$. Conversely, RbV_3Sb_5 supports up to $x = 0.70$ of Sn replacing Sb. While differences in solubility can be attributed to A cation size effects, the disparity between the single-dome hole-doping phase diagrams of KV_3Sb_5 and RbV_3Sb_5 relative to the double-dome phase diagram of CsV_3Sb_5 suggests a distinction in the parent CDW state among the three materials. The potential origins of these distinctions are further discussed.

4.2 Methods

For our electronic state calculations, we conducted first-principles analyses utilizing density functional theory (DFT) within the Vienna ab-initio Simulation Package (VASP), as previously outlined in references [83, 84]. To facilitate these calculations, we employed the projector augmented wave (PAW) method [38, 85] and conducted ionic relaxation procedures with an energy cutoff of 520 eV. Our investigation encompassed the automatic generation of reciprocal space k-point meshes at a density of 55 $Å^{-1}$ along each reciprocal lattice vector.

The central focus of our analysis revolved around the computation of the band structure along primary paths, which were determined based on high symmetry points, as per the definitions by Setyawan and Curtarolo[86]. To gain a comprehensive understanding of the electronic properties, we visualized the density of states (DOS) and band structures using the sumo package[87]. To gain deeper insights, we further examined the Fermi surface and its topology by integrating the

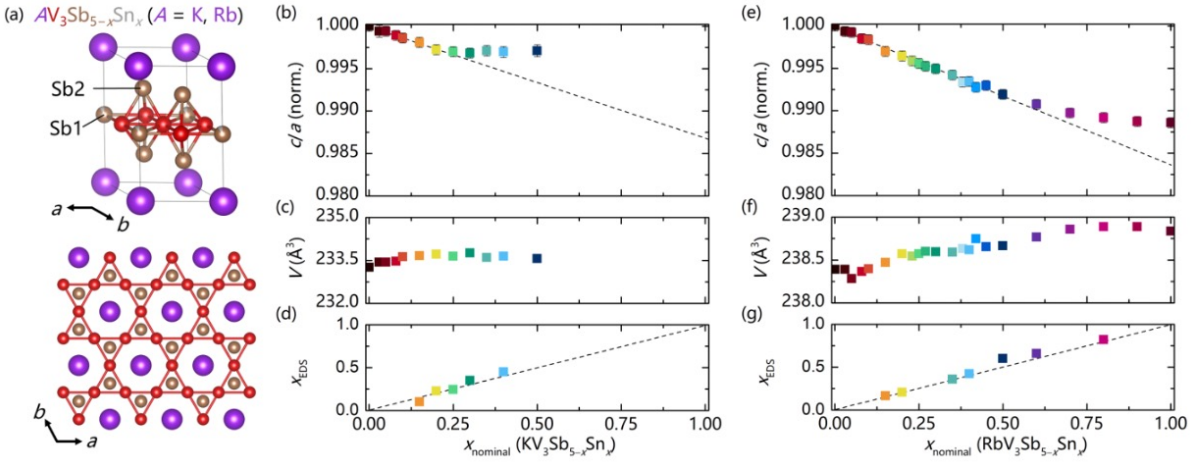

Figure 4.1: (a) $AV_3Sb_{5-x}Sn_x$ crystallizes in the parent AV_3Sb_5 (*P6/mmm*) structure. It is noteworthy that while Sn could theoretically substitute either the Sb1 or Sb2 sites, studies on $CsV_3Sb_{5-x}Sn_x$ have demonstrated the preferential substitution of Sn in the in-plane kagome Sb1 site. (b-c) The integration of Sn into $KV_3Sb_{5-x}Sn_x$ results in a decrease in the c/a ratio, and the solubility limit of Sn is found to be at $x \approx 0.25$, beyond which the c/a ratio deviates from the linear trend. This change indicates a potential disruption of the crystal structure upon exceeding the solubility limit. (e-f) The solubility limit of Sn in $RbV_3Sb_{5-x}Sn_x$ is relatively higher, approximately at $x \approx 0.70$. (d, g) Comparisons between the nominal Sn content and the measured Sn content, considering the EDS sensitivity threshold, demonstrate good agreement. Small error bars are omitted where they are smaller than the associated point size for clarity.

Fermi surface over the Brillouin zone. The calculated Fermi surface maps were generated using the electronic structure visualization toolkit (VESTA) [31].

Powder samples of $KV_3Sb_{5-x}Sn_x$ and $RbV_3Sb_{5-x}Sn_x$ for $0 \leq x \leq 1$ were synthesized as described in previous chapter and the paper [66]. Structural analysis was performed via a Panalytical Empyrean laboratory x-ray powder diffractometer. The diffractometer provided a comprehensive understanding of the crystallographic information, such as the lattice parameters, crystal structure, and any potential structural phase transitions. A Hitachi TM4000Plus scanning electron microscope (SEM) was used to perform energy-dispersive X-ray spectroscopy (EDS), allowing for the elemental analysis of the samples. The EDS results provided crucial information regarding the elemental composition and distribution within the samples. A Quantum Design Magnetic Property Measurement System (MPMS) was utilized to collect magnetization data, allowing for the detailed characterization of the magnetic properties of the samples, including any magnetic phase transitions, hysteresis effects, and magnetic anisotropy. Additionally, a Quantum Design Physical Property Measurement System (PPMS) Dynacool was employed for resistivity measurements, enabling a comprehensive analysis of the electrical properties of the samples, such as resistivity, electrical conductivity, and any potential electronic phase transitions.

4.3 Experimental and computational results

$AV_3Sb_{5-x}Sn_x$ all adopt the parent hexagonal $P6/mmm$ structure at room temperature, with the V atoms forming an ideal kagome network. Studies based on ^{121}Sb nuclear quadrupole resonance (NQR) and DFT calculations on $CsV_3Sb_{5-x}Sn_x$ have revealed the preference of Sn atoms for the Sb1 sublattice site in the kagome plane [66]. Given the structural similarities in all AV_3Sb_5 compounds, we assume that the Sn atoms occupy the Sb1 sublattice for A = K, Rb as well, which was in great agreement with our DFT calculations results. For $KV_3Sb_{5-x}Sn_x$,

the polycrystalline samples were found to be single phase up to $x \leq 0.25$. Similarly, for $RbV_3Sb_{5-x}Sn_x$, the polycrystalline samples were single phase up to $x \leq 0.7$, beyond which the solid solution limit was reached, leading to the observation of secondary phases in both families.

The powder diffraction data were subjected to fitting using the Pawley method to investigate changes in the unit cell with varying Sn content. Consistent with the observations in $CsV_3Sb_{5-x}Sn_x$, the parameter a increases as c decreases with the increasing Sn content in both A = K and Rb, as depicted in Figure 4.1(b,e). Furthermore, the volume was found to be independent of the Sn content (Figure 4.1(c,f)). The solubility limit of Sn was clearly reached when the c/a ratio deviated from its linear trend (around $x \approx 0.30$ for $KV_3Sb_{5-x}Sn_x$ and $x \approx 0.70$ for $RbV_3Sb_{5-x}Sn_x$), leading to the emergence of a secondary phase in the powder diffraction data. Energy-dispersive X-ray spectroscopy (EDS) was performed on samples with critical Sn content to confirm the nominal Sn content (Figure 4.1(d, g)).

Single crystal KV_3Sb_5 exhibits a superconducting T_C of 0.93 K [75]. However, in the case of polycrystalline KV_3Sb_5, the T_C remains below 1.8 K, which is the lowest temperature achievable on the MPMS. With the incorporation of Sn, the superconducting transition temperature increases, becoming detectable at $x = 0.03$. As illustrated in Figure 4.2(a), the evolution of the superconducting transition continues up to $x = 0.25$, where T_C reaches a maximum of 4.5 K. Beyond this Sn content, the appearance of a secondary phase prevents the observation of a suppression of superconductivity within the solid solution of $KV_3Sb_{5-x}Sn_x$. RbV_3Sb_5 exhibits similar behavior, with undoped crystals displaying a T_C of 0.92 K [78]. Although the superconducting transition cannot be detected by an MPMS, it becomes discernible at 1.93 K for $x = 0.05$, gradually increasing to a peak of 4.5 K at $x = 0.40$, as depicted in Figure 4.2(c). Subsequently, for $x > 0.40$, T_C decreases to 3.55 K until a distinct secondary phase emerges. The superconducting volume fractions are approximately $4\pi\chi_v \approx -1$ and have been normalized to -1 for easy comparison. Any slight deviations from this ideal value can be attributed to errors in packing density.

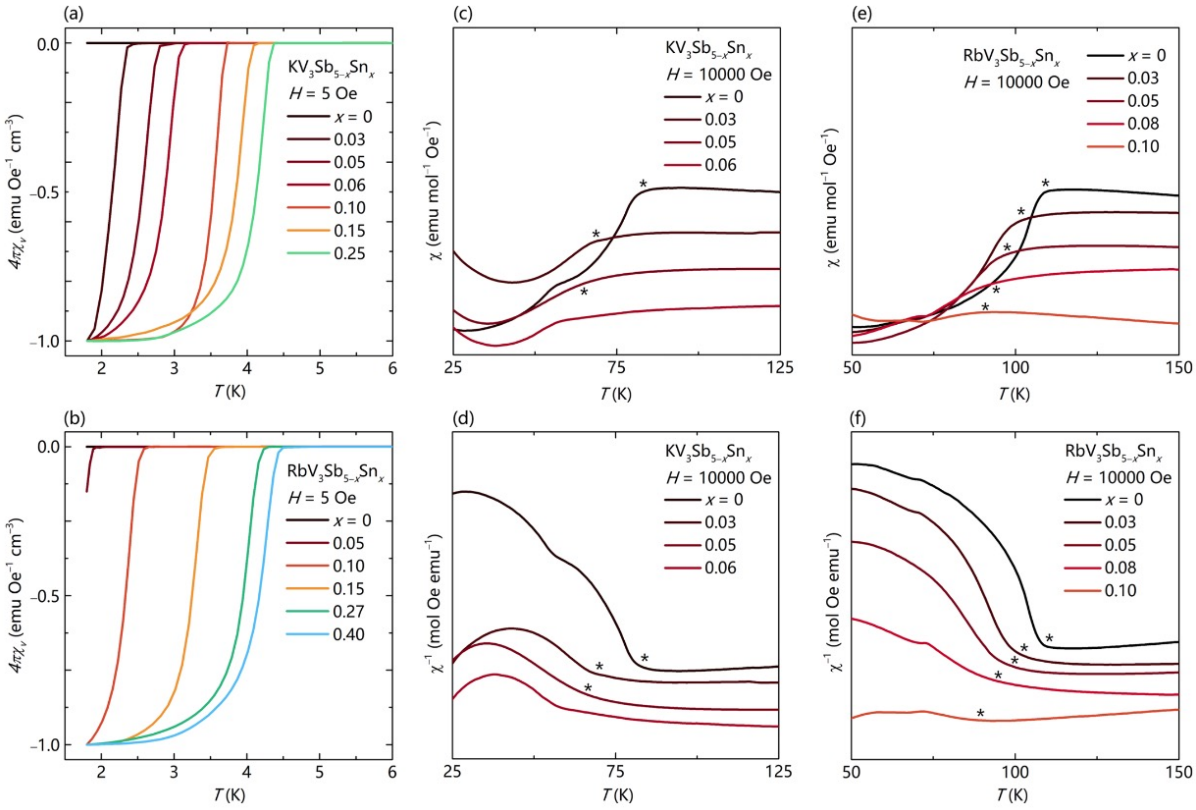

Figure 4.2: (a) The superconducting T_C of $KV_3Sb_{5-x}Sn_x$, measured under a field of $H = 5$ Oe, systematically shifts to higher temperatures in compositions up to $x = 0.30$. The superconducting fraction is normalized to account for errors in mass and packing fraction, ensuring that all data have a minimum of -1, the theoretical minimum. (b) The $1/\chi$ values for compositions $x \leq 0.05$ in $KV_3Sb_{5-x}Sn_x$ indicate that the CDW T^* decreases from 86 K to 59 K and disappears for $x \geq 0.05$. (c) The superconducting T_C of $RbV_3Sb_{5-x}Sn_x$, measured under a field of $H = 5$ Oe, systematically shifts to higher temperatures in compositions up to $x = 0.40$. (d) The $1/\chi$ values for compositions $x \leq 0.10$ in $RbV_3Sb_{5-x}Sn_x$ illustrate that the CDW T^* decreases and eventually disappears for $x \geq 0.10$. (e) The resistivity data for $KV_3Sb_{4.8}Sn_{0.2}$ and $RbV_3Sb_{4.6}Sn_{0.4}$ confirm the T_C transitions and the absence of CDW transitions for these higher Sn content samples.

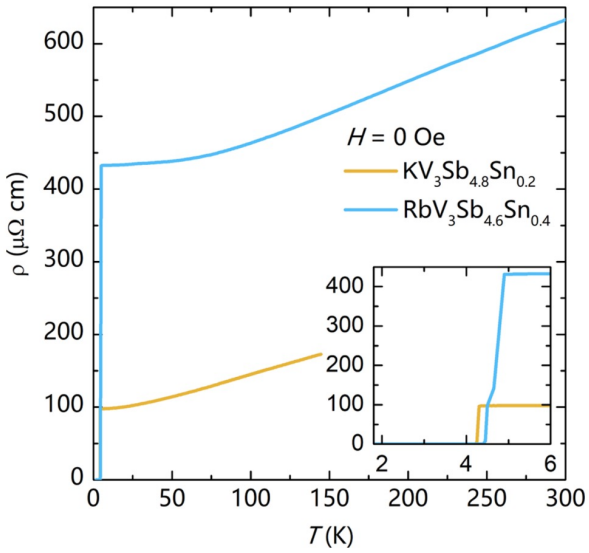

Figure 4.3: Resistivity data obtained from pressed and sintered pellets of polycrystalline $KV_3Sb_{4.8}Sn_{0.2}$ and $RbV_3Sb_{4.6}Sn_{0.4}$ confirm the T_C transitions and absence of charge density wave (CDW) transitions for these samples with higher Sn content.

The determination of the CDW T^* was based on identifying the inflection point of χ^{-1} *vs.* T. In the case of polycrystalline KV_3Sb_5 examined here, the T^* is 86 K, aligning well with the reported CDW transition temperatures of approximately 80 K in crystals [49]. Using this metric, the CDW transition is swiftly suppressed with increasing hole-doping, decreasing to 60 K at $x = 0.06$ before being entirely suppressed. Similarly, in RbV_3Sb_5, the CDW T^* employing the same metric is around 112 K, consistent with the literature-reported value [3]. The CDW is rapidly suppressed to 91 K at $x = 0.10$, at which point it completely disappears (Figure 4.2(d)). In both systems, the CDW transition is fully suppressed with much less Sn content compared to that required to reach the peak of the superconductivity dome. This observation suggests that the interplay between superconductivity and CDW differs in the case of A = K, Rb compared to CsV_3Sb_5, where the CDW persists through the peak of the first superconducting dome.

Electrical resistivity measurements of samples in the vicinity of the superconducting peak concentrations are depicted in Figure 4.3. The emergence of the superconducting states is distinctly observed as zero-resistivity conditions, with transitions occurring at 4.25 K for

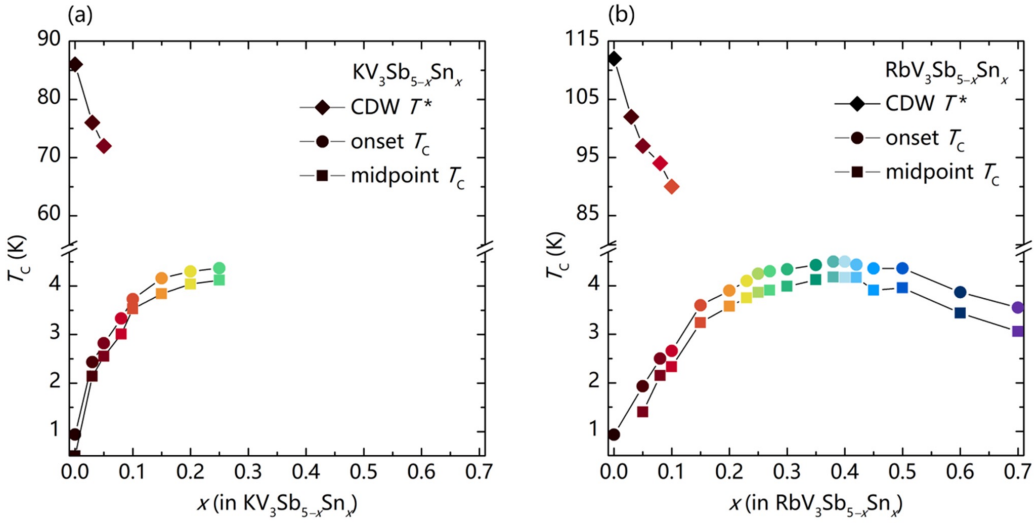

Figure 4.4: The evolution of the superconducting T_C and charge density wave (CDW) order T^* is depicted as a function of Sn composition for $KV_3Sb_{5-x}Sn_x$ and $RbV_3Sb_{5-x}Sn_x$. In $KV_3Sb_{5-x}Sn_x$, the incorporation of Sn reaches its solubility limit before a complete superconducting dome is established, yet the suppression of CDW T^* is still fully realized. On the other hand, $RbV_3Sb_{5-x}Sn_x$ exhibits a single superconducting dome before the solubility limit is reached, along with a simultaneous suppression of CDW order by $x = 0.1$.

$KV_3Sb_{4.80}Sn_{0.20}$ and 4.4 K for $RbV_3Sb_{4.60}Sn_{0.40}$, which are in agreement with those observed in the magnetization data. Additionally, there are no indications of CDW transitions. Analogous to $CsV_3Sb_{5-x}Sn_x$, the residual resistance increases in $RbV_3Sb_{5-x}Sn_x$ and $KV_3Sb_{5-x}Sn_x$ with Sn-substitution, while T_C experiences an increase.

The impacts of Sn-substitution on superconducting (SC) and charge density wave (CDW) orders in $KV_3Sb_{5-x}Sn_x$ and $RbV_3Sb_{5-x}Sn_x$ are summarized in Figure 4.4. In both systems, the temperature of CDW ordering is swiftly suppressed with minor levels of hole doping and completely vanishes before reaching the peak superconducting transition temperatures. Apart from the Sn solubility limit within each lattice, the two phase diagrams exhibit qualitatively similar behavior.

Due to size constraints, the Sn solubility limits in KV_3Sb_5 and RbV_3Sb_5 are significantly lower compared to CsV_3Sb_5. Nevertheless, in all of these systems, the alterations in the electronic structure for the relevant compositions can be deduced by computing band structures upon

substituting one Sb atom for an Sn atom within and outside the kagome plane. Figure 4.5(a) and (d) demonstrate the band structure of undoped KV_3Sb_5 and RbV_3Sb_5, respectively, indicating the range of achievable Fermi levels with the loss of one electron per unit cell shown in gray. Figure 4.5(b) and (e) illustrate a hypothetical structure where the Sb1 lattice is fully replaced by Sn. The shifts in the band structure resemble those observed in CsV_3Sb_4Sn, with the Γ pocket and M-point van Hove singularities (vHs) elevated above the Fermi level. Band structures for Sn substitution within the Sb2 sublattice are depicted in Figure 4.5(c) and (f) and exhibit significant reconstructions at multiple points, including K, L, and H.

4.4 Discussion

Given the close structural and electronic properties across the AV_3Sb_5 series, the disparity in the hole-doping phase diagrams of KV_3Sb_5 and RbV_3Sb_5 compared to CsV_3Sb_5 is intriguing. While the alterations in the band structure resulting from Sn substitution on the Sb1 sublattice in KV_3Sb_4Sn and RbV_3Sb_4Sn initially seem similar to those in CsV_3Sb_4Sn, subtle distinctions are nonetheless present, potentially leading to distinct electronic phase diagrams. A closer examination of the saddle points around M reveals that the irreducible representations of the two points differ for A = K, Rb, and Cs [82, 102]. As a consequence of the saddle point inversions, bands intersect near E_F in CsV_3Sb_5 but not in KV_3Sb_5. This distinction may influence the nature of the stabilized CDW states, the proximity of which may uniquely modify superconductivity. Understanding the nuanced variations in the electronic structure arising from the substitution of Sn is crucial, especially considering the potential impact on the interplay between CDW and superconductivity. These findings emphasize the significance of small compositional changes and their intricate effects on the electronic and magnetic properties in this class of materials, thereby warranting further detailed investigations and theoretical explorations.

One unifying theme among doping and pressure investigations of AV_3Sb_5 materials is the

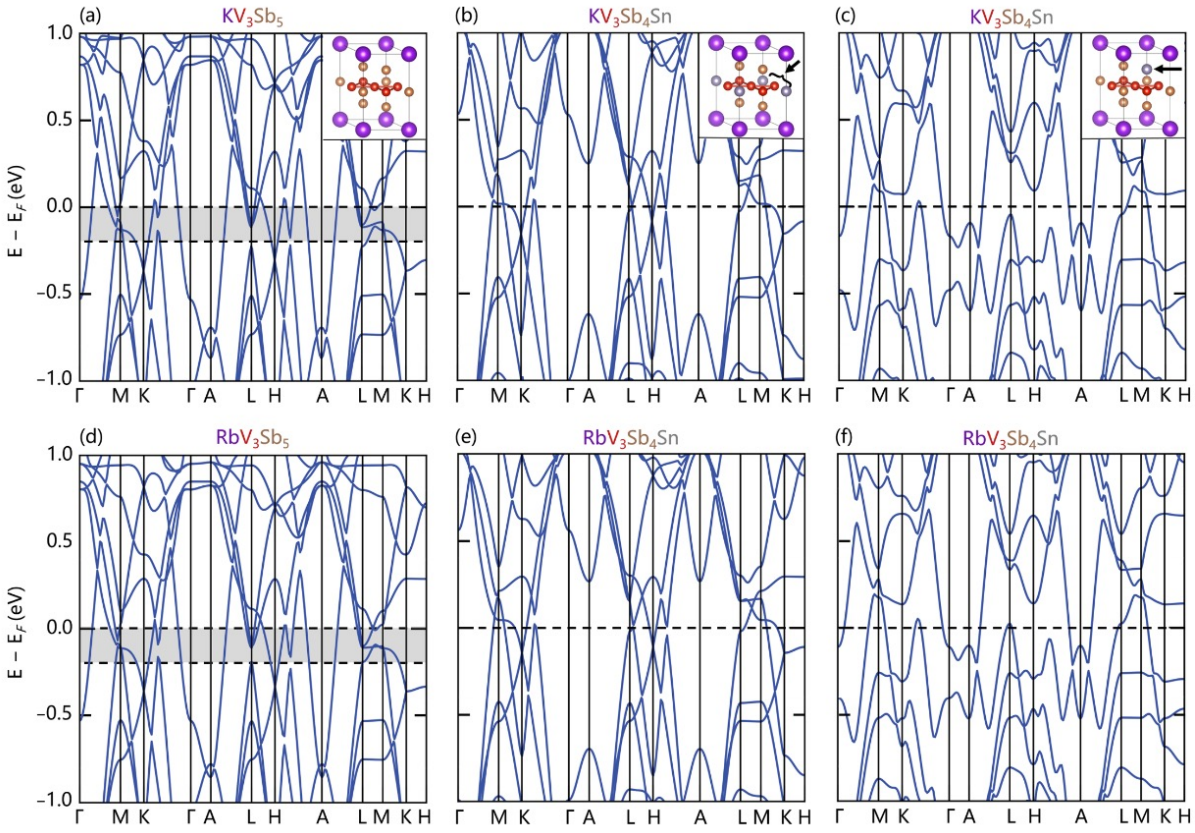

Figure 4.5: (a,d) DFT calculations for KV_3Sb_5 and RbV_3Sb_5 highlighting the allowable range of Fermi levels under the rigid band approximation for the substitution of one Sn atom per formula unit (resulting in one electron less Fermi energy). (b,e) Calculation for a hypothetical structure where one Sn has been substituted within the kagome plane (Sb1 sublattice). The majority of the electronic structure is preserved as in KV_3Sb_5 and RbV_3Sb_5, except for the Γ pocket and the van Hove singularities at the M point, which have shifted significantly upward, potentially contributing to the observed changes in properties. (c,f) Calculation for a hypothetical structure where one Sn has been substituted outside the kagome plane (Sb2 sublattice). A notable restructuring of several bands is evident, particularly near K, H, and the K-Γ points.

presence of two distinct superconducting domes, a unique feature observed solely in CsV_3Sb_5. If one considers pressure or doping as perturbations that simply destabilize the charge density wave (CDW) order, the data strongly suggest that CsV_3Sb_5 harbors a CDW state distinct from the other two variants. In this context, the phase diagram of CsV_3Sb_5 implies a transition between CDW states that is seemingly absent in KV_3Sb_5 and RbV_3Sb_5.

While the intermediate states differ between pressure-induced and hole-doping studies, investigations into the native CDW order in AV_3Sb_5 have revealed distinctions between A = Cs and A = Rb/K. The out-of-plane modulation in Cs is four times that of K [49, 50], and the in-plane structure of the CDW state in CsV_3Sb_5 encompasses both star-of-David and tri-hexagonal characteristics [50, 93, 106], a pattern seemingly absent in the other variants. Considering these differences, one plausible scenario involves a doping-induced transition from an (L, L, L)-type order to an (M, L, L)-type of order upon doping CsV_3Sb_5 [107], a transition that is not observed in the other two compounds. Future scattering studies across the carrier-tuned phase diagrams of these systems will be necessary to fully explore any potential crossovers.

4.5 Conclusion

The phase diagrams resulting from Sn-substitution or hole-doping in KV_3Sb_5 and RbV_3Sb_5 were thoroughly investigated. Notably, the solubility of Sn within the AV_3Sb_5 lattice displays variability linked to the size of the A-site cation, with A = K exhibiting the most restricted solubility and A = Cs accommodating the highest degree of substitution. Prior to reaching the solubility limit, the process of hole-doping, achieved by substituting Sn on Sb sites in both KV_3Sb_5 and RbV_3Sb_5, reveals phase diagrams exhibiting similar characteristics, including a single superconducting (SC) dome and a rapid suppression of charge density wave (CDW) order. These findings stand in contrast to the recently reported double dome observed in CsV_3Sb_5, which suggests the existence of a distinct parent CDW state for the latter. The results

of this comprehensive study have been published. For a more in-depth understanding and supplementary information, we encourage readers to refer to the associated research paper[95].

4.6 Acknowledgments

This work was supported by the National Science Foundation (NSF) through Enabling Quantum Leap: Convergent Accelerated Discovery Foundries for Quantum Materials Science, Engineering and Information (Q-AMASE-i): Quantum Foundry at UC Santa Barbara (DMR-1906325). The research reported here made use of shared facilities of the NSF Materials Research Science and Engineering Center at UC Santa Barbara DMR-1720256, a member of the Materials Research Facilities Network (www.mrfn.org). Use of the Advanced Photon Source at Argonne National Laboratory was supported by the U.S. Department of Energy, Office of Science, Office of Basic Energy Sciences, under Contract No. DE-AC02-06CH11357. YMO is supported by the National Science Foundation Graduate Research Fellowship Program under Grant No. DGE-1650114. FK acknowledges the Roy T. Eddleman Center for Quantum Innovation (ECQI) for their support.

Chapter 5

YbV_3Sb_4 and EuV_3Sb_4, vanadium-based kagome metals

[1]In our study, we introduce two intriguing compounds, YbV_3Sb_4 and EuV_3Sb_4, which unveil novel possibilities within the realm of vanadium-based kagome metals. These compounds feature vanadium-based kagome networks that exhibit slight distortions, accompanied by zig-zag chains of divalent Yb^{2+} and Eu^{2+} ions. Our work includes details on methods employed for growing single crystals, as well as an extensive analysis involving, computational calculations, electronic, and thermodynamic measurements.

First, we turn our attention to YbV_3Sb_4, a nonmagnetic metal characterized by its intriguing properties. Across the temperature range of 60 mK to 300 K, no collective phase transitions are observed. The absence of magnetism and the stability within this temperature span make YbV_3Sb_4 a captivating subject of study in the family of vanadium-based kagome metals.

In contrast, our exploration of EuV_3Sb_4 reveals an entirely different facet of this family. EuV_3Sb_4 emerges as a magnetic kagome metal, marked by its distinctive behavior. Below a

[1]The contents of this chapter previously appeared in Ref. [108]: B.R. Ortiz, G. Pokharel, M. Gundayao, H. Li, **F. Kaboudvand**, L. Kautzsch, S. Sarker et al. "YbV_3Sb_4 and EuV_3Sb_4, Vanadium-Based Kagome Metals with Yb^{2+} and Eu^{2+} Zig-Zag Chains", *Phys. Rev. Mater.* **7** (2023) 064201. Reprinted with permission.

critical temperature of $T_C = 32$ K, it exhibits an easy-plane ferromagnetic-like order. Notably, under the influence of low magnetic fields, it displays signs of noncollinearity, introducing intriguing complexities to its magnetic behavior.

Our discovery of YbV_3Sb_4 and EuV_3Sb_4 demonstrates a fresh and promising direction for the exploration and development of vanadium-based kagome metals. These compounds exemplify the exciting possibilities offered by integrating the chemical and magnetic degrees of freedom inherent in a rare-earth sublattice.

5.1 Introduction

Research in the realm of layered kagome metals has seen remarkable acceleration in recent years, driven in part by the breakthrough discovery of the AV_3Sb_5 kagome superconductors [3, 109, 110, 111]. This heightened interest has been further stoked by the continued exploration of the AM_6X_6 phase space [10, 112, 113, 113, 114, 115, 116, 117, 118, 119, 120, 121, 122]. Kagome network-based metals have garnered significant attention due to their potential to exhibit a rich electronic structure characterized by Dirac points, flat bands, and Van Hove singularities [46, 71, 123, 124]. Depending on the alignment of the Fermi level with these features, a diverse range of electronic instabilities can emerge, encompassing phenomena such as bond density wave order [123, 125], charge fractionalization [126, 127], charge-density waves [8, 71, 128], and superconductivity [19, 71, 123]. Developing new compounds constructed on kagome networks with variable band fillings and the ability to engineer additional interactions, such as magnetic order, continues to be an ongoing challenge.

The nonmagnetic kagome network comprising vanadium ions, located near the Van Hove points within the AV_3Sb_5 (A: K, Rb, Cs) class of kagome superconductors, offers a unique amalgamation of charge density wave (CDW) order and a superconducting ground state [49, 50, 74, 93, 106, 109, 110, 111]. This distinctive behavior makes them excellent platforms for

delving into electronic interactions within the kagome lattice. The challenge at hand is to introduce magnetic interstitial ions into the nonmagnetic vanadium kagome network, akin to the approach used in $Ln V_6Sn_6$ compounds which discussed in chapter 6. This challenge is driven by the exciting potential to engineer magnetic order within itinerant kagome metals, thereby stabilizing a fascinating range of magnetic and electronic instabilities. These include tunable Chern gaps [10, 115, 121, 122], anomalous Hall effects [113, 129, 130], and spin-charge coupled density waves [131].

One exciting class of materials that merits attention consists of compounds in the form of AM_3X_4. These materials feature M-based kagome sublattices combined with zig-zag chains of A-site ions. The choice of A-site offers a degree of chemical flexibility akin to the AM_6X_6 family. Currently, known structures within the AM_3X_4 family are almost exclusively represented by ATi_3Bi_4 with A^{3+} ions, such as La^{3+}, Ce^{3+}, and Sm^{3+} [132, 133]. An exceptional case to this pattern is CaV_3Sb_4, where the Ti–Bi sublattice is replaced with V–Sb. This substitution mirrors the reverse situation of the AV_3Sb_5 family, in which the Ti–Bi variants $RbTi_3Bi_5$ [134] and $CsTi_3Bi_5$ [105, 134] emerged after the initial discovery of the V–Sb series [3]. The overall structure appears to tolerate various A-site valences, as both trivalent rare-earth and divalent alkali-earth compounds (e.g., $CaTi_3Bi_4$, CaV_3Sb_4) are known. However, up to this point, CaV_3Sb_4 remains the sole known V–Sb AM_3X_4 [133]. It's worth noting that other non-stoichiometric antimonides like $NdTi_3(Sb_{0.9}Sn_{0.1})_4$ are recognized [135], and while they may not exist at the purely antimonide limit, they suggest a level of chemical tunability within AM_3X_4 metals. Nevertheless, our knowledge of the physical properties of these materials remains limited.

In this chapter, we present the characterization of two new AM_3X_4 kagome metals: YbV_3Sb_4 and EuV_3Sb_4. Much like the case of CaV_3Sb_4, both YbV_3Sb_4 and EuV_3Sb_4 feature divalent Yb^{2+} and Eu^{2+} ions as A-site cations. Analogous to the AV_3Sb_5 and $Ln V_6Sn_6$ compounds, the vanadium sublattice appears nonmagnetic, with magnetism being primarily attributed to the

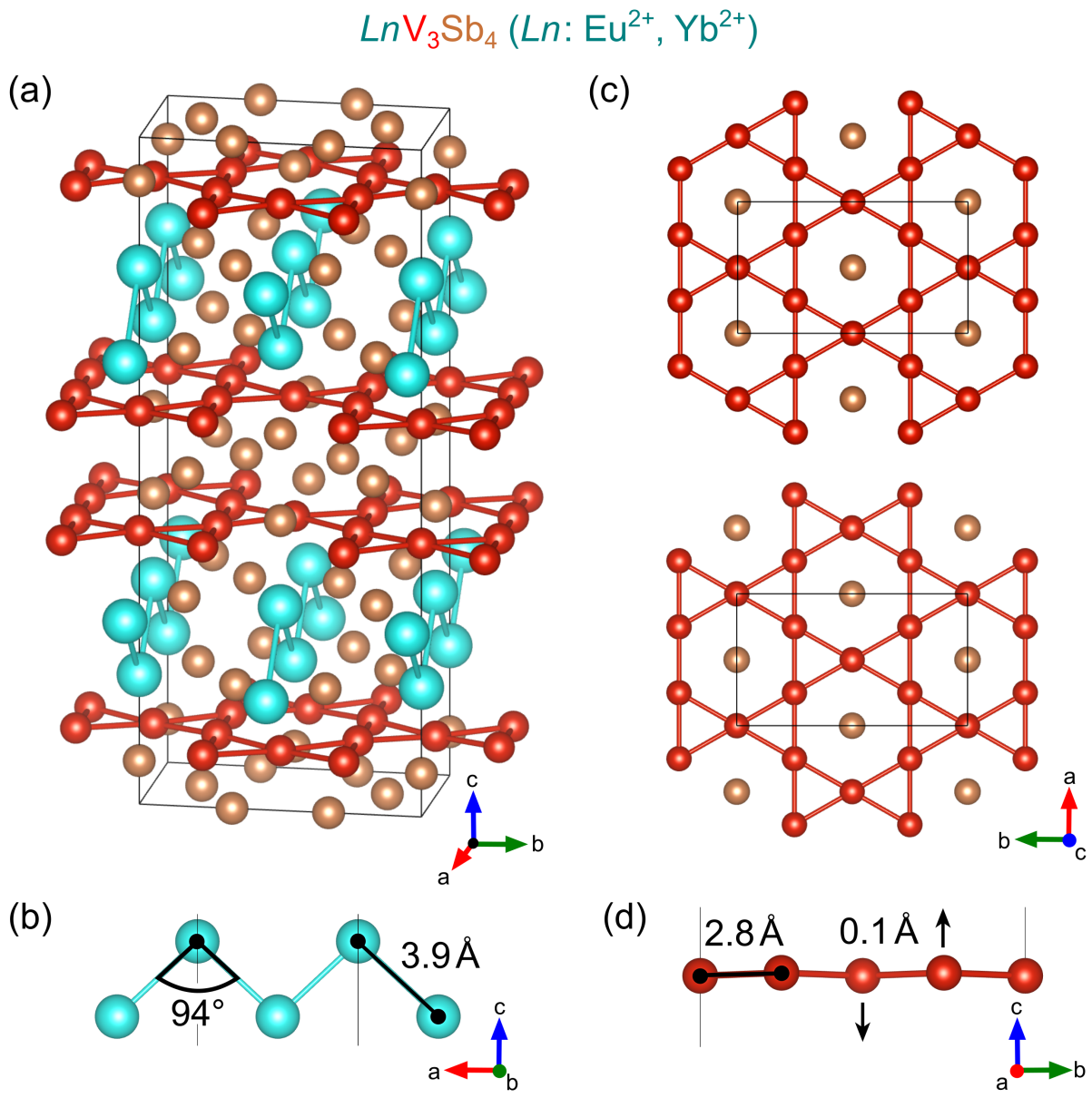

Figure 5.1: YbV_3Sb_4 and EuV_3Sb_4 are both characterized by an orthorhombic crystal structure (space group *Fmmm*). These compounds feature a unique arrangement, where (a) a zig-zag sublattice of *Ln* ions (lanthanides, in this case, Yb and Eu) is intricately woven into the structure. This sublattice is further complemented by (b) staggered layers of V-based kagome networks, which contribute to the overall complexity of the crystal lattice. In line with their orthorhombic symmetry, the kagome networks exhibit (c) slight distortions. These distortions, although present, are relatively minor, with all V-atoms deviating from the idealized kagome lattice by less than 0.1 Å. These subtle structural variations contribute to the unique electronic properties of these materials. To provide a visual reference, some key interatomic distances of interest within this crystal structure are highlighted in the accompanying graphic.

rare-earth element. As expected for Yb^{2+}, YbV_3Sb_4 crystals exhibit Pauli paramagnetism with no apparent thermodynamic phase transitions between 60 mK and 300 K. In contrast, EuV_3Sb_4 displays a low-field ferromagnetic transition at a critical temperature of around 32 K. The magnetism in EuV_3Sb_4 presents an easy-plane anisotropy, and the susceptibility along the *c*-axis suggests a more intricate magnetic ground state in the absence of an external magnetic field, possibly involving moment canting or helical states. Curie-Weiss and magnetic heat capacity analyses are consistent with the magnetism originating from the full moment of $S = 7/2$ Eu^{2+} ions. Together, our results further expand our understanding of kagome metals, offering new avenues for exploring intricate electronic and magnetic ground states in kagome-based materials.

5.2 Methods

5.2.1 Computational Modeling

Since no previous electronic structure calculations have been reported, we undertook the task of providing fundamental insights into the electronic structure of the nonmagnetic AM_3X_4 lattice. To achieve this, first-principles calculations based on density functional theory (DFT) within the Vienna ab initio Simulation Package (VASP) were performed [83, 84]. We employed the projector augmented wave (PAW) method [38, 85] and conducted ionic position relaxations using an energy cutoff of 520 eV. In the reciprocal space, *k*-point meshes were automatically generated with a density of 40 $Å^{-1}$ along each reciprocal lattice vector. The band structure was calculated over a selected set of high symmetry points, as defined by Setyawan and Curtarolo [86].

5.2.2 Synthesis and X-ray Diffraction

YbV_3Sb_4 single crystals are grown in an argon-filled glove box with controlled oxygen and water levels ($<$1 ppm) via a self-flux method. A stoichiometric mixture of Yb, V, and Sb (in a 1:3:4 ratio) is ball-milled in sealed vials. The milling process includes three 1 hr segments with intermediate grinding steps to dislodge Yb metal agglomerates. The resulting precursor can be annealed at 650°C to produce polycrystalline YbV_3Sb_4 powders. For single crystal growth, the as-milled precursor is loaded into high-density alumina crucibles, sealed in carbon-coated fused silica ampules under argon, and heated to 1050°C before slowly cooling to 800°C. Crystals are thin (100–500 μm) hexagonal flakes with side lengths approximately 1–2 mm. The samples are a lustrous silver and can be exfoliated with some slight difficulty. YbV_3Sb_4 does not congruently melt but undergoes peritectic decomposition above 1050°C, with the resulting liquid phase acting as the flux. Efforts to grow YbV_3Sb_4 using alternative fluxes have not succeeded.

Single crystals of EuV_3Sb_5 are grown using a bismuth flux method. A stoichiometric mixture of Eu, V, Sb, and Bi (in a 1:3:4:40 ratio) is sealed in fused silica ampules under argon, heated to 1000°C, and slowly cooled to 400°C, followed by centrifugation to remove excess bismuth. The resulting crystals are typically thin hexagonal flakes (10-50μm) with a brilliant silver luster. The crystal structure of YbV_3Sb_4 was determined using powder diffraction data collected at the Advanced Photon Source [136, 137, 138].

Single-crystal measurements for both YbV_3Sb_4 and EuV_3Sb_4 were conducted on a Bruker KAPPA APEX II diffractometer with a Mo Kα X-ray source (λ = 0.71073 Å) and a TRIUMPH monochromator. Synchrotron X-ray diffraction experiments were carried out at the QM2 beam line at CHESS, using an incident X-ray wavelength of λ = 0.41328 Å. The diffraction experiment employed a cryostream for temperature control and a 6-megapixel pixel-array detector. Data collection involved full 360° rotations with a 0.1° step size. Scattering planes in reciprocal space were visualized using NeXpy software, and data analysis, including absorption and extinction

corrections, was performed using the APEX3 software package. Crystallographic structural solutions were determined using the SHELX software package [139].

Scanning tunneling microscopy (STM) measurements were conducted using a custom Unisoku USM1300 microscope. YbV_3Sb_4 single crystals were cleaved at 20 K and promptly placed into the 4.5 K STM head. Spectroscopic measurements were performed with a standard lock-in technique (frequency: 910 Hz, bias excitation) as explained in the figure captions. STM tips consisted of in-house chemically-etched tungsten tips, annealed to a bright orange color in a UHV chamber before use. To align the atomic Bragg peaks onto single pixels, we employed the Lawler-Fujita drift-correction algorithm to process our data.

Details can be found in the supplementary information of the paper[108].

5.2.3 Bulk Characterization

Magnetization measurements for both YbV_3Sb_4 and EuV_3Sb_4 single crystals were conducted using a Quantum Design Dynacool PPMS system, with single crystals mounted on the sample stage. Heat capacity measurements for both compounds in the range of 1.8K to 300K were performed using a 9T Dynacool PPMS system equipped with the heat capacity option. Additional measurements for YbV_3Sb_4 were taken with a 14T Dynacool PPMS system featuring the dilution refrigerator option. Data normalization was achieved by scaling to higher temperature YbV_3Sb_4 data within the 2K to 4K range.

5.3 Results and discussion

YbV_3Sb_4 and EuV_3Sb_4 represent novel additions to the relatively small AM_3X_4 compound class. Previously, this family predominantly featured Ti–Bi networks paired with rare-earth ions [132, 133, 140]. Notably, YbV_3Sb_4 and EuV_3Sb_4 diverge from this pattern by incorporating divalent rare-earth A-site ions, specifically Yb^{2+} and Eu^{2+}. The overall crystal structure of

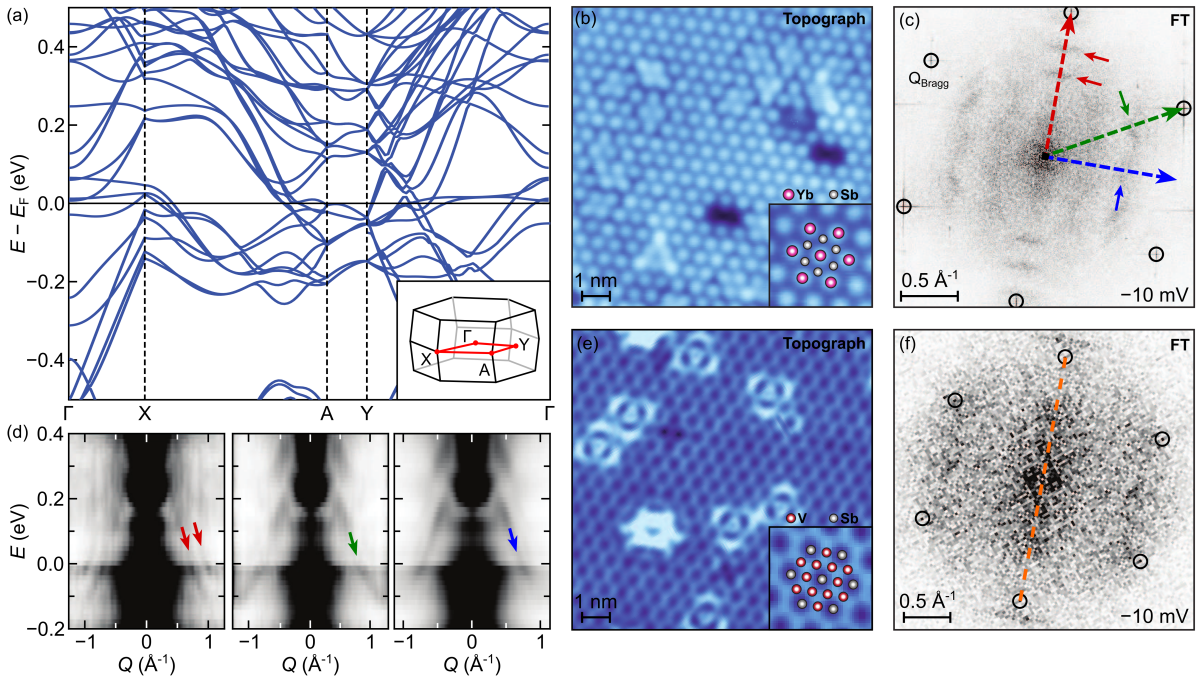

Figure 5.2: (a) Electronic structure of *Fmmm* YbV_3Sb_4 calculated over a selected portion of high-symmetry points, displaying Dirac-like and flatband-like features consistent with the vanadium kagome network. Most cleavage surfaces feature Yb–Sb termination, leading to the scanning tunneling microscopy (STM) topograph and quasiparticle interference (QPI) patterns shown in (b) and (c). We provide several energy- and momentum-dependent line cuts through the QPI patterns (red, green, blue) in (d), with bands indicated by colored arrows. Occasionally, crystals cleave along the V–Sb layers, leading to the STM topograph in (e) and the corresponding QPI in (f).

YbV_3Sb_4 and EuV_3Sb_4 is presented in Figure 5.1(a). The schematic highlights the V and *Ln* sublattices, with V–Sb and *Ln*–Sb bonds excluded for clarity.

Figure 5.1(b) illustrates the zig-zag chains formed by *Ln*–*Ln* distances, which are more closely spaced along the chain (∼3.9 Å) than between neighboring chains (∼5.6 Å). In contrast to the simpler AM_3X_5 (*P6/mmm*) and AM_6X_6 (*P6/mmm*) compounds, AM_3X_4 (*Fmmm*) compounds contain four kagome layers within each unit cell.

Figure 5.1(c) emphasizes these distinct layers, which are mutually displaced. Although the nearest-neighbor Sb atoms are shown, they are not technically part of the kagome plane. This feature mirrors the situation in the AM_6X_6 ($HfFe_6Ge_6$) prototype, where the *X* atoms are slightly

offset above/below the kagome sheet. Additionally, the AM_3X_4 structure encompasses elements of the AM_6X_6 motif when stacked along the c-axis. The stacking sequence in AM_3X_4 includes layers of X_4–M_3–AX_2–[AX_2–M_3–X_4–M_3–AX_2]–AX_2–AX_2–M_3–X_4. The bracketed segment resembles the stacking of the AM_6X_6 prototype structure, as seen in $HfFe_6Ge_6$. It is noteworthy that the other layers in AM_3X_4 compounds incorporate stacking elements from various kagome and quasi-2D compounds, such as $CeCo_3B_2$, $Cs_2Pt_3S_4$, Zr_4Al_3, and $CrSi_2$ [133].

Similar to other AM_3X_4 compounds, the kagome layers within YbV_3Sb_4 and EuV_3Sb_4 display slight distortions, as depicted in Figure 5.1(d). These distortions manifest as mild buckling of the planes and non-uniform V–V distances. Nevertheless, these deviations are relatively minor, with vanadium atoms straying no more than 0.1 Å from their idealized kagome positions. Corresponding CIF files can be accessed in the Electronic Supplementary Information (ESI) of the published paper[108].

The structural imperfections in these compounds do not obscure the manifestation of various key kagome lattice features within their electronic structures. Figure 5.2(a), offers a concise representation of the electronic structure near the Fermi level. An inset displaying a subset of high-symmetry points within the orthorhombic Brillouin zone is presented in the bottom right. The more intricate structure results in a significantly richer band diagram near the Fermi level compared to the AM_3X_5 and AM_6X_6 phases. Nonetheless, Dirac-like characteristics at S and flatband-like features from Y–Γ are observed within 50 to 100 meV of the Fermi energy. These features offer exciting prospects for future studies utilizing ARPES or scanning tunneling spectroscopy techniques.

STM measurements were conducted to investigate any short-range charge correlations in YbV_3Sb_4 crystals not captured in the average structure. The crystals cleave in a way that exposes both Yb–Sb and V–Sb terminations. Figure 5.2(b) illustrates an STM topograph of a Yb–Sb cleavage plane. The STM-measured lattice parameters (a=5.70 Å and b=9.87 Å) are in good agreement with those refined from diffraction (a=5.62 Å and b=9.82 Å). The associated

Fourier transform and quasiparticle interference (QPI) patterns are presented in Figure 5.2(b) and (c), with atomic Bragg peaks highlighted by black circles. The two-fold symmetry of the QPI is consistent with the orthorhombic nature of YbV_3Sb_4. Energy/momentum line cuts are highlighted in red, green, and blue in Figure 5.2(c) and correspond to the energy- and momentum-dependent QPI linecuts in Figure 5.2(d), where bands are indicated by colored arrows.

Less frequently, the V–Sb termination is also observed via STM. Figure 5.2(e) presents the corresponding topograph, while Figure 5.2(f) shows the QPI for the vanadium-terminated surface. Atomic Bragg peaks are outlined with black circles, and the two-fold axis is highlighted in orange. An energy/momentum line cut through Figure 5.2(f) and more information are available in the ESI of the paper [108]. Given the relatively complex electronic structure, more detailed calculations will be necessary to directly compare the bands extracted from the STM QPI linecuts with our DFT calculations.

5.3.1 YbV_3Sb_4

The bulk electronic properties of YbV_3Sb_4 single crystals were investigated. Figure 5.3(a) illustrates temperature-, field-, and orientation-dependent magnetization data, revealing the compound's characteristic Pauli paramagnetic nature with an extremely weak susceptibility (10^{-6} emu Oe^{-1} mol^{-1}) and the absence of bulk local moments. No substantial qualitative difference was observed when the crystal was mounted with the *c*-axis either parallel or perpendicular to the magnetic field. Similarly, the isothermal magnetization on single crystals (Figure 5.3(a, inset)) demonstrated no saturation, aligning with a magnitude of 10^{-2} μ_B per Yb under 7 T, consistent with impurity spin polarization.

Figure 5.3(b) presents temperature-dependent resistivity data, indicating metallic transport behavior in YbV_3Sb_4. The residual resistivity was approximately 11 μΩ cm, although the

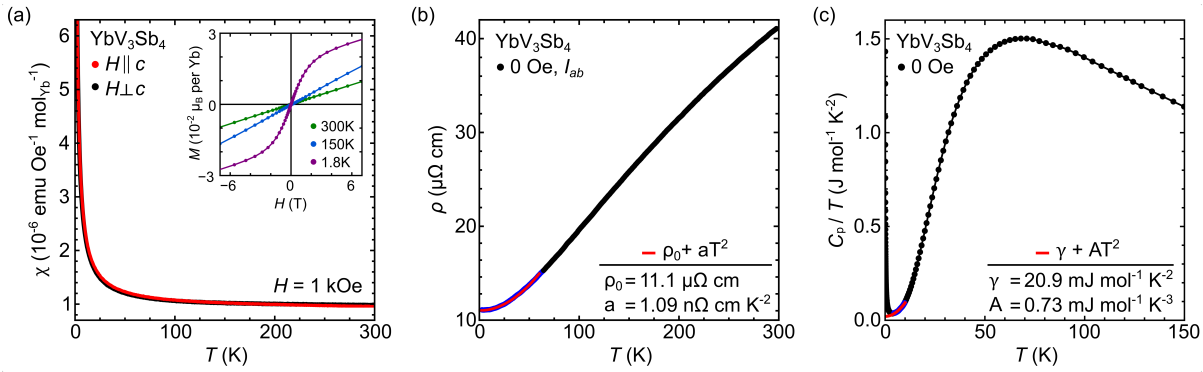

Figure 5.3: Bulk electronic properties of single crystals of YbV_3Sb4 were characterized. Temperature-dependent magnetization data are depicted in Figure (a) with both orientations (c parallel and perpendicular to H), indicating predominantly temperature-independent Pauli paramagnetism along with a weak Curie tail arising from impurity spins. The isothermal magnetization plot (inset of (a)) does not display clear saturation, and the observed magnitude (10^{-2} μ_B per Yb) is consistent with a small fraction of impurity spins. Zero-field resistivity measurements shown in (b) confirm the metallic nature of YbV_3Sb_4 crystals, with a simple quadratic fit applied to the low-temperature data. Heat capacity results are displayed in (c), indicating a nuclear Schottky anomaly below 0.1 K. A Sommerfeld fit (red) is superimposed over a limited temperature range (blue) excluding the Schottky anomaly.

residual resistivity ratio (RRR) was relatively low ($\sim$4). Consequently, no quantum oscillation signatures were observed in the magnetoresistance when the magnetic field was applied parallel to the c-axis with the current within the ab-plane. The zero-field, low temperature (< 50 K) resistivity was well-modeled using Fermi liquid behavior and a simple quadratic fit $\rho = \rho_0 + aT^2$ with ρ_0 = 11.1 μΩ cm and $a = 1.09$ nΩ cm K^{-2}.

No clear phase transitions were indicated in the magnetization or resistivity results on YbV_3Sb_4 down to 2 K. Zero-field heat capacity measurements were also collected from 300 K down to 60 mK. Figure 5.3(c) illustrates the resulting C_p/T data for a 1.1 mg single crystal. A feature consistent with a nuclear Schottky anomaly emerged around 0.1 K, with another small feature noted at 0.8 K. The magnitude of the 0.8 K feature suggests that this is due to an impurity effect, such as freezing of the paramagnetic impurities resolved in magnetization measurements. To avoid contributions from the nuclear Schottky anomaly, a Sommerfeld model was fit to a

limited temperature range (4 K to 10 K). The resulting least-squares fit yielded the parameters $\gamma = 20.9$ mJ mol^{-1} K^{-1} and $A = 0.73$ mJ mol^{-1} K^{-3}.

All experimental data characterizing YbV_3Sb_4 support the classification as a nonmagnetic kagome metal. The structure is consistent with a Yb^{2+} rare-earth sublattice, and no bulk magnetic, electronic, or structural instabilities were noted from 60 mK to 300 K. These results resemble those in other nonmagnetic AM_3X_4 compounds CaV_3Sb_4 and $CaTi_3Bi_4$ [133]. Therefore, YbV_3Sb_4 serves as an excellent comparison and nonmagnetic standard for EuV_3Sb_4.

5.3.2 EuV_3Sb_4

Whereas Yb^{2+} results in a nonmagnetic rare-earth sublattice, divalent Eu^{2+} is isoelectronic to Gd^{3+} ($S = 7/2$) and is expected to exhibit a magnetically ordered ground state. Figure 5.4 illustrates the temperature-, field-, and orientation-dependent magnetization data from a 10 μ g single crystal of EuV_3Sb_4. First, focusing on the temperature-dependent susceptibility, Figure 5.4(a,b) presents the low-field susceptibility of EuV_3Sb_4 under an applied field of 100 Oe oriented with $H \| c$ and $H \perp c$, respectively.

Both orientations exhibit a notable increase in magnetization near 36 K. With $H \perp c$, a rapid polarization is observed that quickly saturates, suggesting a primarily ferromagnetic transition. Upon changing the field orientation to $H \| c$, two main differences emerge: (1) the susceptibility magnitude dramatically reduces, indicating an easy-plane anisotropy, and (2) a low-field, sharp cusp appears near T_C before continuing toward saturation. Similar low-field cusps have been observed in other magnetic kagome metals like GdV_6Sn_6, suggesting a noncollinear, modulated magnetic ground state [114].

Figure 5.4(c,d) presents the field-dependent and temperature-dependent magnetization for both field orientations illustrated in Figure 5.4(a,b). The low-field cusp in the magnetization for $H \| c$ persists for fields up to approximately 500 Oe. The isothermal magnetization (Figure

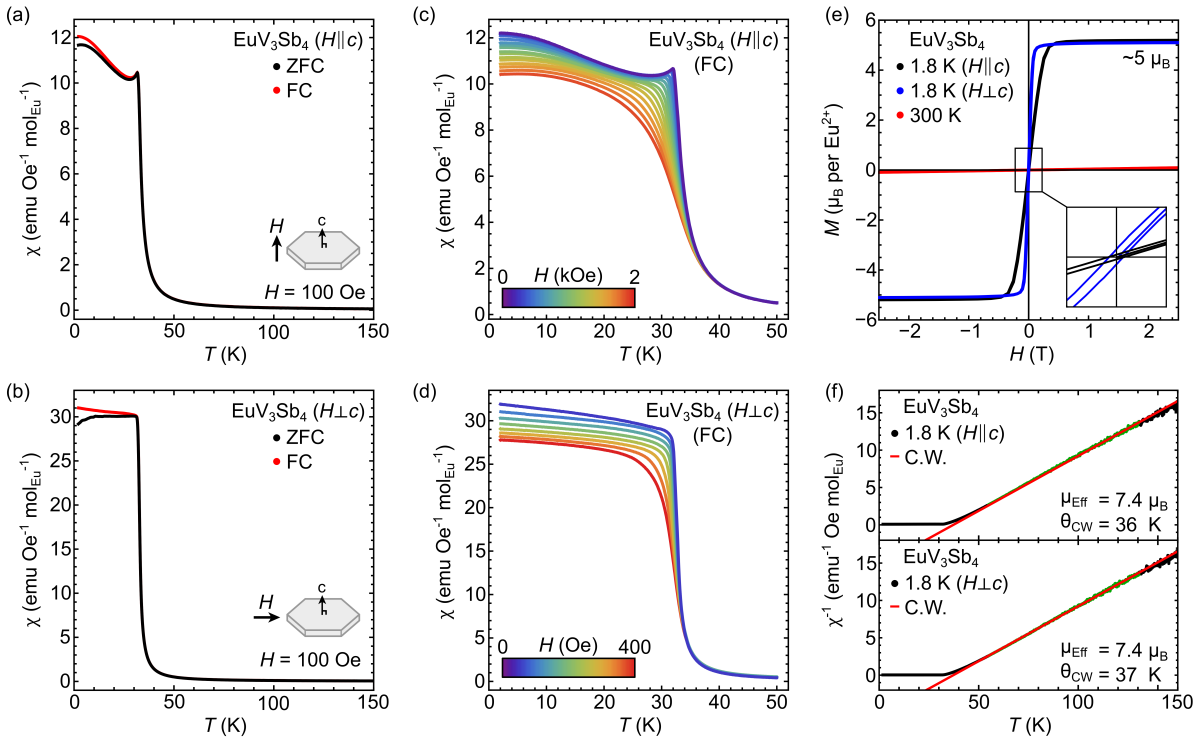

Figure 5.4: We present magnetization data from EuV_3Sb_4 single crystals, demonstrating a sharp upturn in temperature-dependent susceptibility with $H\|c$ (a) and $H\perp c$ (b) orientations near $T_C = 32$ K. An additional cusp and brief downturn in susceptibility are observed with $H\|c$. Field-cooled measurements for both orientations are shown in (c) and (d), and isothermal ZFC magnetization data are depicted in (e), highlighting rapid moment saturation and weak coercivity (inset). Curie-Weiss analysis of the low-field susceptibility for both field orientations is presented in (f).

5.4(e)) indicates that the magnetic response of $H \perp c$ saturates much faster ($\sim$500 Oe) than $H \| c$ ($\sim$2500 Oe), confirming an easy-plane anisotropy. Figure 5.4(e,inset) highlights subtle hysteresis in the 1.8 K isothermal magnetization, consistent with the FC/ZFC irreversibility plotted in Figure 5.4(a,b). Interestingly, at high fields, both curves saturate near 5 μ B, significantly below the anticipated value of 7 μ B for Eu^{2+}, assuming $S = 7/2$ and $g = 2$. Notably, Figure 5.4(f) demonstrates an abbreviated field range with no observed metamagnetic transitions up to 7 T.

A Curie-Weiss analysis (Figure 5.4(f)) of the low-field susceptibility in both field orientations yields nearly identical outcomes. Both orientations exhibit θ CW of approximately +36 K, consistent with the heat capacity peak (32 K, discussed later) and the first derivative of the magnetization curve (33 K). This analysis supports predominantly ferromagnetic correlations and minimal frustration (considering the *Ln*-sublattice's zig-zag motif independent of the vanadium kagome lattice). The effective paramagnetic moment is 7.4 μ B, close to the expected value for Eu^{2+} (7.9 μ B).

Notably, all results in Figure 5.4 were obtained from the same crystal. The local moment derived from the Curie-Weiss analysis possibly deviates from the full Eu^{2+} moment due to uncertainties in determining the sample mass. Despite accounting for a 13% mass error, an additional $\approx$1 μ B moment remains unaccounted for, suggesting potential polarization on the vanadium sites or dynamic effects. Further measurements on larger crystals are needed to confirm this.

Figure 5.5(a) displays the heat capacity data for EuV_3Sb_4 with YbV_3Sb_4 as a nonmagnetic phonon reference. A distinct anomaly is observed at $T_C = 32$ K, in good agreement with the magnetization results. The field-dependence of the heat capacity anomaly in EuV_3Sb_5 when $H \| c$ reveals broadening and slight depression with increasing fields.

Figure 5.5(b) displays the C_p/T data for YbV_3Sb_4 and EuV_3Sb_4. Subtracting the non-magnetic YbV_3Sb_4 lattice reference isolates the magnetic entropy from the EuV_3Sb_4 heat capacity data. Integration of $C_{p,mag}$ from 1.8 K to 100 K (Figure 5.5(c)) yields an entropy of

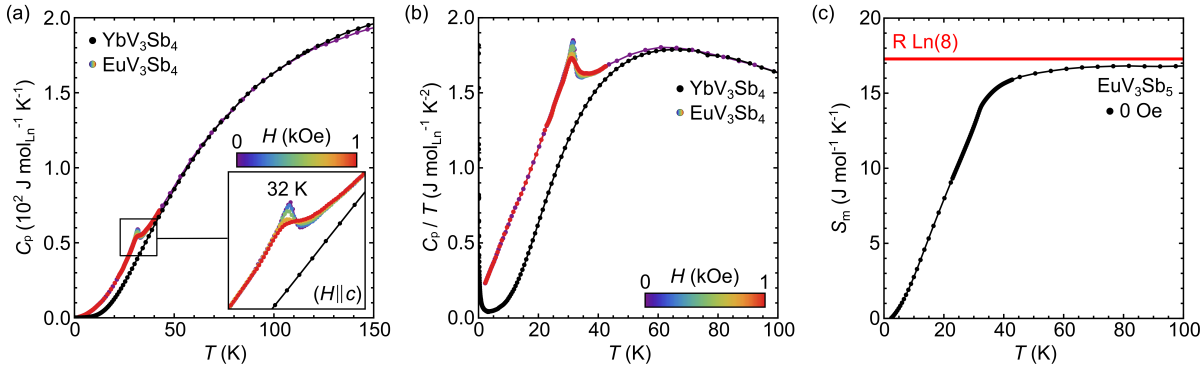

Figure 5.5: In line with the magnetization findings, heat capacity measurements on EuV_3Sb_4 single crystals exhibit a clear lambda-like anomaly at $T_C = 32$ K. The transition is field--dependent, broadening and shifting slightly to lower temperatures (a, inset). In the C_p/T plot (b), subtracting the scaled YbV_3Sb_4 nonmagnetic lattice reference isolates the magnetic contribution, which, upon integration, yields 97% of $R\ln 8$, consistent with divalent Eu^{2+}.

approximately 16.8 J mol^{-1} K^{-1}, accounting for 97% of the expected entropy from Eu^{2+} ions in the fully ordered state ($R\ln 8$).

Overall, the data indicate that EuV_3Sb_4 adopts a noncollinear or modulated (e.g., helical or cycloidal) magnetic ground state under zero field conditions. This may explain the observed cusp in the magnetization just below T_C in the hard-axis susceptibility data. However, comprehensive exploration of this possibility will necessitate larger samples and future scattering experiments (e.g., resonant x-ray or neutron scattering).

5.4 Conclusion

We introduced two novel vanadium-based kagome materials, YbV_3Sb_4 and EuV_3Sb_4, both belonging to the broader AM_3X_4 family, which primarily consists of Ti–Bi based kagome metals with rare-earth ions. While the vanadium kagome sublattice remains nonmagnetic, the inclusion of the rare-earth sublattice introduces zig-zag chains that interconnect the kagome planes, providing the potential for magnetic degrees of freedom.

YbV_3Sb_4 demonstrates properties of a nonmagnetic kagome metal, displaying no discernible bulk phase transitions down to 60 mK. The structural imperfections and their effects on the electronic structure were comprehensively studied using Density Functional Theory (DFT), which facilitated a deeper understanding of the material's behavior. On the other hand, EuV_3Sb_4 exhibits a ferromagnetic-like ground state below $T_C = 32$ K. Notably, the ordered state of EuV_3Sb_4 displays an easy-plane anisotropy, suggesting the presence of a canted or modulated order even in the absence of an external magnetic field. These findings motivate further investigations into the magnetic ground state of EuV_3Sb_4.

This study not only establishes the significance of the newly discovered LnV_3Sb_4 class of kagome metals but also underscores the potential of these materials as platforms for exploring *Ln*-site-tuned magnetic order in tandem with the inherent topologically nontrivial features characteristic of kagome band structures. The combination of experimental data and theoretical insights, particularly from the DFT calculations, provides a comprehensive understanding of the structural, electronic, and magnetic properties of these intriguing materials, paving the way for future studies aimed at uncovering their unique physical phenomena and potential applications. The findings from this research have been published[108].

5.5 Acknowledgments

B.R.O. and P.M.S. acknowledge financial support from the University of California, Santa Barbara, through the Elings Fellowship. S.D.W. and G.P. acknowledge financial support from the US Department of Energy (DOE), Office of Basic Energy Sciences, Division of Materials Sciences and Engineering under Grant No. DE-SC0017752. A portion of this research, including the undergraduate internship program for M. G., F. K., and R. S. acknowledge support by the National Science Foundation (NSF) through Enabling Quantum Leap: Convergent Accelerated Discovery Foundries for Quantum Materials Science, Engineering and Information (Q-AMASE-

i): Quantum Foundry at UC Santa Barbara (DMR-1906325). S.J.G.A. acknowledges financial support from the National Science Foundation Graduate Research Fellowship under Grant 1650114. A portion of this research, including support for E.S.T and T.B., was supported by the National Science Foundation (NSF) under grants DMR-1950924 and DMR-1555340, respectively. This work is based upon research conducted at the Center for High Energy X-ray Sciences (CHEXS) which is supported by the National Science Foundation under award DMR-1829070. Use of the Advanced Photon Source at Argonne National Laboratory was supported by the U. S. Department of Energy, Office of Science, Office of Basic Energy Sciences, under Contract No. DE-AC02-06CH11357. The research made use of the shared experimental facilities of the NSF Materials Research Science and Engineering Center at UC Santa Barbara (DMR- 1720256). The UC Santa Barbara MRSEC is a member of the Materials Research Facilities Network. (www.mrfn.org).

Chapter 6

Other 135 and 166 vanadium-based kagome metals

6.1 Introduction

In this chapter we are going to talk about other kagome metals. We initiated our exploration by investigating the AV_3Sb_5 (A = K, Rb, Cs) family, commonly denoted as "135" compounds. The broader scope of the 135 family was recently predicted, as detailed in a recent first-principles study that systematically examined 1386 kagome structures with the AM_3X_5 stoichiometry (where A represents alkali elements, M represents transition metals, and X represents anionic elements from *IIIA*, *IVA*, and *VA*), all exhibiting the $P6/mmm$ space group [45]. Subsequently, $CsTi_3Bi_5$ was synthesized and confirmed to possess a stable kagome structure by Professor Dirk Johrendt and his research team. Our initial calculations of the band structure for $CsTi_3Bi_5$ indicated a shifted Fermi level (as illustrated later in Figure 10), akin to the behavior observed in CsV_3Sb_5, although strong superconductivity was not observed. However, further detailed studies are necessary to elucidate the electronic structure characteristics of $CsTi_3Bi_5$.

Another prominent focus of our research involves the "166" compounds, a family of kagome

metals crystallizing in the $MgFe_6Ge_6$ structural prototype. These AB_6X_6 compounds feature two kagome sheets per unit cell, separated by alternating AX_2 and X_2 layers, as illustrated in Figure 6.3. The A-site can accommodate various alkali, alkaline earth, and rare earth metals, while the B-site typically hosts transition metals. The X-site is generally restricted to group IV elements. Due to this chemical diversity, the 166 materials exhibit a wide array of functionalities, particularly among those with magnetic host lattices [141, 142, 143].

Future endeavors aim to investigate additional compounds within these families and other kagome networks. For instance, ScV_6Sn_6 and TbV_6Sn_6 are other members of the RV_6Sn_6 series featuring a kagome network. Band structure calculations revealed the presence of saddle points near the Fermi level, which can be modulated through electron or hole doping. Notably, a recent study of ScV_6Sn_6 reported charge density wave (CDW) ordering in this system [143]. Given the diversity of the AB_6X_6 family, it offers numerous opportunities to explore the factors influencing charge ordering and superconductivity in kagome metals. Phonon calculations represent another intriguing approach to gain deeper insights into the electronic structure of this material. By inducing structural distortions along high symmetry points and comparing formation energies, we aim to identify the ground state structure.

6.2 Methods

For our electronic state calculations, we conducted first-principles analyses using density functional theory (DFT) within the Vienna ab-initio Simulation Package (VASP), as previously described in references [83, 84]. To facilitate these calculations, we utilized the projector augmented wave (PAW) method [38, 85] and performed ionic relaxation procedures with an energy cutoff of 520 eV. Our investigation included the automatic generation of reciprocal space k-point meshes at a density of 55 $Å^{-1}$ along each reciprocal lattice vector.

Our analysis primarily focused on computing the band structure along key paths, determined

based on high symmetry points, following the definitions provided by Setyawan and Curtarolo [86]. To obtain a comprehensive understanding of the electronic properties, we visualized the density of states (DOS) and band structures using the sumo package [87]. The phonon dispersion spectrums were calculated using the PHONOPY package[144]. The structure constructed with the help of the VESTA program[31].

6.3 $CsTi_3Bi_5$

In condensed matter physics, the kagome lattice serves as an essential quantum material system, showcasing the interplay between electron correlation, topology, and lattice geometry [145, 146]. Notably, the unique electronic structures exhibited by the kagome lattice, such as flat bands, Dirac cones, and van Hove points, stem from its distinctive lattice geometry [147]. Since, the quasi-two-dimensional kagome materials CsV_3Sb_5, RbV_3Sb_5, and KV_3Sb_5 have emerged, linking superconductivity with kagome physics, thereby amplifying the curiosity within the physics community to uncover further unconventional quantum phenomena from the kagome lattice [3, 4, 75, 77, 78, 110, 147, 148, 149].

Despite the growing interest in kagome materials, discovering the desired candidates remains a challenging task. Consequently, the advancement of quantum physics heavily relies on identifying a viable material system with low dimensionality and various symmetry-breaking instabilities, such as charge density wave and superconductivity.

In a recent, first principles study[45], a group of researchers systematically evaluated 1386 kagome structures with the stoichiometry of AM_3X_5 (A for alkali elements, M for transition metals, and X for anionic elements from IIIA, IVA, and VA) with the P6/mmm space group. Asummary of their study presented in Figure 6.1[45]. The study computed optimized structures, thermodynamic stability (energy above hull < 5 meV/atom), and electronic structures. As a result, 28 promising candidates emerged from the screening process, including CsV_3Sb_5,

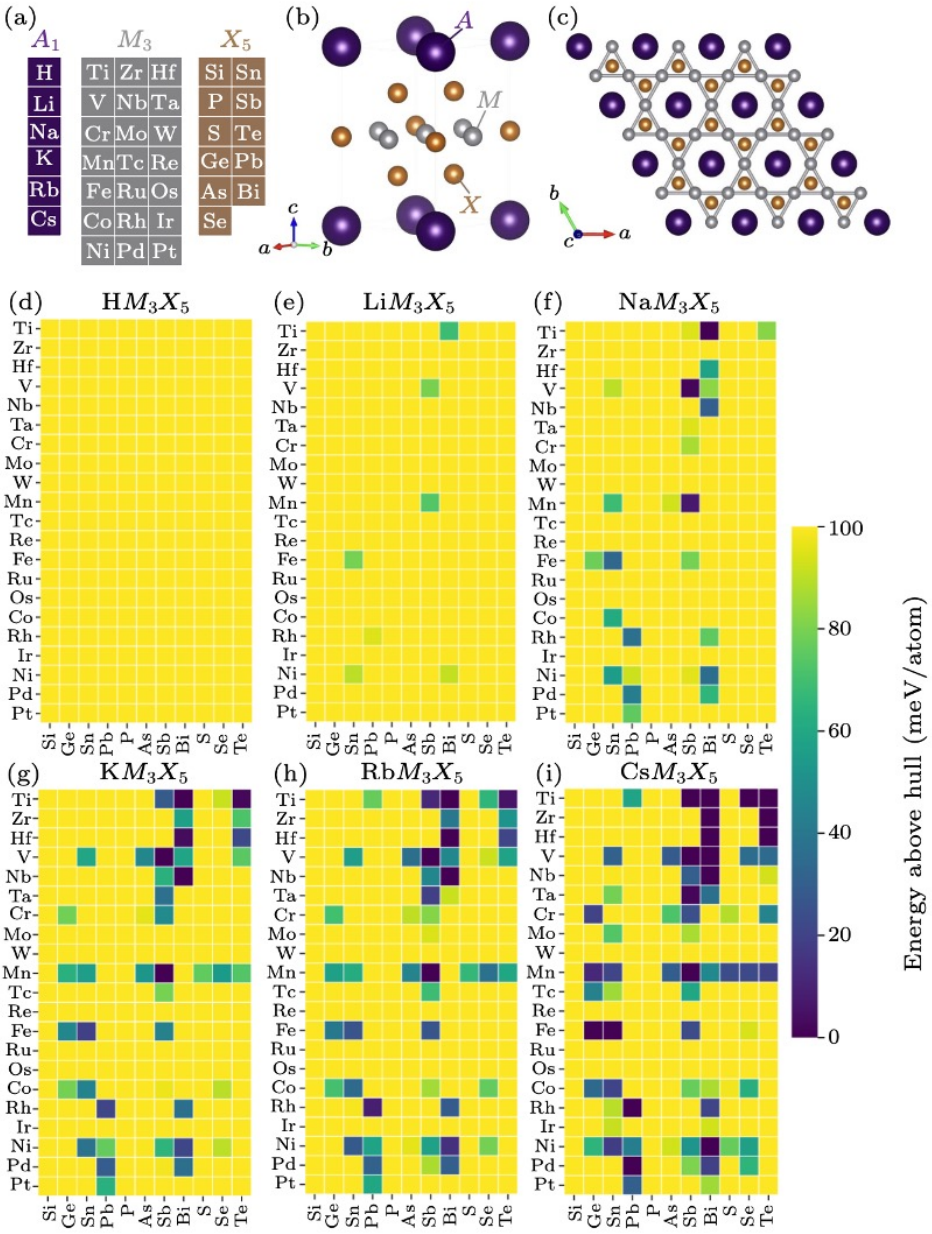

Figure 6.1: (a)–(c) The structure and the schematic of the element substitution strategy for generating CsV_3Sb_5-like compounds, and the transition metal forms the kagome lattice in the structure. (d)–(i), the thermodynamic stability (represented quantitatively as E_{hull}) for 1386 compounds in a heat map plotting mode is illustrated. Each box represents an AM_3X_5 compound, and the darkness of the color indicates the stability of the compound, with compounds having E_{hull} greater than 100 meV/atom depicted in yellow. This figure is adapted from [45].

RbV_3Sb_5, and KV_3Sb_5, which are the three known compounds experimentally synthesized according to existing literature, thus validating the reliability of the calculations.

Following the computational study, the findings prompted further experimental exploration. Professor Dirk Johrendt and his research group successfully synthesized $CsTi_3Bi_5$, a compound that demonstrated structural stability and featured a kagome lattice. The stability of the material verified the theoretical predictions and contributed to the growing understanding of kagome-like structures in new materials. Our calculation of the band structure of $CsTi_3Bi_5$ presented in Figure 6.2.

The experimental analysis of the $CsTi_3Bi_5$ compound revealed the absence of a strong superconductivity character within its electronic behavior, distinguishing it from the observed properties of the CsV_3Sb_5 kagome material. While both systems exhibited Γ pockets positioned below the Fermi level, the absence of saddle points under the Fermi level at the *M* point in the $CsTi_3Bi_5$ compound indicated differing electronic configurations compared to the CsV_3Sb_5 compound. Consequently, the potential mixtures of these compounds might offer an intriguing avenue for exploring unique physical properties, suggesting the possibility of uncovering novel quantum phenomena resulting from the interplay of different electronic structures in these mixed systems. The more detailed study has been published[134].

6.4 166 vanadium-based kagome

Another family of kagome metals which has been the focus of our research is the so-called "166" compounds. The emergence of 166-kagome metals, adopting the $MgFe_6Ge_6$ structural prototype, has provided a recent avenue to explore a plethora of intriguing phenomena arising from the interplay between topology, correlations, and magnetism [10, 113, 122, 150, 151, 152, 153, 154, 155, 156]. These compounds have garnered significant attention due to their unique structural configuration, enabling the investigation of various unconventional electronic

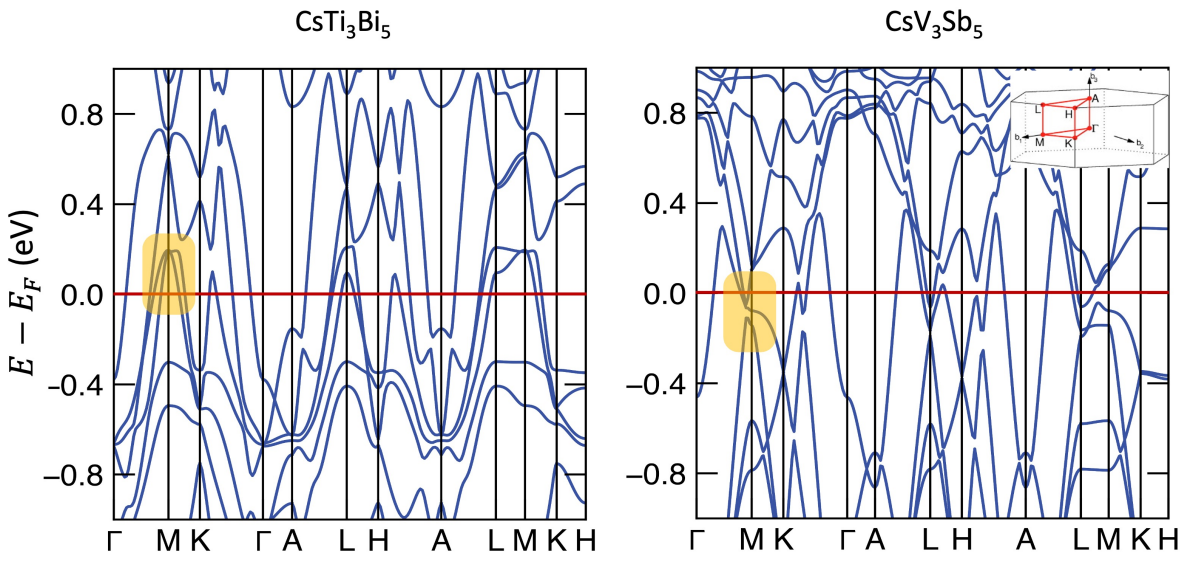

Figure 6.2: Band structures for $CsTi_3Bi_5$ and CsV_3Sb_5 with spin-orbit coupling. Although there are similarities between these two systems, the saddle point at M has been shifted above the fermi level for the $CsTi_3Bi_5$ system.

properties and magnetic behaviors.

The crystal structure of AB_6X_6 presented in Figure6.3. The A-site in the 166-kagome materials can accommodate a diverse range of alkali, alkali earth, and rare earth metals, such as Li, Mg, Yb, Sc, and Gd. On the other hand, the B-site typically accommodates a transition metal, including Co, Cr, Mn, V, and Ni. The X-site is primarily limited to group IV elements, namely Si, Ge, and Sn. Owing to this chemical diversity, 166 materials exhibit a wide array of functionalities, especially in the context of compounds with magnetic host lattices.

Recent research has uncovered a group of compounds, RV_6Sn_6 (R = rare earth), that exhibit a comparable band structure with Van Hove singularities (VHSs) in close proximity to the Fermi level (E_F). The existence of topological surface states, Dirac cones, and Van Hove singularities within the electronic band structure, coupled with the capacity to manipulate magnetic interactions through control of the R-sites in RV_6Sn_6 compounds, implies that they serve as promising platforms for exploring unconventional electronic states originating from a

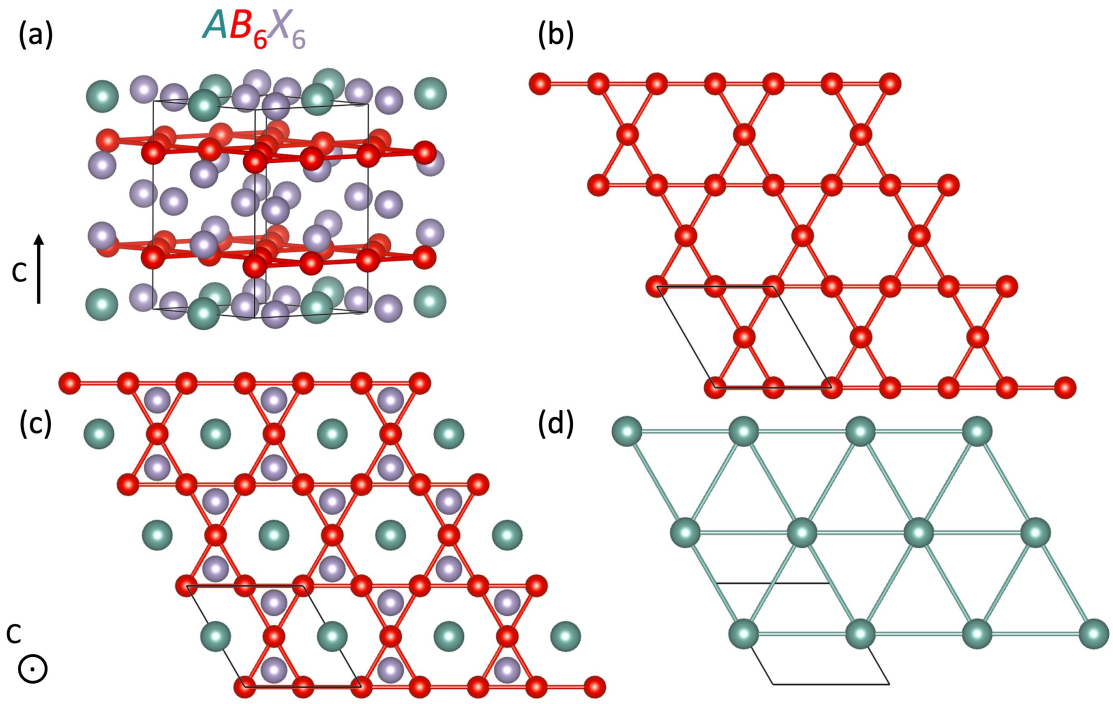

Figure 6.3: Crystal structures of AB_6X_6. (a) AB_6X_6 lattice structure comprised of different layers of AX_2 and X_2 layers. (b) Top view of crystal structure looking along the c axis and showing the kagome plane of B atoms. (c) 2D kagome net of B atoms. (d) The triangular lattice of A-site ions interwoven between kagome planes as shown looking along the c axis.

model kagome lattice proximitized with an adjustable magnetic layer. The spatial separation of the magnetic layer composed of *R*-site ions and the kagome plane not only introduces tunable magnetic properties from the magnetic layer but also facilitates a direct investigation of the electronic structure of non-magnetic kagome systems. The discovery of novel kagome metals and the potential manipulation of magnetic couplings via neighboring layers represent promising avenues for further exploration within the family of RV_6Sn_6 compounds.[142, 157]

Although the introduction of magnetic ions onto the *R*-sites of these compounds enables the engineering of various magnetic states [120, 142], the nonmagnetic versions have yet to exhibit a stabilized superconducting transition. Nevertheless, the nonmagnetic variant characterized by the smallest *R*-site cation radius, ScV6Sn6, recently exhibited indications of charge ordering.

Figure6.4 illustrates the results of the phonon calculations conducted for ScV_6Sn_6. The absence of any imaginary phonon modes suggests that the structural distortion remains minimal within these materials. Synchrotron x-ray diffraction measurements reveal high-temperature, short-range charge correlations at the wave vectors along $q = (\frac{1}{3}, \frac{1}{3}, \frac{1}{2})$ whose interlayer correlation lengths diverge upon cooling. At the charge order transition, this divergence is interrupted, and long-range order freezes in along $q = (\frac{1}{3}, \frac{1}{3}, \frac{1}{3})$, as previously reported, while disorder enables the charge correlations to persist at the $q = (\frac{1}{3}, \frac{1}{3}, \frac{1}{2})$ wave vector down to the lowest temperatures measured. Both short-range and long-range charge correlations seemingly arise from the same instability and both are rapidly quenched upon the introduction of larger Y ions onto the Sc sites. This observation suggests that the introduction of larger Y ions has a significant impact on the charge correlations, possibly altering the lattice dynamics and electronic interactions in the material[158].

Recent studies focusing on GdV_6Sn_6 and YV_6Sn_6 categorized these compounds as Z_2 kagome metals, characterized by multiple Dirac crossings and Van Hove singularities (VHS) near the Fermi level[141,142,143]. However, despite these similarities, only GdV_6Sn_6 exhibited signs of magnetic ordering below 5 K, while YV_6Sn_6 did not display any indication of local magnetism.

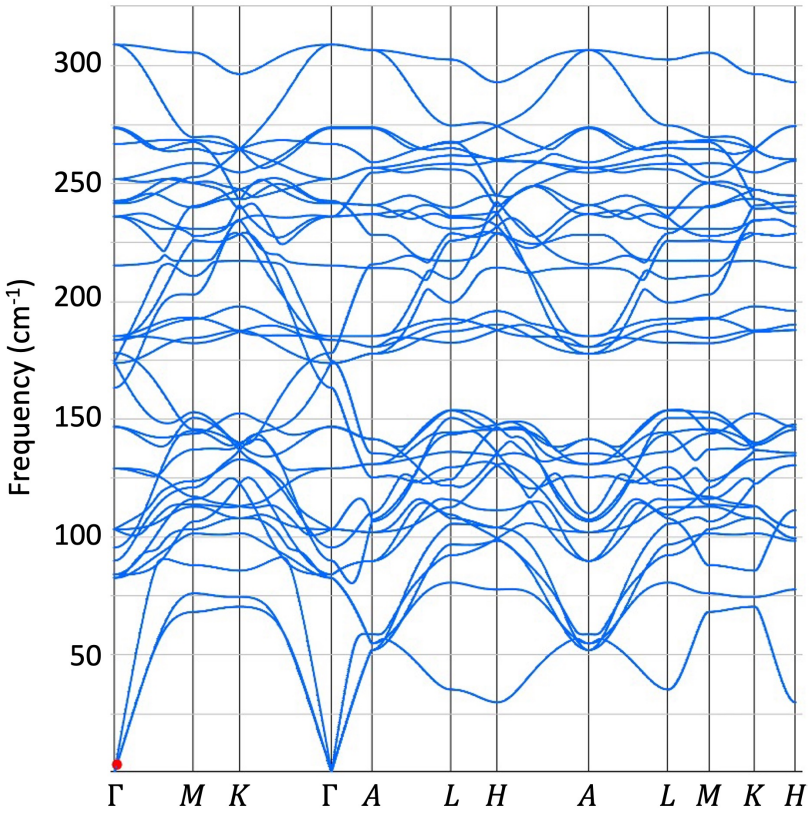

Figure 6.4: phonon spectrum calculated *via* DFT for ScV_6Sn_6. The size of the supercell is 3 $\times$ 3 $\times$ 1. No existence of imaginary phonon-modes indicates that the structural distortion is weak in these materials.

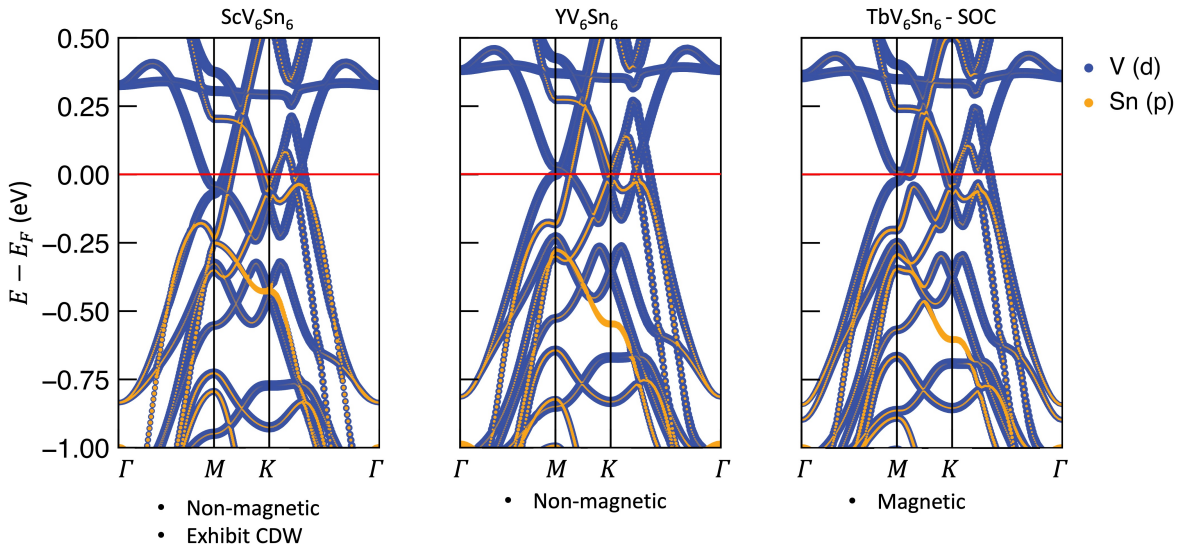

Figure 6.5: Colorized bands structure from DFT calculations show the orbitals contributions from V and Sn for ScV_6Sn_6, YV_6Sn_6 and TbV_6Sn_6 .

The presence of these instabilities near the Fermi level in the band structure, combined with the ability to manipulate magnetic interactions by controlling the *A* sites, positions this family as a promising platform for the exploration of unconventional electronic phenomena [154, 155, 156].

Figure6.5 presents the Colorized bands structure from DFT calculations, illustrating the orbitals' contributions from V and Sn for ScV_6Sn_6, YV_6Sn_6, and TbV_6Sn_6. According to previous research by Pokharel et al. [158], it has been demonstrated that ScV_6Sn_6 exhibits a charge density wave (CDW) and functions as a nonmagnetic metal. When comparing the band structure of ScV_6Sn_6 to that of the nonmagnetic YV_6Sn_6 and the magnetic TbV_6Sn_6, it is noticeable that only in ScV_6Sn_6 the *M*-saddle point is positioned below the Fermi level.

6.5 Summary and conclusion

In this chapter, we delve into the exploration of various kagome metals, beginning with the investigation of the AV_3Sb_5 (A = K, Rb, Cs) family, also known as "135" compounds. The comprehensive study conducted by Jiang et al. [45] scrutinized 1386 kagome structures characterized by the AM_3X_5 stoichiometry (where A represents alkali elements, M represents transition metals, and X represents anionic elements from groups $IIIA$, IVA, and VA) with the $P6/mmm$ space group. Subsequently, the successful synthesis of $CsTi_3Bi_5$ with a stable kagome structure by Professor Dirk Johrendt and his research team expanded our understanding of the electronic structure characteristics within the kagome lattice. Despite the absence of strong superconductivity in $CsTi_3Bi_5$, further investigations are required to elucidate its electronic behavior.

Moreover, our exploration extended to the "166" compounds, a family of kagome metals exhibiting the $MgFe_6Ge_6$ structural prototype. Notably, the diverse range of functionalities observed within the 166 materials, particularly those with magnetic host lattices, has garnered significant attention within the field [141, 142, 143]. A distinct characteristic of the 166 compounds is their ability to control the magnetic interactions through manipulation of the R-sites, leading to unconventional electronic states originating from the model kagome lattice.

The phonon calculations performed for ScV_6Sn_6 revealed a minimal structural distortion, as illustrated in Figure 6.4. Based on the previous research, synchrotron x-ray diffraction measurements highlighted the presence of high-temperature, short-range charge correlations, which eventually froze in along specific wave vectors upon cooling. The introduction of larger Y ions onto the Sc sites played a pivotal role in altering the lattice dynamics and electronic interactions within the material, thereby impacting the charge correlations.

Overall, the findings discussed in this chapter provide insights into the intricate electronic and structural characteristics of diverse kagome metals, underscoring the significance of their

versatile functionalities and their potential implications for future quantum material research. Further in-depth analyses and studies have been published on these topics [134, 158].

Chapter 7

Triangular-lattice $LaCd_3P_3$ compound

Crystalline compounds with geometric magnetic frustration continue to be a central focus in condensed matter physics, mainly due to their potential to host a diverse range of interesting ground states. When confined to low-dimensional structures, such as quasi-one-dimensional systems and two-dimensional arrangements, these compounds often exhibit amplified quantum fluctuations, leading to the emergence of unique quantum ground states, notably the quantum spin liquid state. Of particular interest are material systems featuring two-dimensional triangular lattices, which have garnered significant attention. These systems offer a high degree of geometric frustration, owing to the arrangement of magnetic moments in edge-sharing triangles within the two-dimensional array. This geometric setup not only enhances quantum fluctuations but also amplifies the likelihood of observing unconventional quantum ground states. In this chapter we are going to talk about $LaCd_3P_3$ which is part of the RM_3Pn_3, also known as 133 family.

7.1 Introduction

The layered RM_3Pn_3 compounds, where R represents a rare earth element and M is either Zn or Cd, along with Pn being P or As, consist of R^{3+} cations arranged on well-separated triangular lattice layers [159, 160]. With interlayer distances around 10 Å, these compounds exhibit primarily two-dimensional magnetic interactions, leading to enhanced quantum fluctuations. The octahedral coordination of rare earth cations by pnictide anions results in strong crystal field ligand effects, influencing the crystal field interactions of the $4f$ electrons and creating significant anisotropies that can impact frustration in the system.

Recent investigations into $CeCd_3P_3$ and $CeCd_3As_3$ have highlighted the role of crystal field anisotropies as a key mechanism underlying the emergence of magnetic order, despite the expected two-dimensional behavior, with a transition temperature (TN) below 0.42 K [161]. The RM_3Pn_3 family encompasses several rare earth variants, from La to Er, within the RZn_3P_3 subclass, while the RCd_3P_3 subclass has only been reported for R = La, Ce, and Pr [159, 162]. Previous studies on $LaCd_3P_3$ and $CeCd_3P_3$ demonstrated metallic states in single-crystalline samples, with structural transitions occurring at approximately 170 K and 126 K, respectively, whereas polycrystalline samples exhibited insulating behavior [162].

Furthermore, for the RZn_3P_3 compounds, an increase in metallicity correlated with larger R radii, suggesting a balance between unit cell volume and band dispersion near the Fermi level [163].

Exploring the RCd_3P_3 materials class, as well as delving into the extensive RM_3Pn_3 phase space, may offer a promising route to systematically control the conductivity in these two-dimensional, seemingly frustrated magnetic materials.

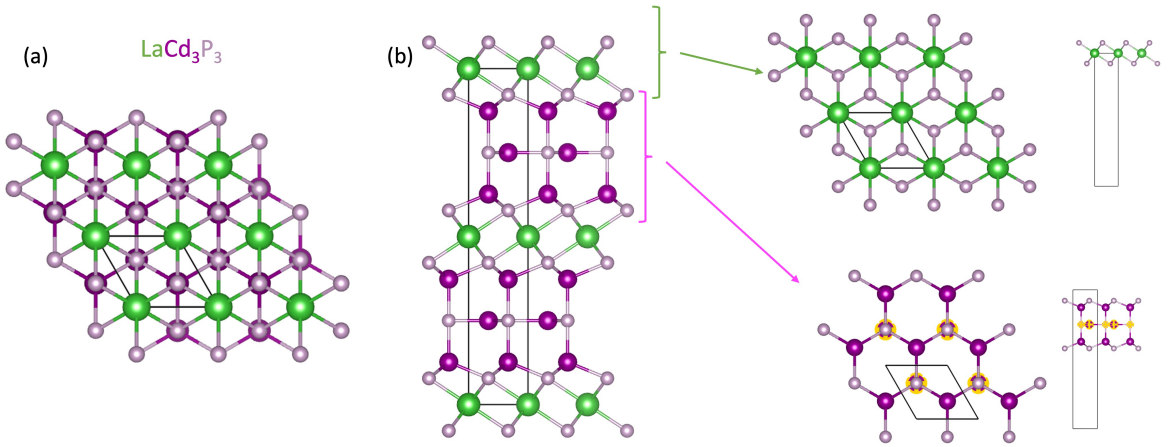

Figure 7.1: Crystal structures of $LaCd_3P_3$. (a) Top view of crystal structure looking along the c axis and showing the triangular lattice. (b) $LaCd_3P_3$ crystal structure comprised of different layers, which presented on the side.

7.2 Methods

To perform our electronic state calculations, we employed density functional theory (DFT) within the Vienna ab-initio Simulation Package (VASP) as outlined in previous works [83, 84]. The calculations were facilitated using the projector augmented wave (PAW) method [38, 85], and ionic relaxation was conducted with an energy cutoff of 520 eV. Reciprocal space k-point meshes were automatically generated at a density of 55 $Å^{-1}$ along each reciprocal lattice vector.

Our primary analysis revolved around the computation of the band structure along specific paths, based on high symmetry points defined by Setyawan and Curtarolo [86]. To gain a comprehensive understanding of the electronic properties, we visualized the density of states (DOS) and band structures using the sumo package [87]. Additionally, phonon dispersion spectrums were computed using the PHONOPY package [144], and the structure was constructed using the VESTA program [31].

7.3 Results and discussion

The structure of $LaCd_3P_3$ is presented in Figure 7.1. As we mentioned before[159, 160], $LaCd_3P_3$ is a compound belonging to the RM_3Pn_3 family, where R represents rare earth elements. This family of compounds features R^{3+} cations arranged on distinct triangular lattice layers, and $LaCd_3P_3$ specifically consists of lanthanum (La) and cadmium (Cd) elements bonded to phosphorus (P) atoms. The crystal structure of $LaCd_3P_3$ can be characterized by its unique arrangement of components and its two-dimensional geometric layout, which can contribute to its magnetic and electronic properties.

The specific heat measurements, which were previously studied [162], clearly display a discernible feature in the form of a γ-like anomaly at $T_s = 173$ K, in accordance with the electrical resistivity data. This characteristic anomaly is a strong indicator of the presence of a charge density wave (CDW) in $LaCd_3P_3$. To delve deeper into the structural stability and understand the intricate phonon behavior, we employed extensive phonon calculations. These calculations were instrumental in providing a more comprehensive understanding of the material's phonon properties. The phonon calculation is presented in Figure 7.2. The phonon spectrum was calculated through density functional theory (DFT) for $LaCd_3P_3$. The supercell's size was determined to be $2 \times 2 \times 1$. The presence of imaginary phonon-modes suggests the possibility of structural distortion in these materials.

To follow that, we tried with distorting the structure, with moving Cd atoms in the plane and out of the plane, and calculated the energy along the distortion path.

To explore the identification of a lower-energy structure, various crystallographic distortions were tested by manipulating the positions of the Cd atoms both in-plane and out-of-plane. Subsequently, the energy along the distortion path was computed. The results of these analyses are presented in Figure 7.3 and Figure 7.4, where an increase in energy and absence of a significant local minimum indicate that these distortions are not thermodynamically favorable. This

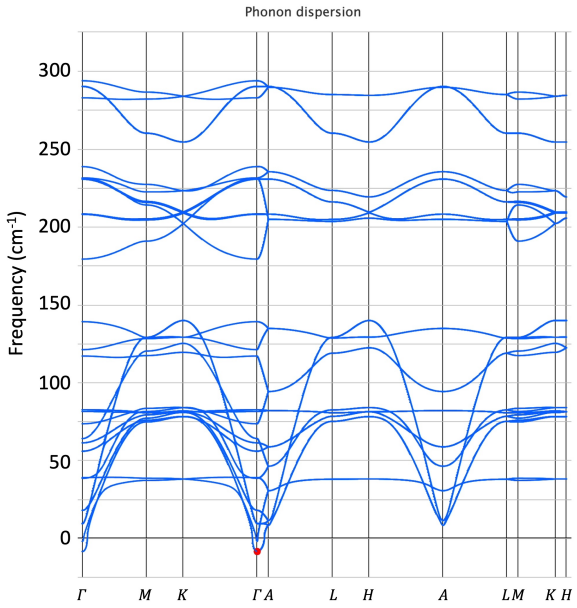

Figure 7.2: phonon spectrum calculated *via* DFT for $LaCd_3P_3$. The size of the supercell is $2 \times 2 \times 1$. The existence of imaginary phonon-modes indicates that the possibility of the structural distortion in these materials.

suggests the robustness of the original crystallographic configuration against such distortions. Further study needed to identify the lower energy structure and CDW distorted structures.

To get more information about the electronic structure of the $LaCd_3P_3$, I did a band structure with spin orbit coupling calculation which presented in Figure7.5(a). In the band structure analysis, it was observed that the valence band maximum predominantly comprises P-*p* states, suggesting a significant contribution from the phosphorus orbitals to the electronic structure. On the other hand, the conduction band minima predominantly involve La-*d* orbitals, indicating a substantial influence of the lanthanum *d* orbitals on the conduction properties. Our calculations revealed that $LaCd_3P_3$ possesses a calculated band gap of 0.75 eV. These findings are in rough agreement with the transport gaps obtained from resistivity measurements, indicating that the observed metallicity in single crystal studies may be a result of light doping[162, 164]. To gain a more comprehensive understanding, we delved deeper into the analysis by conducting intricate calculations involving the doping of Ca into the structure through the substitution of La. The

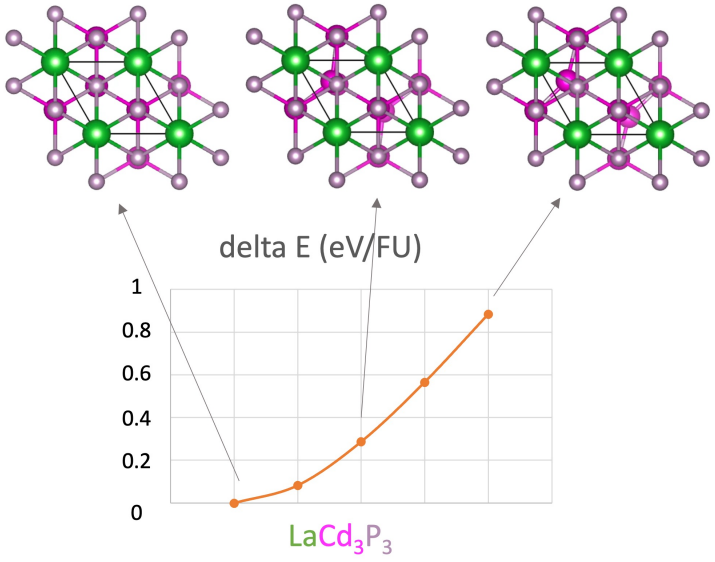

Figure 7.3: Crystallographic distortions and calculated energy along the path for $LaCd_3P_3$. The Cd atoms, moves in plane.

resulting compound, $La0.5Ca0.5Cd_3P_3$ ($LaCaCd_6P_6$) which presented in Figure 7.5 (b), was subjected to a rigorous band structure analysis, revealing a discernible increase in the metallic characteristics of the doped structure.

7.4 Summary and conclusion

The exploration of crystalline compounds with geometric magnetic frustration continues to offer significant insights into condensed matter physics, particularly due to their potential to host a diverse range of intriguing ground states. This chapter talked about $LaCd_3P_3$, which is part of the RM_3Pn_3 family. The material's geometric setup, characterized by its two-dimensional triangular lattice, has facilitated the observation of notable features like charge density wave (CDW) signatures, and a calculated band gap of 0.75 eV and metallicity with doping.

Our extensive investigations, employing techniques such as density functional theory (DFT) calculations, phonon spectrum analyses, and crystallographic distortions, have offered crucial

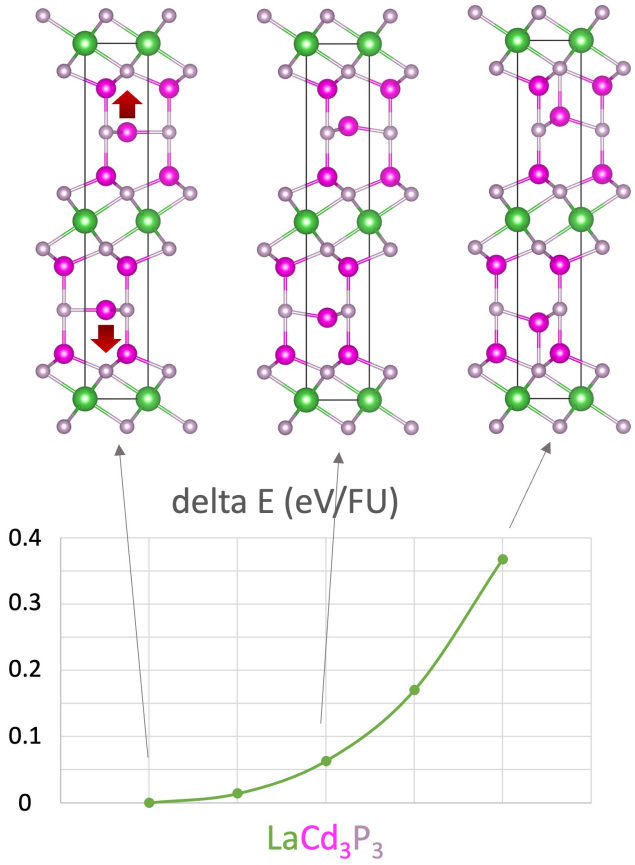

Figure 7.4: Crystallographic distortions and calculated energy along the path for $LaCd_3P_3$. The Cd atoms display out-of-plane movement.

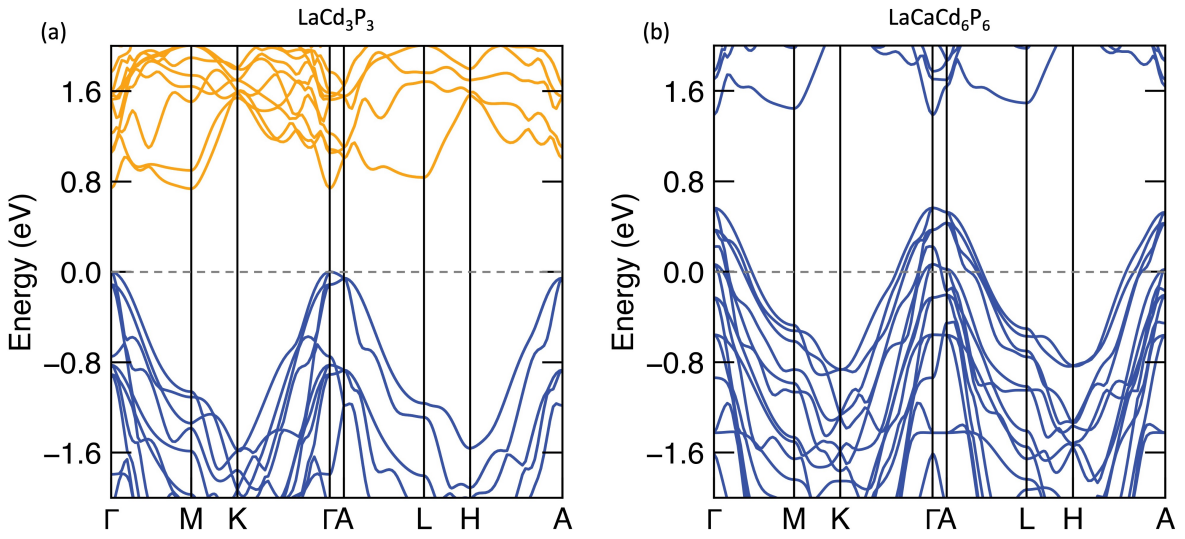

Figure 7.5: The electronic band structures with spin orbit coupling of (a) $LaCd_3P_3$ and (b)$LaCaCd_6P_6$

insights into the structural stability and electronic behavior of $LaCd_3P_3$. While the material exhibits a robust resistance to crystallographic distortions, the possibility of structural distortion has been suggested by the presence of imaginary phonon modes. Furthermore, our results have pointed towards the influence of doping on the material's electronic properties, with the introduction of Ca leading to an increased metallic nature within the doped structure.

Overall, the comprehensive exploration of $LaCd_3P_3$ has not only enhanced our understanding of its unique properties and behaviors but has also contributed to the broader context of research on geometrically frustrated magnetic materials and their intriguing quantum states. The findings from this study are currently undergoing final preparations for publication.

Chapter 8

Conclusion

In this thesis, I have explored various analyses of the electronic structure across multiple kagome materials. Overall, these results represents a contribution to the ever-expanding knowledge base in the field of kagome materials. With thoroughly comparisons between our DFT simulation results and real-world experimental data, we aimed to reveal the intricate physical mechanisms responsible for the diverse phenomena observed in these captivating materials. The careful examination of their electronic, magnetic, and structural properties has revealed previously undiscovered facets, opening up new possibilities for further research and development in this exciting field. By delving into the realm of electronic instability in kagome materials, this research report provides valuable insights into their fascinating properties.

The investigation into the Fermi surface nesting-driven instabilities in CsV_3Sb_5 a member of the AV_3Sb_5 kagome family has resulted in several significant conclusions, shedding light on the complex behavior of these materials which presented in chapter 2. This compound exhibit a CDW at $T = 94$ K, and some research suggested that the phase transition is dominated by charge density waves and a Peierls-like nesting-driven instability. Our analysis has revealed that the peaks observed at the M point in the nesting function and the real part of the susceptibility are not singularly strong; rather, they are part of ridges extending along the $\Gamma - M$ direction.

While they contribute to the electronic instability to some extent, they do not solely drive it.

Moreover, we have observed that Fermi surface nesting is largely insensitive to variations in the k_z value. The $\chi''(q)$ and $\chi'(q)$ maps exhibit qualitative similarity at different k_z values, indicating that specific features in the saddle points may not uniquely influence the nesting effects.

Additionally, the Lindhard function remains relatively unchanged with variations in the Fermi level and k_z value, suggesting that the kagome saddle point has minimal relevance to the overall nesting behavior. These findings challenge previous assumptions regarding the relationship between the saddle points and the nesting effects. Our results indicate that the CDWs observed in CsV_3Sb_5 do not solely arise from a singular instability in the electronic structure and cannot be classified as type-I Peierls-like distortions. Furthermore, our findings suggest that the electron-phonon coupling mechanism may play a crucial role in the observed CDW ordering in CsV_3Sb_5, similar to $NbSe_2$ [27, 63]. The intricate phase diagrams resulting from chemical substitutions within the AV_3Sb_5 family offer new avenues for exploring the interplay between charge density wave and superconductivity.

Based on the prior discussion, the research conducted suggests that the lack of a clear Peierls-like transition signature reinforces the idea that the breathing mode distortions in CsV_3Sb_5 are not exclusively a result of Fermi surface nesting effects. Consequently, it implies that other factors, such as electron-phonon interactions or complex electronic correlations, might contribute to driving the observed charge density wave (CDW) ordering.

To further study, we tuned the band structure by hole-doping. The introduction of hole-doping through the substitution of Sn into the CsV_3Sb_5 compound led to the emergence of two distinct superconducting (SC) regions, each with its unique characteristics. Notably, the first SC dome coexists with the CDW order, emphasizing the intricate interplay between the Sb p_z states, CDW, and superconductivity. The application of first-principle studies shed light on how the Sb p_z states intertwine with both CDW order and SC, offering insights into the chemical tuning of

the competition between these states in the new class of AV_3Sb_5 kagome superconductors. The published results of this study in chapter 3 pave the way for exploring and understanding the unique properties and exotic physical phenomena exhibited by these intriguing materials.

Moreover, the comprehensive investigation into the phase diagrams resulting from Sn-substitution or hole-doping in KV_3Sb_5 and RbV_3Sb_5 showcased intriguing solubility variations linked to the size of the *A*-site cation. The resulting phase diagrams exhibited consistent characteristics, featuring a single superconducting dome and a rapid suppression of the CDW order, diverging from the observed double dome in CsV_3Sb_5. This comprehensive research, detailed in the associated chapter 4, provides a thorough understanding of the diverse behavior exhibited by the AV_3Sb_5 compounds, paving the way for further investigations into these unique materials and their underlying properties.

In chapter 5, two novel vanadium-based kagome materials, YbV_3Sb_4 and EuV_3Sb_4 part of the AM_3X_4 family, were introduced, highlighting their distinct magnetic properties. While YbV_3Sb_4 exhibited nonmagnetic behavior, EuV_3Sb_4 demonstrated a ferromagnetic-like ground state. This study emphasizes the potential of these materials for exploring tunable magnetic order and their unique kagome band structure. The combination of experimental data and theoretical insights provides a comprehensive understanding of their properties and potential applications [108].

Chapter 6 provided a comprehensive exploration of diverse kagome metals, including the "135" and "166" compounds. The "135" family, represented by AV_3Sb_5 (A = K, Rb, Cs), was extensively studied by Jiang et al. [45], showcasing 1386 kagome structures with the $P6/mmm$ space group. Additionally, comparing the electronic structure characteristics of $CsTi_3Bi_5$ with CsV_3Sb_5 shed light on the electronic structure characteristics within the kagome lattice. Further investigations are necessary to comprehend the electronic behavior of $CsTi_3Bi_5$.

Moreover, the RV_6Sn_6 family compounds, typified by the $MgFe_6Ge_6$ structure, revealed diverse functionalities, particularly in materials with magnetic host lattices, attracting substantial

interest [141, 142, 143]. The 166 compounds demonstrated the ability to manipulate magnetic interactions through the modification of the *R*-sites, resulting in unconventional electronic states derived from the kagome lattice model. The phonon calculations conducted for ScV_6Sn_6 indicated minimal structural distortion, alongside the presence of high-temperature, short-range charge correlations. Notably, the introduction of larger *Y* ions onto the Sc sites played a pivotal role in altering the lattice dynamics and electronic interactions, thus influencing the charge correlations observed in the material.

Finally, our investigations into $LaCd_3P_3$, part of the RM_3Pn_3 family, are presented in chapter 7. The research has deepened our understanding of structural stability and electronic behavior of this material, particularly its resistance to crystallographic distortions and the influence of doping on its metallic nature.

The collective findings from these studies have significantly advanced our understanding of the electronic and magnetic properties of various kagome materials, paving the way for further research into their exotic physical phenomena and potential applications.

Bibliography

[1] M. Vergniory, L. Elcoro, C. Felser, N. Regnault, B. A. Bernevig, and Z. Wang, "A complete catalogue of high-quality topological materials," *Nature*, vol. 566, no. 7745, pp. 480–485, 2019.

[2] F. Tang, H. C. Po, A. Vishwanath, and X. Wan, "Comprehensive search for topological materials using symmetry indicators," *Nature*, vol. 566, no. 7745, pp. 486–489, 2019.

[3] B. R. Ortiz, L. C. Gomes, J. R. Morey, M. Winiarski, M. Bordelon, J. S. Mangum, I. W. H. Oswald, J. A. Rodriguez-Rivera, J. R. Neilson, S. D. Wilson, E. Ertekin, T. M. McQueen, and E. S. Toberer, "New kagome prototype materials: discovery of KV_3Sb_5, RbV_3Sb_5, and CsV_3Sb_5," *Phys. Rev. Mater.*, vol. 3, p. 094407, 2019.

[4] B. R. Ortiz, S. M. Teicher, Y. Hu, J. L. Zuo, P. M. Sarte, E. C. Schueller, A. M. Abeykoon, M. J. Krogstad, S. Rosenkranz, R. Osborn, *et al.*, "CsV_3Sb_5: A $\mathbb{Z}_2$ topological kagome metal with a superconducting ground state," *Phys. Rev. Lett.*, vol. 125, no. 24, p. 247002, 2020.

[5] B. R. Ortiz, E. Kenney, P. M. Sarte, S. M. L. Teicher, R. Seshadri, M. J. Graf, and S. D. Wilson, "Superconductivity in the $\mathbb{Z}_2$ kagome metal KV_3Sb_5," *Phys. Rev. Mater.*, vol. 5, p. 034801, 2020.

[6] H. Tan, Y. Liu, Z. Wang, and B. Yan, "Charge density waves and electronic properties of superconducting kagome metals," *Phys. Rev. Lett.*, vol. 127, no. 4, p. 046401, 2021.

[7] M. L. Kiesel and R. Thomale, "Sublattice interference in the kagome hubbard model," *Phys. Rev. B*, vol. 86, no. 12, p. 121105, 2012.

[8] S.-L. Yu and J.-X. Li, "Chiral superconducting phase and chiral spin-density-wave phase in a hubbard model on the kagome lattice," *Phys. Rev. B*, vol. 85, no. 14, p. 144402, 2012.

[9] W.-S. Wang, Z.-Z. Li, Y.-Y. Xiang, and Q.-H. Wang, "Competing electronic orders on kagome lattices at van Hove filling," *Phys. Rev. B*, vol. 87, no. 11, p. 115135, 2013.

[10] J.-X. Yin, W. Ma, T. A. Cochran, X. Xu, S. S. Zhang, H.-J. Tien, N. Shumiya, G. Cheng, K. Jiang, B. Lian, *et al.*, "Quantum-limit chern topological magnetism in $TbMn_6Sn_6$," *Nature*, vol. 583, no. 7817, pp. 533–536, 2020.

[11] J.-X. Yin, S. H. Pan, and M. Zahid Hasan, "Probing topological quantum matter with scanning tunnelling microscopy," *Nat. Rev. Phys.*, vol. 3, no. 4, pp. 249–263, 2021.

[12] D. E. Freedman, T. H. Han, A. Prodi, P. Muller, Q.-Z. Huang, Y.-S. Chen, S. M. Webb, Y. S. Lee, T. M. McQueen, and D. G. Nocera, "Site specific x-ray anomalous dispersion of the geometrically frustrated kagomé magnet, herbertsmithite, $ZnCu_3(OH)_6Cl_2$," *J. Am. Chem. Soc.*, vol. 132, no. 45, pp. 16185–16190, 2010.

[13] D. Wulferding, P. Lemmens, P. Scheib, J. Röder, P. Mendels, S. Chu, T. Han, and Y. S. Lee, "Interplay of thermal and quantum spin fluctuations in the kagome lattice compound herbertsmithite," *Phys. Rev. B*, vol. 82, no. 14, p. 144412, 2010.

[14] T.-H. Han, J. S. Helton, S. Chu, D. G. Nocera, J. A. Rodriguez-Rivera, C. Broholm, and Y. S. Lee, "Fractionalized excitations in the spin-liquid state of a kagome-lattice antiferromagnet," *Nature*, vol. 492, no. 7429, pp. 406–410, 2012.

[15] T. Han, S. Chu, and Y. S. Lee, "Refining the spin hamiltonian in the spin -1/2 kagome lattice antiferromagnet $ZnCu_3(OH)_6Cl_2$ using single crystals," *Phys. Rev. Lett.*, vol. 108, no. 15, p. 157202, 2012.

[16] A. O'Brien, F. Pollmann, and P. Fulde, "Strongly correlated fermions on a kagome lattice," *Phys. Rev. B*, vol. 81, no. 23, p. 235115, 2010.

[17] H.-M. Guo and M. Franz, "Topological insulator on the kagome lattice," *Phys. Rev. B*, vol. 80, no. 11, p. 113102, 2009.

[18] S. Yan, D. A. Huse, and S. R. White, "Spin-liquid ground state of the S = 1/2 kagome heisenberg antiferromagnet," *J. Sci.*, vol. 332, no. 6034, pp. 1173–1176, 2011.

[19] W.-H. Ko, P. A. Lee, and X.-G. Wen, "Doped kagome system as exotic superconductor," *Phys. Rev. B*, vol. 79, no. 21, p. 214502, 2009.

[20] N. Ratcliff, L. Hallett, B. R. Ortiz, S. D. Wilson, and J. W. Harter, "Coherent phonon spectroscopy and interlayer modulation of charge density wave order in the kagome metal CsV_3Sb_5," *Phys. Rev. Mater.*, vol. 5, no. 11, p. L111801, 2021.

[21] F. Kaboudvand, S. M. Teicher, S. D. Wilson, R. Seshadri, and M. D. Johannes, "Fermi surface nesting and the lindhard response function in the kagome superconductor CsV_3Sb_5," *Appl. Phys. Lett.*, vol. 120, no. 11, p. 111901, 2022.

[22] R. E. Thorne, "Charge-density-wave conductors," *Phys. Today*, vol. 49, no. 5, pp. 42–47, 1996.

[23] X. Zhu, J. Guo, J. Zhang, and E. Plummer, "Misconceptions associated with the origin of charge density waves," *Adv. Phys. X*, vol. 2, pp. 622–640, 2017.

[24] R. E. Peierls, *Quantum theory of solids*. Clarendon Press, 1996.

[25] M. Johannes and I. Mazin, "Fermi surface nesting and the origin of charge density waves in metals," *Phys. Rev. B*, vol. 77, p. 165135, 2008.

[26] X. Zhu, Y. Cao, J. Zhang, E. Plummer, and J. Guo, "Classification of charge density waves based on their nature," *Proc. Natl. Acad. Sci. U.S.A.*, vol. 112, pp. 2367–2371, 2015.

[27] M. Johannes, I. Mazin, and C. Howells, "Fermi-surface nesting and the origin of the charge-density wave in $NbSe_2$," *Phys. Rev. B*, vol. 73, p. 205102, 2006.

[28] K. Rossnagel, O. Seifarth, L. Kipp, M. Skibowski, D. Voß, P. Krüger, A. Mazur, and J. Pollmann, "Fermi surface of 2H - $NbSe_2$ and its implications on the charge-density-wave mechanism," *Phys. Rev. B*, vol. 64, no. 23, p. 235119, 2001.

[29] L. Mattheiss, "Energy bands for 2H - $NbSe_2$ and 2H - MoS_2," *Phys. Rev. Lett.*, vol. 30, no. 17, p. 784, 1973.

[30] F. Soto, H. Berger, L. Cabo, C. Carballeira, J. Mosqueira, D. Pavuna, P. Toimil, and F. Vidal, "Electric and magnetic characterization of $NbSe_2$ single crystals: Anisotropic superconducting fluctuations above Tc," *Phys. C: Supercond.*, vol. 460, pp. 789–790, 2007.

[31] K. Momma and F. Izumi, "Vesta 3 for three-dimensional visualization of crystal, volumetric and morphology data," *J. Appl. Crystallogr.*, vol. 44, no. 6, pp. 1272–1276, 2011.

[32] M. Born, "Statistical interpretation of quantum mechanics," *J. Sci.*, vol. 122, no. 3172, pp. 675–679, 1955.

[33] M. Born and W. Heisenberg, "Zur quantentheorie der molekeln," *Original Scientific Papers Wissenschaftliche Originalarbeiten*, pp. 216–246, 1985.

[34] P. Hohenberg and W. Kohn, "Inhomogeneous electron gas," *Phys. Rev.*, vol. 136, no. 3B, p. B864, 1964.

[35] W. Kohn and L. J. Sham, "Self-consistent equations including exchange and correlation effects," *Phys. Rev.*, vol. 140, no. 4A, p. A1133, 1965.

[36] R. M. Martin, *Electronic structure: basic theory and practical methods*. Cambridge university press, 2020.

[37] D. Vanderbilt, "Soft self-consistent pseudopotentials in a generalized eigenvalue formalism," *Phys. Rev. B*, vol. 41, no. 11, p. 7892, 1990.

[38] P. E. Blöchl, "Projector augmented-wave method," *Phys. Rev. B*, vol. 50, no. 24, p. 17953, 1994.

[39] J. P. Perdew and A. Zunger, "Self-interaction correction to density-functional approximations for many-electron systems," *Phys. Rev. B*, vol. 23, no. 10, p. 5048, 1981.

[40] D. M. Ceperley and B. J. Alder, "Ground state of the electron gas by a stochastic method," *Phys. Rev. Lett.*, vol. 45, no. 7, p. 566, 1980.

[41] J. P. Perdew, K. Burke, and M. Ernzerhof, "Generalized gradient approximation made simple," *Phys. Rev. Lett.*, vol. 77, p. 3865, 1996.

[42] S. M. Teicher, *Orbital design and electronic structure of topological metals*. University of California, Santa Barbara, 2022.

[43] M. Vergniory, L. Elcoro, C. Felser, N. Regnault, B. Bernevig, and Z. Wang, "The (high quality) topological materials in the world," *arXiv preprint arXiv:1807.10271*, 2018.

[44] T. Zhang, Y. Jiang, Z. Song, H. Huang, Y. He, Z. Fang, H. Weng, and C. Fang, "Catalogue of topological electronic materials," *Nature*, vol. 566, no. 7745, pp. 475–479, 2019.

[45] Y. Jiang, Z. Yu, Y. Wang, T. Lu, S. Meng, K. Jiang, and M. Liu, "Screening promising CsV_3Sb_5-like kagome materials from systematic first-principles evaluation," *Chin. Phys. Lett.*, vol. 39, no. 4, p. 047402, 2022.

[46] T. Park, M. Ye, and L. Balents, "Electronic instabilities of kagome metals: Saddle points and Landau theory," *Phys. Rev. B*, vol. 104, p. 035142, 2021.

[47] R. Nandkishore, G.-W. Chern, and A. V. Chubukov, "Itinerant half-metal spin-density-wave state on the hexagonal lattice," *Phys. Rev. Lett.*, vol. 108, p. 227204, 2012.

[48] H. Zhao, H. Li, B. R. Ortiz, S. M. L. Teicher, T. Park, M. Ye, Z. Wang, L. Balents, S. D. Wilson, and I. Zeljkovic, "Cascade of correlated electron states in a kagome superconductor CsV_3Sb_5," *Nature*, 2021.

[49] Y.-X. Jiang, J.-X. Yin, M. M. Denner, N. Shumiya, B. R. Ortiz, G. Xu, Z. Guguchia, J. He, M. S. Hossain, X. Liu, J. Ruff, L. Kautzsch, S. S. Zhang, G. Chang, I. Belopolski, Q. Zhang, T. A. Cochran, D. Multer, M. Litskevich, Z.-J. Cheng, X. P. Yang, Z. Wang, R. Thomale, T. Neupert, S. D. Wilson, and M. Z. Hasan, "Unconventional chiral charge order in kagome superconductor KV_3Sb_5," *Nat. Mater.*, vol. 20, pp. 1353–1357, 2021.

[50] B. R. Ortiz, S. M. Teicher, L. Kautzsch, P. M. Sarte, N. Ratcliff, J. Harter, J. P. Ruff, R. Seshadri, and S. D. Wilson, "Fermi surface mapping and the nature of charge-density-wave order in the kagome superconductor CsV_3Sb_5," *Phys. Rev. X.*, vol. 11, no. 4, p. 041030, 2021.

[51] H. Miao, H. X. Li, W. Meier, A. Huon, H. N. Lee, A. Said, H. Lei, B. Ortiz, S. Wilson, J. Yin, *et al.*, "Geometry of the charge density wave in the kagome metal AV_3Sb_5," *Phys. Rev. B*, vol. 104, no. 19, p. 195132, 2021.

[52] Z. Liu, N. Zhao, Q. Yin, C. Gong, Z. Tu, M. Li, W. Song, Z. Liu, D. Shen, Y. Huang, K. Liu, H. Lei, and S. Wang, "Charge-density-wave-induced bands renormalization and energy gaps in a kagome superconductor RbV_3Sb_5," *Phys. Rev. X*, vol. 11, p. 041010, 2021.

[53] Y. Hu, S. M. Teicher, B. R. Ortiz, Y. Luo, S. Peng, L. Huai, J. Ma, N. C. Plumb, S. D. Wilson, J. He, *et al.*, "Topological surface states and flat bands in the kagome superconductor CsV_3Sb_5," *Sci. Bull.*, vol. 67, no. 5, pp. 495–500, 2022.

[54] H. Luo, Q. Gao, H. Liu, Y. Gu, D. Wu, C. Yi, J. Jia, S. Wu, X. Luo, Y. Xu, *et al.*, "Electronic nature of charge density wave and electron-phonon coupling in kagome superconductor KV_3Sb_5," *Nat. Commun.*, vol. 13, no. 1, p. 273, 2022.

[55] M. Kang, S. Fang, J.-K. Kim, B. R. Ortiz, S. H. Ryu, J. Kim, J. Yoo, G. Sangiovanni, D. Di Sante, B.-G. Park, *et al.*, "Twofold van hove singularity and origin of charge order in topological kagome superconductor CsV_3Sb_5," *Nat. Phys.*, vol. 18, no. 3, pp. 301–308, 2022.

[56] Y.-P. Lin and R. M. Nandkishore, "Complex charge density waves at van hove singularity on hexagonal lattices: Haldane-model phase diagram and potential realization in the kagome metals AV_3Sb_5 (A= K, Rb, Cs)," *Phys. Rev. B*, vol. 104, no. 4, p. 045122, 2021.

[57] R. Lou, A. Fedorov, Q. Yin, A. Kuibarov, Z. Tu, C. Gong, E. F. Schwier, B. Büchner, H. Lei, and S. Borisenko, "Charge-density-wave-induced peak-dip-hump structure and flat band in the kagome superconductor CsV_3Sb_5," *arXiv preprint arXiv:2106.06497*, 2021.

[58] C. Wang, S. Liu, H. Jeon, and J.-H. Cho, "Origin of charge density wave in the layered kagome metal CsV_3Sb_5," *Phys. Rev. B*, vol. 105, no. 4, p. 045135, 2022.

[59] P. Blaha, K. Schwarz, G. Madsen, D. Kvasnicka, and J. Luitz, *WIEN2K: An Augmented Plane Wave and Local Orbitals Program for Calculating Crystal Properties*. Karlheinz Schwarz, 2001.

[60] P. E. Blöchl, "Projector augmented-wave method," *Phys. Rev. B*, vol. 50, pp. 17953–17979, 1994.

[61] G. Kresse and J. Hafner, "Norm-conserving and ultrasoft pseudopotentials for first-row and transition elements," *J. Phys. Condens. Matter*, vol. 6, p. 8245, 1994.

[62] S. Grimme, S. Ehrlich, and L. Goerigk, "Effect of the damping function in dispersion corrected density functional theory," *J. Comput. Chem.*, vol. 32, no. 7, pp. 1456–1465, 2011.

[63] F. Weber, S. Rosenkranz, J.-P. Castellan, R. Osborn, R. Hott, R. Heid, K.-P. Bohnen, T. Egami, A. Said, and D. Reznik, "Extended phonon collapse and the origin of the charge-density wave in 2H-$NbSe_2$," *Phys. Rev. Lett*, vol. 107, no. 10, p. 107403, 2011.

[64] Y. Xie, Y. Li, P. Bourges, A. Ivanov, Z. Ye, J.-X. Yin, M. Z. Hasan, A. Luo, Y. Yao, Z. Wang, *et al.*, "Electron-phonon coupling in the charge density wave state of CsV_3Sb_5," *Phys. Rev. B*, vol. 105, no. 14, p. L140501, 2022.

[65] E. Uykur, B. R. Ortiz, S. D. Wilson, M. Dressel, and A. A. Tsirlin, "Optical detection of the density-wave instability in the kagome metal KV_3Sb_5," *npj Quantum Mat.*, vol. 7, no. 1, p. 16, 2022.

[66] Y. M. Oey, B. R. Ortiz, F. Kaboudvand, J. Frassineti, E. Garcia, S. Sanna, V. Mitrović, R. Seshadri, and S. D. Wilson, "Fermi level tuning and double-dome superconductivity in the kagome metals $CsV_3Sb_{5-x}Sn_x$," *Phys. Rev. Mater.*, vol. 6, 2022.

[67] Y. Liu, Y. Wang, Y. Cai, Z. Hao, X.-M. Ma, L. Wang, C. Liu, J. Chen, L. Zhou, J. Wang, S. Wang, H. He, Y. Liu, S. Cui, J. Wang, B. Huang, C. Chen, and J.-W. Mei, "Doping evolution of superconductivity, charge order and band topology in hole-doped topological kagome superconductors $Cs(V_{1-x}Ti_x)_3Sb_5$," *arXiv preprint arXiv:2110.12651*, 2021.

[68] S. V. Isakov, S. Wessel, R. G. Melko, K. Sengupta, and Y. B. Kim, "Hard-core bosons on the kagome lattice: Valence-bond solids and their quantum melting," *Phys. Rev. Lett.*, vol. 97, p. 147202, 2006.

[69] A. O'Brien, F. Pollmann, and P. Fulde, "Strongly correlated fermions on a kagome lattice," *Phys. Rev. B*, vol. 81, no. 23, p. 235115, 2010.

[70] A. Rüegg and G. A. Fiete, "Fractionally charged topological point defects on the kagome lattice," *Phys. Rev. B*, vol. 83, no. 16, p. 165118, 2011.

[71] M. L. Kiesel, C. Platt, and R. Thomale, "Unconventional Fermi surface instabilities in the kagome Hubbard model," *Phys. Rev. Lett.*, vol. 110, p. 126405, 2013.

[72] K. Barros, J. W. Venderbos, G.-W. Chern, and C. Batista, "Exotic magnetic orderings in the kagome Kondo-lattice model," *Phys. Rev. B*, vol. 90, no. 24, p. 245119, 2014.

[73] X. Feng, K. Jiang, Z. Wang, and J. Hu, "Chiral flux phase in the kagome superconductor AV_3Sb_5," *Sci. Bull.*, vol. 66, no. 14, pp. 1384–1388, 2021.

[74] H. Zhao, H. Li, B. R. Ortiz, S. M. Teicher, T. Park, M. Ye, Z. Wang, L. Balents, S. D. Wilson, and I. Zeljkovic, "Cascade of correlated electron states in the kagome superconductor CsV_3Sb_5," *Nature*, vol. 599, no. 7884, pp. 216–221, 2021.

[75] B. R. Ortiz, P. M. Sarte, E. M. Kenney, M. J. Graf, S. M. Teicher, R. Seshadri, and S. D. Wilson, "Superconductivity in the $\mathbb{Z}_2$ kagome metal KV_3Sb_5," *Phys. Rev. Mater.*, vol. 5, no. 3, p. 034801, 2021.

[76] Z. Liang, X. Hou, F. Zhang, W. Ma, P. Wu, Z. Zhang, F. Yu, J.-J. Ying, K. Jiang, L. Shan, *et al.*, "Three-dimensional charge density wave and surface-dependent vortex-core states in a kagome superconductor CsV_3Sb_5," *Phys. Rev. X.*, vol. 11, no. 3, p. 031026, 2021.

[77] H. Chen, H. Yang, B. Hu, Z. Zhao, J. Yuan, Y. Xing, G. Qian, Z. Huang, G. Li, Y. Ye, *et al.*, "Roton pair density wave in a strong-coupling kagome superconductor," *Nature*, vol. 599, no. 7884, pp. 222–228, 2021.

[78] Q. Yin, Z. Tu, C. Gong, Y. Fu, S. Yan, and H. Lei, "Superconductivity and normal-state properties of kagome metal RbV_3Sb_5 single crystals," *Chinese Phys. Lett.*, vol. 38, no. 3, p. 037403, 2021.

[79] F. Du, S. Luo, B. R. Ortiz, Y. Chen, W. Duan, D. Zhang, X. Lu, S. D. Wilson, Y. Song, and H. Yuan, "Pressure-induced double superconducting domes and charge instability in the kagome metal KV_3Sb_5," *Phys. Rev. B*, vol. 103, no. 22, p. L220504, 2021.

[80] K. Chen, N. Wang, Q. Yin, Y. Gu, K. Jiang, Z. Tu, C. Gong, Y. Uwatoko, J. Sun, H. Lei, *et al.*, "Double superconducting dome and triple enhancement of T_C in the kagome superconductor CsV_3Sb_5 under high pressure," *Phys. Rev. Lett.*, vol. 126, no. 24, p. 247001, 2021.

[81] Y. Song, T. Ying, X. Chen, X. Han, X. Wu, A. P. Schnyder, Y. Huang, J.-g. Guo, and X. Chen, "Competition of superconductivity and charge density wave in selective oxidized CsV_3Sb_5 thin flakes," *Phys. Rev. Lett.*, vol. 127, no. 23, p. 237001, 2021.

[82] H. LaBollita and A. S. Botana, "Tuning the Van Hove singularities in AV_3Sb_5 (A = K, Rb, Cs) via pressure and doping," *Phys. Rev. B*, vol. 104, no. 20, p. 205129, 2021.

[83] G. Kresse and J. Furthmüller, "Efficient iterative schemes for ab initio total-energy calculations using a plane-wave basis set," *Phys. Rev. B*, vol. 54, p. 11169, 1996.

[84] G. Kresse and J. Furthmüller, "Efficiency of ab-initio total energy calculations for metals and semiconductors using a plane-wave basis set," *Comput. Mater. Sci.*, vol. 6, pp. 15–50, 1996.

[85] G. Kresse and D. Joubert, "From ultrasoft pseudopotentials to the projector augmented-wave method," *Phys. Rev. B*, vol. 59, no. 3, p. 1758, 1999.

[86] W. Setyawan and S. Curtarolo, "High-throughput electronic band structure calculations: Challenges and tools," *Comput. Mater. Sci.*, vol. 49, pp. 299–312, 2010.

[87] A. M. Ganose, A. J. Jackson, and D. O. Scanlon, "sumo: Command-line tools for plotting and analysis of periodic* ab initio* calculations," *J. Open Source Softw.*, vol. 3, p. 717, 2018.

[88] A. A. Coelho, "TOPAS and TOPAS-Academic: An optimization program integrating computer algebra and crystallographic objects written in C++," *J. Appl. Crystallogr.*, vol. 51, pp. 210–218, 2018.

[89] G. W. Stinton and J. S. Evans, "Parametric Rietveld refinement," *J. Appl. Crystallogr.*, vol. 40, no. 1, pp. 87–95, 2007.

[90] K. Momma and F. Izumi, "VESTA 3 for three-dimensional visualization of crystal, volumetric and morphology data," *J. Appl. Crystallogr.*, vol. 44, pp. 1272–1276, 2011.

[91] A. Abragam, *The principles of nuclear magnetism*. No. 32, Oxford University Press, 1961.

[92] J. Luo, Z. Zhao, Y. Zhou, J. Yang, A. Fang, H. Yang, H. Gao, R. Zhou, and G.-q. Zheng, "Possible Star-of-David pattern charge density wave with additional modulation in the kagome superconductor CsV_3Sb_5," *npj Quantum Mat.*, vol. 7, no. 1, pp. 1–7, 2022.

[93] Y. Hu, X. Wu, B. R. Ortiz, X. Han, N. C. Plumb, S. D. Wilson, A. P. Schnyder, M. Shi, *et al.*, "Coexistence of Trihexagonal and Star-of-David pattern in the charge density wave of the kagome superconductor AV_3Sb_5," *Phys. Rev. B*, vol. 106, no. 24, p. L241106, 2022.

[94] A. Tsirlin, P. Fertey, B. R. Ortiz, B. Klis, V. Merkl, M. Dressel, S. Wilson, and E. Uykur, "Role of Sb in the superconducting kagome metal CsV_3Sb_5 revealed by its anisotropic compression," *SciPost Phys.*, vol. 12, no. 2, p. 049, 2022.

[95] Y. M. Oey, F. Kaboudvand, B. R. Ortiz, R. Seshadri, and S. D. Wilson, "Tuning charge density wave order and superconductivity in the kagome metals $KV_3Sb_{5-x}Sb_x$ and $RbV_3Sb_{5-x}Sb_x$," *Phys. Rev. Mater.*, vol. 6, p. L074802, 2022.

[96] X. Feng, Y. Zhang, K. Jiang, and J. Hu, "Low-energy effective theory and symmetry classification of flux phases on the kagome lattice," *Phys. Rev. B*, vol. 104, no. 16, p. 165136, 2021.

[97] X. Wu, T. Schwemmer, T. Müller, A. Consiglio, G. Sangiovanni, D. Di Sante, Y. Iqbal, W. Hanke, A. P. Schnyder, M. M. Denner, *et al.*, "Nature of unconventional pairing in the kagome superconductors AV_3Sb_5 (A = K, Rb, Cs)," *Phys. Rev. Lett.*, vol. 127, no. 17, p. 177001, 2021.

[98] Y.-P. Lin and R. M. Nandkishore, "Multidome superconductivity in charge density wave kagome metals," *Phys. Rev. B*, vol. 106, no. 6, p. L060507, 2022.

[99] J. Ge, P. Wang, Y. Xing, Q. Yin, H. Lei, Z. Wang, and J. Wang, "Discovery of charge-4e and charge-6e superconductivity in kagome superconductor CsV_3Sb_5," *arXiv preprint arXiv:2201.10352*, 2022.

[100] D. F. Agterberg, M. Geracie, and H. Tsunetsugu, "Conventional and charge-six superfluids from melting hexagonal Fulde-Ferrell-Larkin-Ovchinnikov phases in two dimensions," *Phys. Rev. B*, vol. 84, p. 014513, 2011.

[101] S. Zhou and Z. Wang, "Chern Fermi-pockets and chiral topological pair density waves in kagome superconductors," *arXiv preprint arXiv:2110.06266*, 2021.

[102] E. Uykur, B. Ortiz, O. Iakutkina, M. Wenzel, S. Wilson, M. Dressel, and A. Tsirlin, "Low-energy optical properties of the nonmagnetic kagome metal CsV_3Sb_5," *Phys. Rev. B*, vol. 104, no. 4, p. 045130, 2021.

[103] C. Zhu, X. Yang, W. Xia, Q. Yin, L. Wang, C. Zhao, D. Dai, C. Tu, B. Song, Z. Tao, *et al.*, "Double-dome superconductivity under pressure in the V-based kagome metals AV_3Sb_5 (A = Rb and K)," *Phys. Rev. B*, vol. 105, no. 9, p. 094507, 2022.

[104] F. Yu, D. Ma, W. Zhuo, S. Liu, X. Wen, B. Lei, J. Ying, and X. Chen, "Unusual competition of superconductivity and charge-density-wave state in a compressed topological kagome metal," *Nat. Commun.*, vol. 12, no. 1, pp. 1–6, 2021.

[105] H. Yang, Z. Huang, Y. Zhang, Z. Zhao, J. Shi, H. Luo, L. Zhao, G. Qian, H. Tan, B. Hu, *et al.*, "Titanium doped kagome superconductor $CsV_{3-x}Ti_xSb_5$ and two distinct phases," *Sci. Bull.*, vol. 67, no. 21, pp. 2176–2185, 2022.

[106] M. Kang, S. Fang, J. Yoo, B. R. Ortiz, Y. M. Oey, J. Choi, S. H. Ryu, J. Kim, C. Jozwiak, A. Bostwick, *et al.*, "Charge order landscape and competition with superconductivity in kagome metals," *Nat. Mater.*, vol. 22, no. 2, pp. 186–193, 2023.

[107] M. H. Christensen, T. Birol, B. M. Andersen, and R. M. Fernandes, "Theory of the charge density wave in AV_3Sb_5 kagome metals," *Phys. Rev. B*, vol. 104, p. 214513, 2021.

[108] B. R. Ortiz, G. Pokharel, M. Gundayao, H. Li, F. Kaboudvand, L. Kautzsch, S. Sarker, J. P. Ruff, T. Hogan, S. J. G. Alvarado, *et al.*, "YbV_3Sb_4 and EuV_3Sb_4 vanadium-based kagome metals with Yb^{2+} and Eu^{2+} zigzag chains," *Phys. Rev. Mater.*, vol. 7, no. 6, p. 064201, 2023.

[109] B. R. Ortiz, S. M. Teicher, Y. Hu, J. L. Zuo, P. M. Sarte, E. C. Schueller, A. M. Abeykoon, M. J. Krogstad, S. Rosenkranz, R. Osborn, R. Seshadri, L. Balents, J. He, and S. D. Wilson, "CsV_3Sb_5: a $\mathbb{Z}_2$ topological kagome metal with a superconducting ground state," *Phys. Rev. Lett.*, vol. 125, no. 24, p. 247002, 2020.

[110] B. R. Ortiz, E. Kenney, P. M. Sarte, S. M. Teicher, R. Seshadri, M. J. Graf, and S. D. Wilson, "Superconductivity in the $\mathbb{Z}_2$ kagome metal KV_3Sb_5," *Phys. Rev. Mater.*, vol. 5, no. 3, p. 034801, 2020.

[111] Q. Yin, Z. Tu, C. Gong, Y. Fu, S. Yan, and H. Lei, "Superconductivity and normal-state properties of kagome metal RbV_3Sb_5 single crystals," *Chin. Phys. Lett.*, vol. 38, no. 3, p. 037403, 2021.

[112] S. Peng, Y. Han, G. Pokharel, J. Shen, Z. Li, M. Hashimoto, D. Lu, B. R. Ortiz, Y. Luo, H. Li, M. Guo, B. Wang, S. Cui, Z. Sun, Z. Qiao, S. D. Wilson, and J. He, "Realizing kagome band structure in two-dimensional kagome surface states of RV_6Sn_6 (R = Gd, Ho)," *Phys. Rev. Lett.*, vol. 127, p. 266401, 2021.

[113] Q. Wang, K. J. Neubauer, C. Duan, Q. Yin, S. Fujitsu, H. Hosono, F. Ye, R. Zhang, S. Chi, K. Krycka, H. Lei, and P. Dai, "Field-induced topological Hall effect and double-fan spin structure with a *c*-axis component in the metallic kagome antiferromagnetic compound YMn_6Sn_6," *Phys. Rev. B*, vol. 103, p. 014416, 2021.

[114] G. Pokharel, S. M. L. Teicher, B. R. Ortiz, P. M. Sarte, G. Wu, S. Peng, J. He, R. Seshadri, and S. D. Wilson, "Electronic properties of the topological kagome metals YV_6Sn_6 and GdV_6Sn_6," *Phys. Rev. B*, vol. 104, p. 235139, 2021.

[115] G. Pokharel, B. Ortiz, J. Chamorro, P. Sarte, L. Kautzsch, G. Wu, J. Ruff, and S. D. Wilson, "Highly anisotropic magnetism in the vanadium-based kagome metal TbV_6Sn_6," *Phys. Rev. Mater.*, vol. 6, p. 104202, 2022.

[116] E. Rosenberg, J. M. DeStefano, Y. Guo, J. S. Oh, M. Hashimoto, D. Lu, R. J. Birgeneau, Y. Lee, L. Ke, M. Yi, and J.-H. Chu, "Uniaxial ferromagnetism in the kagome metal TbV_6Sn_6," *Phys. Rev. B*, vol. 106, p. 115139, 2022.

[117] N. J. Ghimire, R. L. Dally, L. Poudel, D. C. Jones, D. Michel, N. T. Magar, M. Bleuel, M. A. McGuire, J. S. Jiang, J. F. Mitchell, J. W. Lynn, and I. I. Mazin, "Competing magnetic phases and fluctuation-driven scalar spin chirality in the kagome metal YMn_6Sn_6," *Sci. Adv.*, vol. 6, no. 51, p. eabe2680, 2020.

[118] H. W. S. Arachchige, W. R. Meier, M. Marshall, T. Matsuoka, R. Xue, M. A. McGuire, R. P. Hermann, H. Cao, and D. Mandrus, "Charge density wave in kagome lattice intermetallic ScV_6Sn_6," *Phys. Rev. Lett.*, vol. 129, p. 216402, 2022.

[119] X. Zhang, Z. Liu, Q. Cui, Q. Guo, N. Wang, L. Shi, H. Zhang, W. Wang, X. Dong, J. Sun, Z. Dun, and J. Cheng, "Electronic and magnetic properties of intermetallic kagome magnets RV_6Sn_6 (*R*: Tb–Tm)," *Phys. Rev. Mater.*, vol. 6, p. 105001, 2022.

[120] J. Lee and E. Mun, "Anisotropic magnetic property of single crystals RV_6Sn_6 (*R* = Y, Gd-Tm, Lu)," *Phys. Rev. Mater.*, vol. 6, p. 083401, 2022.

[121] Z. Shao-ying, Z. Peng, L. Run-wei, C. Z.-h. Sun Ji-rong, Z. Hong-wei, and S. Bao-gen, "Structure, magnetic properties and giant magnetoresistance of $YMn_6Sn_{6-x}Ga_x$ (x = 0-0.6) compounds," *Chin. Phys.*, vol. 10, no. 4, p. 345, 2001.

[122] W. Ma, X. Xu, J.-X. Yin, H. Yang, H. Zhou, Z.-J. Cheng, Y. Huang, Z. Qu, F. Wang, M. Z. Hasan, and S. Jia, "Rare earth engineering in RMn_6Sn_6 ($R = \mathrm{Gd}-\mathrm{Tm}$, Lu) topological kagome magnets," *Phys. Rev. Lett.*, vol. 126, p. 246602, 2021.

[123] W.-S. Wang, Z.-Z. Li, Y.-Y. Xiang, and Q.-H. Wang, "Competing electronic orders on kagome lattices at van hove filling," *Phys. Rev. B*, vol. 87, p. 115135, 2013.

[124] W. R. Meier, M.-H. Du, S. Okamoto, N. Mohanta, A. F. May, M. A. McGuire, C. A. Bridges, G. D. Samolyuk, and B. C. Sales, "Flat bands in the CoSn-type compounds," *Phys. Rev. B*, vol. 102, no. 7, p. 075148, 2020.

[125] S. V. Isakov, S. Wessel, R. G. Melko, K. Sengupta, and Y. B. Kim, "Hard-core bosons on the kagome lattice: Valence-bond solids and their quantum melting," *Phys. Rev. Lett.*, vol. 97, p. 147202, 2006.

[126] A. O'Brien, F. Pollmann, and P. Fulde, "Strongly correlated fermions on a kagome lattice," *Phys. Rev. B*, vol. 81, p. 235115, 2010.

[127] A. Rüegg and G. A. Fiete, "Fractionally charged topological point defects on the kagome lattice," *Phys. Rev. B*, vol. 83, p. 165118, 2011.

[128] H.-M. Guo and M. Franz, "Topological insulator on the kagome lattice," *Phys. Rev. B*, vol. 80, p. 113102, 2009.

[129] H. Zhang, C. Liu, Y. Zhang, Z. Hou, X. Fu, X. Zhang, X. Gao, and J. Liu, "Magnetic field-induced nontrivial spin chirality and large topological Hall effect in kagome magnet $ScMn_6Sn_6$," *Appl. Phys. Lett.*, vol. 121, no. 20, p. 202401, 2022.

[130] G. Dhakal, F. C. Kabeer, A. K. Pathak, F. Kabir, N. Poudel, R. Filippone, J. Casey, A. P. Sakhya, S. Regmi, C. Sims, *et al.*, "Anisotropically large anomalous and topological hall effect in a kagome magnet," *Phys. Rev. B*, vol. 104, no. 16, p. L161115, 2021.

[131] X. Teng, L. Chen, F. Ye, E. Rosenberg, Z. Liu, J.-X. Yin, Y.-X. Jiang, J. S. Oh, M. Z. Hasan, K. J. Neubauer, *et al.*, "Discovery of charge density wave in a kagome lattice antiferromagnet," *Nature*, vol. 609, no. 7927, pp. 490–495, 2022.

[132] A. Ovchinnikov and S. Bobev, "Synthesis, crystal and electronic structure of the titanium bismuthides $Sr_5Ti_{12}Bi_{19+x}$, $Ba_5Ti_{12}Bi_{19+x}$, and $Sr_{5-\delta}Eu_\delta Ti_{12}Bi_{19+x}$ (x = 0.5–1.0; δ=2.4, 4.0)," *Eur. J. Inorg. Chem.*, vol. 2018, no. 11, pp. 1266–1274, 2018.

[133] A. Ovchinnikov and S. Bobev, "Bismuth as a reactive solvent in the synthesis of multi-component transition-metal-bearing bismuthides," *Inorg. Chem.*, vol. 59, no. 6, pp. 3459–3470, 2019.

[134] D. Werhahn, B. R. Ortiz, A. K. Hay, S. D. Wilson, R. Seshadri, and D. Johrendt, "The kagomé metals $RbTi_3Bi_5$ and $CsTi_3Bi_5$," *Z. Naturforsch. B*, vol. 77, no. 11-12, pp. 757–764, 2022.

[135] H. Bie, S. D. Moore, D. G. Piercey, A. V. Tkachuk, O. Y. Zelinska, and A. Mar, "Ternary rare-earth titanium antimonides: phase equilibria in the RE–Ti–Sb (RE = La, Er) systems and crystal structures of $RE_2Ti_7Sb_{12}$ (RE = La, Ce, Pr, Nd) and $RETi_3(Sn_xSb_{1-x})_4$ (RE = Nd, Sm)," *J. Solid State Chem.*, vol. 180, no. 8, pp. 2216–2224, 2007.

[136] G. Oszlányi and A. Sütő, "Ab initio structure solution by charge flipping," *Acta Crystallogr. A*, vol. 60, no. 2, pp. 134–141, 2004.

[137] G. Oszlányi and A. Sütő, "Ab initio structure solution by charge flipping. ii. use of weak reflections," *Acta Crystallogr. A*, vol. 61, no. 1, pp. 147–152, 2005.

[138] A. Coelho, "A charge-flipping algorithm incorporating the tangent formula for solving difficult structures," *Acta Crystallogr. A*, vol. 63, no. 5, pp. 400–406, 2007.

[139] G. M. Sheldrick, "A short history of SHELX," *Acta Crystallogr. A*, vol. 64, no. 1, pp. 112–122, 2008.

[140] G. Motoyama, M. Sezaki, J. Gouchi, K. Miyoshi, S. Nishigori, T. Mutou, K. Fujiwara, and Y. Uwatoko, "Magnetic properties of new antiferromagnetic heavy-fermion compounds, Ce_3TiBi_5 and $CeTi_3Bi_4$," *Physica B Condens.*, vol. 536, pp. 142–144, 2018.

[141] M. Li, Q. Wang, G. Wang, Z. Yuan, W. Song, R. Lou, Z. Liu, Y. Huang, Z. Liu, H. Lei, *et al.*, "Dirac cone, flat band and saddle point in kagome magnet YMn_6Sn_6," *Nat. Commun.*, vol. 12, no. 1, p. 3129, 2021.

[142] G. Pokharel, S. M. Teicher, B. R. Ortiz, P. M. Sarte, G. Wu, S. Peng, J. He, R. Seshadri, and S. D. Wilson, "Electronic properties of the topological kagome metals YV_6Sn_6 and GdV_6Sn_6," *Phys. Rev. B*, vol. 104, no. 23, p. 235139, 2021.

[143] H. W. S. Arachchige, W. R. Meier, M. Marshall, T. Matsuoka, R. Xue, M. A. McGuire, R. P. Hermann, H. Cao, and D. Mandrus, "Charge density wave in kagome lattice intermetallic ScV_6Sn_6," *Phys. Rev. Lett.*, vol. 129, no. 21, p. 216402, 2022.

[144] A. Togo, L. Chaput, T. Tadano, and I. Tanaka, "Implementation strategies in phonopy and phono3py," *J. Phys. Condens. Matter*, vol. 35, no. 35, p. 353001, 2023.

[145] Y. Zhou, K. Kanoda, and T.-K. Ng, "Quantum spin liquid states," *Rev. Mod. Phys.*, vol. 89, no. 2, p. 025003, 2017.

[146] L. Balents, "Spin liquids in frustrated magnets," *Nature*, vol. 464, no. 7286, pp. 199–208, 2010.

[147] K. Jiang, T. Wu, J.-X. Yin, Z. Wang, M. Z. Hasan, S. D. Wilson, X. Chen, and J. Hu, "Kagome superconductors AV_3Sb_5 (A = K, Rb, Cs)," *Natl. Sci. Rev.*, vol. 10, no. 2, p. nwac199, 2023.

[148] C. Mielke, D. Das, J.-X. Yin, H. Liu, R. Gupta, Y.-X. Jiang, M. Medarde, X. Wu, H. Lei, J. Chang, *et al.*, "Time-reversal symmetry-breaking charge order in a kagome superconductor," *Nature*, vol. 602, no. 7896, pp. 245–250, 2022.

[149] L. Nie, K. Sun, W. Ma, D. Song, L. Zheng, Z. Liang, P. Wu, F. Yu, J. Li, M. Shan, *et al.*, "Charge-density-wave-driven electronic nematicity in a kagome superconductor," *Nature*, vol. 604, no. 7904, pp. 59–64, 2022.

[150] N. J. Ghimire, R. L. Dally, L. Poudel, D. C. Jones, D. Michel, N. T. Magar, M. Bleuel, M. A. McGuire, J. S. Jiang, J. F. Mitchell, J. W. Lynn, and I. I. Mazin, "Competing magnetic phases and fluctuation-driven scalar spin chirality in the kagome metal YMn_6Sn_6," *Sci. Adv.*, vol. 6, no. 51, p. eabe2680, 2020.

[151] C. Sims, "Existence of chern gaps in kagome magnets RMn$_6$Ge$_6$ (R= Nd, Sm, Tb, Dy, Ho, Er, Yb, Lu)," *arXiv preprint arXiv:2203.09447*, 2022.

[152] C. Sims, "Evolution of the chern gap in kagome magnet HoMn$_6$Sn$_{6-x}$Ge$_x$," *Condens. Matter*, vol. 7, no. 2, p. 40, 2022.

[153] M. Li, Q. Wang, G. Wang, Z. Yuan, W. Song, R. Lou, Z. Liu, Y. Huang, Z. Liu, H. Lei, Z. Yin, and S. Wang, "Spin-polarized dirac cone, flat band and saddle point in kagome magnet YMn$_6$Sn$_6$," *Nat. Commun.*, vol. 12, p. 3129, 2021.

[154] X. Xu, J.-X. Yin, W. Ma, H.-J. Tien, X.-B. Qiang, P. V. S. Reddy, H. Zhou, J. Shen, H.-Z. Lu, T.-R. Chang, Z. Qu, and S. Jia, "Topological charge-entropy scaling in kagome chern magnet TbMn$_6$Sn$_6$," *Nat. Commun.*, vol. 13, no. 1, p. 1197, 2022.

[155] G. Pokharel, S. M. L. Teicher, B. R. Ortiz, P. M. Sarte, G. Wu, S. Peng, J. He, R. Seshadri, and S. D. Wilson, "Electronic properties of the topological kagome metals YV$_6$Sn$_6$ and GdV$_6$Sn$_6$ (R = Gd, Ho)," *Phys. Rev. B*, vol. 104, p. 235139, 2021.

[156] S. Peng, Y. Han, G. Pokharel, J. Shen, Z. Li, M. Hashimoto, D. Lu, B. R. Ortiz, Y. Luo, H. Li, M. Guo, B. Wang, S. Cui, Z. Sun, Z. Qiao, S. D. Wilson, and J. He, "Realizing kagome band structure in two-dimensional kagome surface states of RV$_6$Sn$_6$ (R = Gd, Ho))," *Phys. Rev. Lett.*, vol. 127, p. 266401, 2021.

[157] S. Peng, Y. Han, G. Pokharel, J. Shen, Z. Li, M. Hashimoto, D. Lu, B. R. Ortiz, Y. Luo, H. Li, *et al.*, "Realizing kagome band structure in two-dimensional kagome surface states of RV$_6$Sn$_6$ (R= Gd, Ho)," *Phys. Rev. Lett.*, vol. 127, no. 26, p. 266401, 2021.

[158] G. Pokharel, B. R. Ortiz, L. Kautzsch, S. A. Gomez, K. Mallayya, G. Wu, E.-A. Kim, J. P. Ruff, S. Sarker, and S. D. Wilson, "Frustrated charge order and cooperative distortions in ScV$_6$Sn$_6$," *Phys. Rev. Mater.*, vol. 7, no. 10, p. 104201, 2023.

[159] A. T. Nientiedt and W. Jeitschko, "The series of rare earth zinc phosphides RZn$_3$P$_3$ (R = Y, La–Nd, Sm, Gd–Er) and the corresponding cadmium compound PrCd$_3$P$_3$," *J. Solid State Chem.*, vol. 146, no. 2, pp. 478–483, 1999.

[160] S. S. Stoyko and A. Mar, "Ternary rare-earth arsenides REZn$_3$As$_3$ (RE= La–Nd, Sm) and RECd$_3$As$_3$ (RE= La–Pr)," *Inorg. Chem.*, vol. 50, no. 21, pp. 11152–11161, 2011.

[161] O. P. Uzoh, S. Kim, and E. Mun, "Influence of crystalline electric field on the magnetic properties of CeCd$_3X_3$ (X= P, As)," *Phys. Rev. Mater.*, vol. 7, no. 1, p. 013402, 2023.

[162] J. Lee, A. Rabus, N. Lee-Hone, D. Broun, and E. Mun, "The two-dimensional metallic triangular lattice antiferromagnet CeCd$_3$P$_3$," *Phys. Rev. B*, vol. 99, no. 24, p. 245159, 2019.

[163] N. Kabeya, T. Sakamoto, K. Hara, Y. Hara, S. Nakamura, K. Katoh, and A. Ochiai, "Competing exchange interactions in lanthanide triangular lattice compounds LnZn$_3$P$_3$ (Ln = La–Nd, Sm, Gd)," *journal of the physical society of japan*, vol. 89, no. 7, p. 074707, 2020.

[164] S. Higuchi, Y. Noshima, N. Shirakawa, M. Tsubota, and J. Kitagawa, "Optical, transport and magnetic properties of new compound CeCd$_3$P$_3$," *Mater. Res.*, vol. 3, no. 5, p. 056101, 2016.